

1 **Mass transfer into the leading edge of the mantle wedge:**
2 **Initial results from Oman Drilling Project Hole BT1B**
3

4 Peter B. Kelemen¹, Juan Carlos de Obeso², James A. Leong¹, Marguerite Godard³, Keishi Okazaki⁴,
5 Alissa J. Kotowski⁵, Craig E. Manning⁶, Eric T. Ellison⁷, Manuel D. Menzel⁸, Janos L. Urai⁸, Greg
6 Hirth⁹, Matthew Rioux¹⁰, Daniel F. Stockli¹¹, Romain Lafay³, Andreas M. Beinlich¹², Jude A. Coggon¹³,
7 Nehal H. Warsi¹⁴, Jürg M. Matter¹³, Damon A.H. Teagle¹³, Michelle Harris¹⁵, Katsu Michibayashi¹⁶,
8 Eiichi Takazawa¹⁷, Zaher Al Sulaimani¹⁸ and the Oman Drilling Project Science Team
9

10 1: Lamont Doherty Earth Observatory, Columbia University, Palisades NY 10964, peterk@LDEO.columbia.edu 2: Dept. of
11 Geosciences, University of Calgary 3: Géosciences Montpellier, Université de Montpellier, CNRS 4: Kochi Institute for Core
12 Sample Research, JAMSTEC 5: Dept. of Earth & Planetary Sciences, McGill University 6: Dept of Earth, Planetary & Space
13 Sciences, University of California, Los Angeles 7: Dept. of Geological Sciences, University of Colorado, Boulder 8: Tectonics
14 & Geodynamics, RWTH Aachen University 9: Dept. of Earth, Environmental and Planetary Sciences, Brown University 10:
15 Dept. of Earth Science, University of California, Santa Barbara 11: Dept. of Geological Sciences, University of Texas, Austin
16 12: Dept. of Earth Science, University of Bergen ... 13: Dept. of Ocean & Earth Science, National Oceanography Centre
17 Southampton 14: Alara Resources Ltd., Oman 15: School of Geography, Earth and Environmental Sciences, University of
18 Plymouth ...16: Dept. of Earth & Planetary Sciences, Nagoya University 17: Dept. of Geology, Niigata University & VERC IMG
19 JAMSTEC 18: Oman Water Society & Middle East Desalination Research Center
20

21 **Abstract**

22 This paper provides an overview of research on core from Oman Drilling Project Hole BT1B and the
23 surrounding area, plus new data and calculations, constraining processes in the Tethyan subduction
24 zone beneath the Samail ophiolite. The area is underlain by gently dipping, broadly folded layers of
25 allochthonous Hawasina pelagic sediments, the metamorphic sole of the Samail ophiolite, and
26 Banded Unit peridotites at the base of the Samail mantle section. Despite reactivation of some faults
27 during uplift of the Jebel Akdar and Saih Hatat domes, the area preserves the tectonic “stratigraphy”
28 of the Cretaceous subduction zone. Gently dipping listvenite bands, parallel to peridotite banding and
29 to contacts between the peridotite and the metamorphic sole, replace peridotite at and near the basal
30 thrust. Listvenites formed at less than 200°C and (poorly constrained) depths of 25 to 40 km by
31 reaction with CO₂-rich, aqueous fluids migrating from greater depths, derived from devolatilization of
32 subducting sediments analogous to clastic sediments in the Hawasina Formation, at 400-500°. Such
33 processes could form important reservoirs for subducted CO₂. Listvenite formation was accompanied
34 by ductile deformation of serpentinites and listvenites – perhaps facilitated by fluid-rock reaction – in a
35 process that could lead to aseismic subduction in some regions. Addition of H₂O and CO₂ to the
36 mantle wedge, forming serpentinites and listvenites, caused large increases in the solid mass and
37 volume of the rocks. This may have been accommodated by fractures formed as a result of volume
38 changes, perhaps mainly at a serpentinization front.
39

40 **Plain language summary**

41 This paper reports initial results from study of core from Oman Drilling Project Hole BT1B and the
42 surrounding area. It provides insights into subduction zone processes, including large fluxes of
43 recycled CO₂ from subducting sediments into the leading edge of the mantle wedge, and surprisingly
44 low temperature ductile deformation at less than 200°C. Recycling of CO₂ via carbon mineralization in
45 the hanging wall of subduction zones may produce an important, lithospheric reservoir in the global
46 carbon cycle. Ductile deformation of serpentinite, and during or after transformation of peridotite to
47 listvenites (mixtures of carbonates and opal or quartz) could explain aseismic subduction atop some
48 subduction zones.

1. Introduction

Oman Drilling Project (OmanDP) Hole BT1B at 23.364374°N, 58.182693°E, southeast of the town of Fanjah in the Sultanate of Oman, sampled serpentinized peridotites and listvenites (fully carbonated peridotites, Halls & Zhao 1995) at the base of the Samail ophiolite, the basal fault of the ophiolite, and the underlying metamorphic sole, with the intention of investigating mass transfer and deformation in the “leading edge of the mantle wedge” overlying a Tethyan subduction zone. Hole BT1B was drilled using cylindrical diamond bits and wireline core retrieval, from March 7 to March 23, 2017. Core recovery was ~ 100% throughout the Hole. Core was shipped to Japan and loaded onto Drilling Vessel Chikyu, where the OmanDP Science Team performed analyses closely following protocols established by the various incarnations of the Ocean Drilling Program (currently, the International Ocean Discovery Program, IODP). Detailed core descriptions, together with drilling history and some background information (Kelemen et al 2020b, Kelemen et al 2020c) are available online at http://publications.iodp.org/other/Oman/VOLUME/CHAPTERS/113_BT1.PDF

This paper provides a summary of initial observations, as well as original, interpretive context, for more detailed studies of core from Hole BT1B and the geology of the surrounding region, in this Special Issue of the Journal of Geophysical Research (Beinlich et al 2020, de Obeso et al 2021a, de Obeso et al 2021b, Godard et al 2017, Kotowski et al 2021, Malvoisin et al 2020, Manning et al. 2021, Menzel et al 2021, Menzel et al 2020, Okazaki et al 2021, Rioux et al 2021b) and previously published elsewhere (Falk & Kelemen 2015, Nasir et al 2007, Scharf et al 2020, Stanger 1985, Wilde et al 2002). Section 1 of this paper provides geological context for observations of core and surrounding outcrops, incorporating new data from field observations, and discussing their interpretation. Section 2 provides references for methods that have been extensively described elsewhere, and a brief summary of analytical and computational methods used to produce results presented for the first time in this paper. Section 3 summarizes observations, analytical data and computational results described in more detail in Kelemen et al. (2020b), and also reports some new data for the first time. Section 4 provides interpretation of results obtained so far, in terms of the pressure, temperature and timing of listvenite formation, the nature and source of the fluids that transformed mantle peridotite into serpentinite and listvenite, the chemical and mechanical processes during these transformations, and the deformation of altered mantle peridotite immediately above a paleo-subduction zone beneath the “leading edge of the mantle wedge”.

Some of the interpretations in this paper are qualitative and/or uncertain, even controversial. As for any samples of Cretaceous rocks, the features observed in core from Hole BT1B have been modified by later events, so that it can be difficult to discern which aspects reflect subduction zone processes, and which are younger. It is hoped that this paper, and the other papers on this region that are currently published or in press, will not pre-empt continued research, and instead will provide a starting point for future investigations of this unique and important site. In this context, readers should be aware that the archive half of the core is currently stored at Petroleum Development Oman where

89 it is available for viewing, the working half of the core is stored at the American Museum of Natural
90 History, where it can be sampled upon request to the Museum, and a huge volume of data from
91 shipboard visual core observations and analytical data is available to anyone at
92 <http://publications.iodp.org/other/Oman/OmanDP.html> , [https://www.icdp-](https://www.icdp-online.org/projects/world/asia/oman/)
93 [online.org/projects/world/asia/oman/](https://www.icdp-online.org/projects/world/asia/oman/), and other sites that can be accessed from there.

94

95

1.1 Regional geologic context

96

97 The Samail ophiolite is composed of oceanic crust formed at a submarine spreading center above a
98 subduction zone. The crustal thickness and composition of the ophiolite is similar to the geophysically
99 and geologically constrained characteristics of fast-spreading, Pacific oceanic crust, with a few km of
100 submarine lavas and sheeted dikes overlying a thicker, gabbroic lower crust (e.g., Christensen &
101 Smewing 1981, Coleman & Hopson 1981, Nicolas et al 1996) However, the lavas have a trace
102 element “subduction signature” (Alabaster et al 1982, Pearce et al 1981, Pearce & Peate 1995), and
103 parental, mantle-derived magmas appear to have contained 0.2 to 2 wt% H₂O, substantially more
104 than in primitive mid-ocean ridge basalts (MacLeod et al 2013). Beneath the crustal section of the
105 ophiolite, residual mantle peridotites and tabular dunites record polybaric decompression melting,
106 melt extraction, and focused transport of basaltic melt upward to form the crust (Braun & Kelemen
107 2002, Godard et al 2000, Kelemen et al 2000, Kelemen et al 1995, Monnier et al 2006).

108

109

1.2 Lithologies just above and below the base of the Samail ophiolite

110

111 Beneath the mantle section of the ophiolite are discontinuously exposed lenses of a “metamorphic
112 sole”, recording peak temperatures up to 700 to 900°C in samples close to the tectonic contact with
113 mantle peridotite, declining sharply downward over tens to hundreds of meters to 400 to 500°C. Peak
114 pressures and temperatures in the “metamorphic sole”, emplaced along the basal contact between
115 overlying peridotite and underlying sediments, generally record hot subduction conditions with peak
116 temperatures up to 700-900°C (Cowan et al 2014, Ghent & Stout 1981, Hacker & Gnos 1997, Searle
117 & Cox 1999, Searle & Cox 2002, Searle et al 1980, Searle & Malpas 1980, Searle & Malpas 1982,
118 Soret et al 2017) though at BT1B peak temperatures are lower (450-550°C, Kotowski et al 2021).
119 Apparently – based on published data and calculations – the sole records a broad range of peak
120 pressures from a possible lower limit of 200 MPa (Ghent & Stout 1981) or 800 MPa (Soret et al 2017)
121 to a possible upper limit of 1400 MPa (Cowan et al 2014, Searle & Cox 2002). Kotowski et al. (2021)
122 report that the sole in core from Hole BT1B records a peak pressure in the range of 800 to 1200 MPa.

123

124

125 The sole contains metasediments and meta-volcanic rocks – including submarine pillow lavas – with
126 the major element compositions of mid-ocean ridge basalts (MORB) and of alkali basalts (Searle et al
127 1980). In the core from BT1B, alkaline metabasalt compositions in the metamorphic sole (Godard et
128 al 2017, Kelemen et al 2020c) are unlike the magmas that formed the crust of the Samail ophiolite. In
the ophiolite, the structurally lowest, “Geotimes” or “V1” lavas are very similar to normal mid-ocean

129 ridge basalts, though they probably were hydrous and they contain a hint of an arc trace element
130 signature. Their composition, and that of dunite conduits for transport of primitive melts parental to V1
131 through the shallow mantle, is consistent with formation of the gabbroic lower crust in the Samail and
132 Wadi Tayin massifs of the ophiolite from primitive V1 magmas (Braun & Kelemen 2002, Kelemen et al
133 1997, Kelemen et al 1995). The overlying “Lasail” or “V2” lavas in the ophiolite are incompatible
134 element depleted, with a stronger trace element subduction signature (Alabaster et al 1982, Ernewein
135 et al 1988, MacLeod et al 2013, Pearce et al 1981) and include boninites as well as tholeiitic basalts
136 (e.g., Ishikawa et al 2002). Neither V1 nor V2 lavas are similar to the alkali basalt compositions in
137 metabasalts in the sole. Sr isotope ratios of lavas in the ophiolite and metabasalts in the sole have
138 probably been modified during alteration, so it is difficult to be sure, but the present day $^{87}\text{Sr}/^{86}\text{Sr}$
139 ratios in the submarine, alkali basalts in the sole at BT1B range from 0.704 to 0.706 (de Obeso et al
140 2021a), more radiogenic than MORB. One possibility is that they are remnants of subducted
141 seamounts, similar to accreted seamounts along the Cascadia margin of North America (e.g., Duncan
142 1982).

143

144 In addition to metabasalts, regionally the sole contains metasediments, and “exotic limestones”, all
145 incorporated by Searle and Malpas (1980) in the “Haybi Formation”. However, in this paper we
146 informally group the Haybi Formation as part of an undifferentiated metamorphic sole unit. In the
147 metamorphic sole sampled by drill core from Hole BT1B, some metasediments are clearly
148 distinguishable from the metabasalts based on texture, but some of them are compositionally similar
149 to the metabasalts, perhaps reflecting a volcanoclastic origin, whereas others grade into somewhat
150 odd, low-SiO₂, muscovite-bearing lithologies (Godard et al 2017; Kelemen et al 2020b, Kotowski et al
151 2021).

152

153 Where the sole is present, and elsewhere along the fault at the base of the mantle section of the
154 ophiolite, the lower few km of the mantle section contains easily visible, meter to 10-meter scale,
155 parallel bands of dunite, harzburgite and (rare) lherzolite, informally known as the Banded Unit. The
156 lithological contacts in this unit are sharp. They have low angle dips with respect to the paleo-seafloor,
157 the crust-mantle transition zone, and – where it is exposed – the basal fault that juxtaposes mantle
158 peridotite with the metamorphic sole. Mylonitic shear zones are present in the Banded Unit, with
159 textures recording deformation at 700–1,000°C (Boudier et al 1988, Herwegh et al 2016, Linckens et
160 al 2011, Prigent et al 2018a). Thus, there is evidence for high strain ductile deformation and
161 transposition of layering at the base of the mantle section, which might have accommodated
162 substantial thinning (Prigent et al 2018a, Soret et al 2017).

163

164 While some of the range in temperature and pressure estimates from the metamorphic sole and the
165 Banded Unit peridotites may be due to analytical and methodological uncertainty, or incomplete
166 outcrop and/or incomplete sampling of the highest-grade rocks, some may be due to temporal and
167 spatial variability in peak metamorphic conditions. Moreover, the temperature record in these
168 lithologies may be biased toward peak conditions, rather than later cooling. It is proposed that, at the

169 initiation of subduction near a spreading ridge, hot metamorphic rocks from the footwall are accreted
170 to the hot base of the newly formed mantle wedge, whereas as subduction zones grow colder and
171 develop a steady-state thermal structure, cold dense lithologies in the footwall are subducted rather
172 than accreted to the base of the hanging wall (Agard et al 2016, Soret et al 2017). If so, the
173 metamorphic sole in Oman may record the anomalously high temperatures of subduction initiation,
174 and not lower temperatures during later evolution toward a steady-state subduction zone geotherm. It
175 has been proposed that the relatively low temperatures recorded by the sole in BT1B core could
176 record a point along this cooling path (Kotowski et al 2021).

177

178 A close correspondence between 96 to 95 Ma igneous ages in the crust, and both $^{40}\text{Ar}/^{39}\text{Ar}$ and zircon
179 U/Pb ages of metamorphic rocks along the basal thrust (ca. 96-94 Ma), indicates that thrusting of the
180 Samail ophiolite over adjacent oceanic crust and nearby pelagic sedimentary units began during
181 formation of igneous crust in the ophiolite (e.g. , Garber et al 2020, Hacker & Gnos 1997, Hacker &
182 Mosenfelder 1996, Hacker et al 1996, Rioux et al 2012, Rioux et al 2013, Rioux et al 2016, Rioux et al
183 2021b, Stanger 1985, Styles et al 2006, Tilton et al 1981, Warren et al 2005) or perhaps even earlier
184 (Guilmette et al 2018).

185

186 The base of the sole is truncated by a fault contact with autochthonous, low-grade metasediments of
187 the Hawasina Formation, composed of pelagic clastic units interlayered with limestones (Béchenec
188 et al 1990, Béchenec et al 1988). Relatively high, age corrected $^{87}\text{Sr}/^{86}\text{Sr}$ ratios in the clastic units
189 suggest that they are distal sediments derived from erosion of continental crust (de Obeso et al
190 2021a, Weyhenmeyer 2000), while carbonate units record Sr isotope ratios similar to those of
191 Mesozoic seawater (Weyhenmeyer 2000, Wohlwend et al 2017). These sedimentary units were thrust
192 over Mesozoic to Proterozoic rocks of the Arabian continental margin, forming a “rumpled rug”
193 between the autochthon and the ophiolite throughout northern Oman and the eastern United Arab
194 Emirates.

195

196 *1.4 The “basal thrust of the Samail ophiolite”: A discussion in the introduction!*

197

198 Where the metamorphic sole is preserved, its tectonic contact with the mantle section of the ophiolite
199 represents a paleo-subduction zone at the base of the ophiolite, where the overlying peridotite was
200 “the leading edge of the mantle wedge”, that consumed several hundred kilometers of Tethyan basin
201 and then continental crust before coming to rest on the Arabian continental margin (Béchenec et al
202 1990, Béchenec et al 1988, Breton et al 2004, Cooper 1988, Ninkabou et al 2021, Searle &
203 Robertson 1990, van Hinsbergen et al 2019). Study of these outcrops can illuminate processes in and
204 above a subduction zone that are generally inaccessible to direct observation. Of particular interest
205 are (a) the source of footwall fluids, (b) the nature and mechanism of fluid transport along the thrust
206 fault and into the mantle wedge, (c) chemical, mineralogical and rheological modification of the
207 hanging wall by reaction with footwall fluids, and (d) the mechanisms of subduction zone deformation.

208

209 With this said, subsequent events have affected the wedge, the sole, the underlying sedimentary
210 units, and the faults between them (Grobe et al 2018, Grobe et al 2019). Even during coeval
211 metamorphism of the sole and igneous accretion of the crust in the ophiolite, the relative locations of
212 these two units are uncertain. The parental magmas of the V1 lavas in the ophiolite, with major and
213 trace element characteristics almost indistinguishable from mid-ocean ridge basalts (MORB),
214 crystallized to form most of the crust, particularly in the southern Wadi Tayin and Samail massifs that
215 were the site of all of the OmanDP boreholes. Like MORB worldwide, these magmas probably formed
216 via polybaric decompression melting over a depth interval of 75 km or more (e.g., Allegre et al 1973,
217 Asimow et al 2004, Bottinga & Allegre 1973, Klein & Langmuir 1987, McKenzie & Bickle 1988). Thus,
218 the metamorphic sole (recording peak depths less than 40 km) must not have been directly beneath
219 the spreading center during crustal formation and metamorphism. Instead, the ophiolite section and
220 the metamorphic sole were juxtaposed after crust formation and after peak metamorphism in the sole.

221

222 Moreover, the structural thickness of the Samail ophiolite measured perpendicular to the paleo-
223 seafloor and/or the crust/mantle transition zone, and including both crust and mantle sections, never
224 exceeds ~ 20 to 30 km (Boudier & Coleman 1981, Nicolas et al 2000), corresponding to a pressure
225 less than or equal to ~ 800 MPa, beneath ~ 7 km of crust (on average, Nicolas et al 1996) and ~ 20
226 km of fresh mantle peridotite. Thus, the structural thickness of the ophiolite appears to be at least 10
227 km less than the depth inferred from the high end of the pressure range recorded by the sole (1300 or
228 1400 MPa, ~ 40 to 45 km). In addition, there is no evidence for widespread, tectonic thinning of the
229 crustal section of the ophiolite, either by faulting or ductile deformation.

230

231 How can these data be reconciled? It is possible that the peak pressures inferred for the sole are
232 imprecise, and/or that they represent tectonic “overpressures” that don’t correspond closely with
233 depth (Garber et al 2020). In this interpretation, the metamorphism of the sole could have occurred at
234 ~ 800 MPa, corresponding to the current structural thickness of the ophiolite.

235

236 Alternatively, perhaps the base of the mantle section of the ophiolite underwent tectonic thinning,
237 perhaps via simple shear. Indeed, as summarized by Soret et al. (2017) and Prigent et al. (2018a)
238 and already mentioned in this paper, there is evidence for high strain ductile deformation and
239 transposition of layering at the base of the mantle section, which might have accommodated
240 substantial thinning near the base of the mantle section. Indeed, there is evidence for thinning of the
241 units below the ophiolite (Grobe et al 2018, Grobe et al 2019).

242

243 A third alternative is that some of the lenses of the metamorphic sole – those recording the highest
244 pressures - migrated updip to reach their current structural position, ~ 25 km below the paleo seafloor.
245 Indeed, upward transport of buoyant footwall lithologies during subduction is recorded in many
246 preserved collisional orogens (e.g., Chemenda et al 2000). If so, updip migration of the sole with
247 respect to the overlying ophiolite must have occurred after peak metamorphism but during Tethyan
248 subduction, prior to emplacement of the ophiolite and the sole over the allochthonous Haybi and

249 Hawasina sediments. And, of course, it is possible that the current juxtaposition of the sole and the
250 base of the ophiolite may be explained as the result of combinations of these three alternatives.

251

252 Later processes could also have modified the simple “stratigraphy” described above. In Oman, after
253 Late Cretaceous emplacement of the ophiolite over the allochthonous sediments and autochthonous,
254 Arabian continental margin, large scale uplift formed the gigantic Jebel Akdar and Saih Hatat domes,
255 cored by Proterozoic rocks (e.g., Glennie et al 1973, Glennie et al 1974b). Saih Hatat uplift and
256 cooling started at about 60 Ma, if not earlier (e.g., Grobe et al 2018, Grobe et al 2019, Hansman et al
257 2017). This event reactivated and/or cut the basal thrust of the ophiolite in normal faults and shear
258 zones. Some of these younger faults have juxtaposed mantle peridotite from the ophiolite with the
259 allochthonous sedimentary rocks, or even with the autochthonous units of the Arabian continental
260 margin, along tectonic contacts where the metamorphic sole is no longer present. As will be seen in
261 the following Section (1.5), it can become difficult to distinguish this later deformation, coupled with
262 “reactivation” of existing alteration and formation of new veins, from features formed during
263 subduction at the base of the ophiolite.

264

265 However, despite these complexities, we reiterate that – where it is parallel to banding and foliation –
266 the contact between the metamorphic sole and the overlying Banded Unit at the base of the Samail
267 ophiolite mantle section represents the basal thrust of the ophiolite. In this paper, when we refer to the
268 “basal thrust”, we are referring to contacts that preserve these characteristics. In turn, though of
269 course there can have been imbrication and/or subduction erosion, the basal thrust of the ophiolite
270 was the locus of 100’s of kilometers of subduction of oceanic crust, overlying sediments and,
271 ultimately, the Arabian continental margin, from 96 Ma (or earlier) to ~ 70 Ma.

272

273 *1.5 Geology of MoD Mountain*

274

275 Hole BT1B is on the north side of the wide Wadi Mansah, southeast of “Ministry of Defense
276 Mountain”, (MoD Mtn), which is informally named for the military firing range on the south side of
277 Wadi Mansah in this area. It is close to the saddle between the northeastward plunging end of the
278 Jebel Akdar massif, to the west, and the westward plunging Saih Hatat massif to the northeast (**Figure**
279 **1**). Uplift of these nearby massifs caused reactivation of some older faults, combined with formation of
280 new, younger faults. For example, shallow-level gabbros and sheeted dikes are juxtaposed with
281 mantle peridotite and the metamorphic sole on a steep fault parallel to Wadi Mansah, just south of
282 Hole BT1B (Villey et al 1986, Wilde et al 2002). In another example, Scharf et al. (2020) report early
283 U/Pb formation or cooling ages (60 ± 16 and 58 ± 6 Ma) of calcite veins that cut listvenite, cataclasite
284 and fault contacts between listvenite and post-emplacement, Late Cretaceous conglomerates.

285

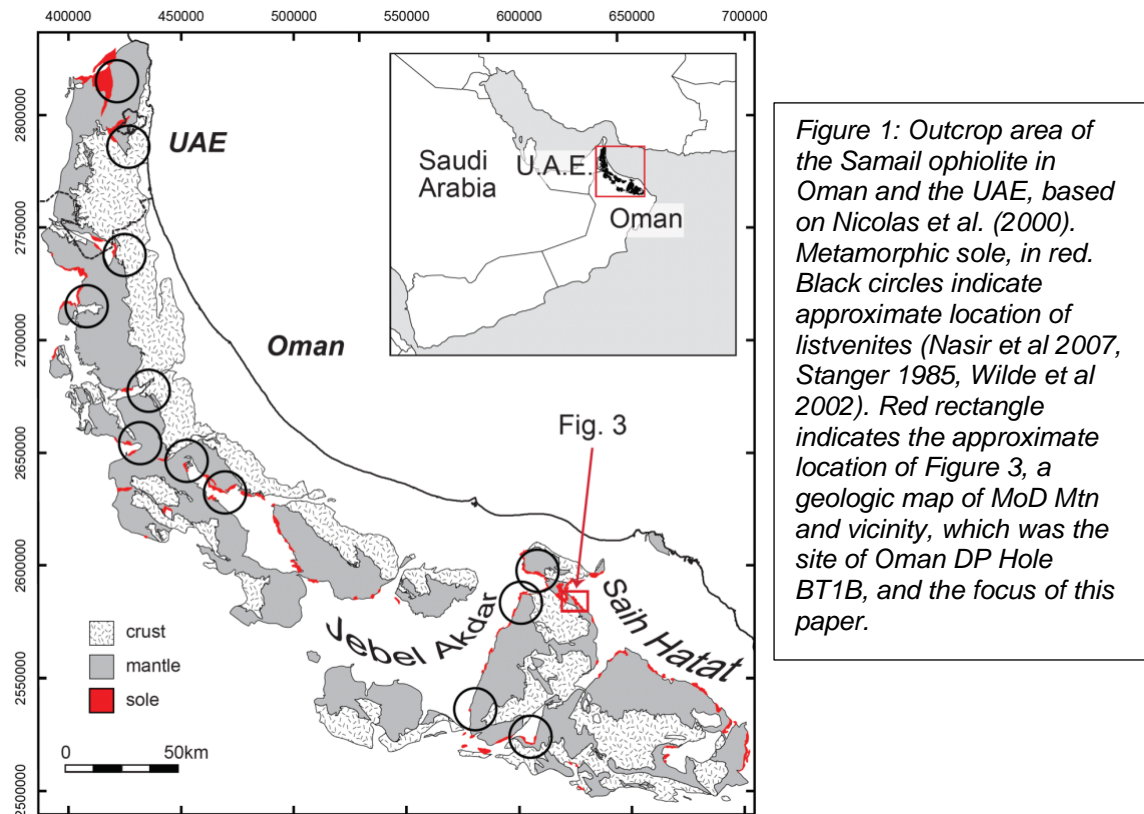


Figure 1: Outcrop area of the Samail ophiolite in Oman and the UAE, based on Nicolas et al. (2000). Metamorphic sole, in red. Black circles indicate approximate location of listvenites (Nasir et al 2007, Stanger 1985, Wilde et al 2002). Red rectangle indicates the approximate location of Figure 3, a geologic map of MoD Mtn and vicinity, which was the site of Oman DP Hole BT1B, and the focus of this paper.

286

287

288 In this context, zircon (U,Th)/He cooling ages on samples from the metamorphic sole SE of Fanjah,
 289 near MoD Mountain, are 38.7 ± 7.7 and 44.4 ± 8.0 Ma, cooling ages of zircons from the metamorphic
 290 sole at the base of the Wadi Tayin massif to the east are 54.5 ± 7.4 and 61.8 ± 2.6 Ma, and the
 291 cooling age of zircons from the lower crust of the Samail massif near Fanjah is 46.4 ± 3.9 Ma
 292 (Supplementary Table 1 and Supplementary Figure 1). It is likely that the listvenites at MoD Mountain
 293 remained above the closure temperature for He diffusion in zircon, $\sim 180^\circ\text{C}$ (Reiners et al 2004), or
 294 were reheated above this temperature, during 30 to 60 million years after formation of the igneous
 295 crust in the ophiolite and peak metamorphism of the sole.

296

297 However, whereas Scharf et al. (2020) reiterate qualitative conclusions from Stanger (1985) and
 298 Wilde et al. (2002) that listvenites near Fanjah postdate ophiolite emplacement, our field observations
 299 are inconsistent with this interpretation. Specifically, in outcrops extending for more than 5 km
 300 northeast of Hole BT1B (Figure 2) there is a relatively regular “stratigraphy”, with variably altered
 301 peridotite overlying the metamorphic sole, in turn overlying Hawasina Formation sediments, all with
 302 low angle fault contacts that have been deformed by a series of gentle, broad open folds (Figure 3). In
 303 contrast, to the northwest and southeast, the outcrop patterns become much more complex, the sole
 304 outcrop thins, and there are some vertical fault contacts where all of these older units are juxtaposed
 305 with Late Cretaceous Al Khod conglomerates and younger, shallow marine limestones (Stanger 1985,
 306 Villey et al 1986, Wilde et al 2002).

307

308 The lowest exposed units in the gently folded sequence NE of Hole BT1B are diagenetically-altered
309 sedimentary rocks, mostly clastic shales and slates with a few meter to 10 meter scale intercalations
310 of limestone and minor lenses of metavolcanic rocks. These are parts of the Hawasina Formation
311 (Béchenec et al 1990, Béchenec et al 1988). Overlying the sedimentary rocks is one of the most
312 aerially extensive outcrops of the metamorphic sole in Oman and the UAE (e.g., Figure 1 and
313 geologic maps in Soret et al 2017, Wilde et al 2002). The outcrop area is unusually large in this region
314 because the unit is regionally flat lying, though broadly folded.
315

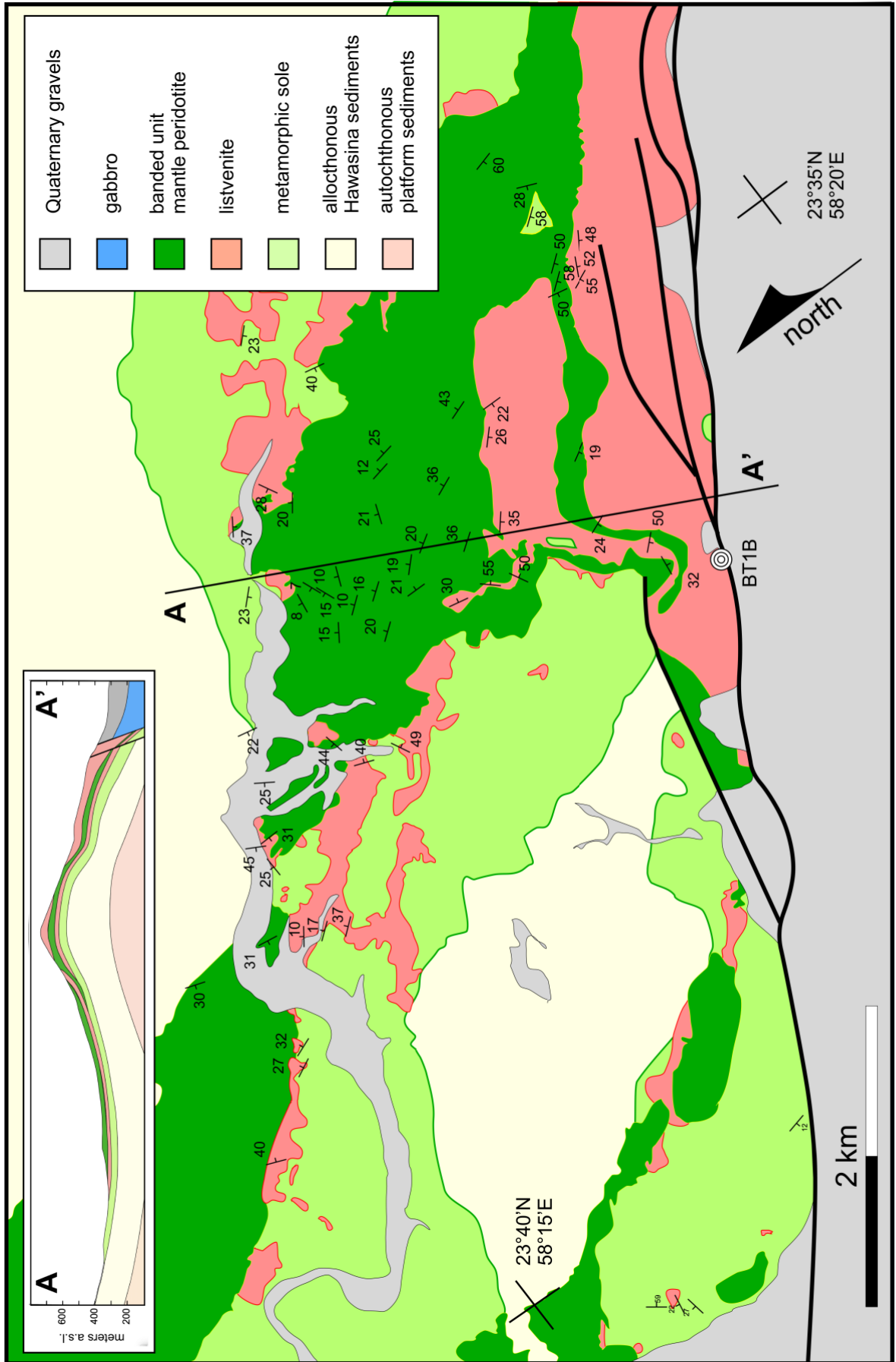


316
317
318 *Figure 2: Photograph of the west end of the MoD Mountain ridge, from the SW, looking NE, showing*
319 *bands of listvenite (rusty orange) parallel to contacts between partially serpentinized harzburgite*
320 *(brown) and dunite (tan) comprising the “Banded Unit” at the base of the Samail ophiolite mantle*
321 *section. Greenish metabasalts and metasediments of the metamorphic sole underlying the ophiolite*
322 *are exposed along indistinct ridge in lower left. The listvenite band at top right is more than 100 m*
323 *thick and extends for 1.5 kilometers along the length of the summit ridge. The listvenite band in the*
324 *center of the photo is 15-20 m thick. Photo taken with a telephoto lens from ~ 23.35°N, 58.17°E, along*
325 *azimuth ~ 030°.*
326

327

328

329 *Figure 3: Geologic map and cross section of MoD Mountain and vicinity. Complex map pattern arises*
330 *from intersection of topography with broadly folded, gently dipping units, as is more evident in the*
331 *cross section (no vertical exaggeration) illustrating the antiform coinciding with MoD Mountain, and*
332 *the syncline to its north. Dips are all measured on lithologic contacts, including dunite/harzburgite*
333 *contacts within the Samail ophiolite mantle section.*



335 Above the metamorphic sole in this gently folded “stratigraphy” is partially serpentized peridotite,
336 composed of distinctive, banded alternations of dunite, harzburgite and lherzolite on a scale of meters
337 to tens of meters, characteristic of the “Banded Unit” that commonly is present at the base of the
338 ophiolite, especially in areas where the contact with the metamorphic sole is preserved (Boudier et al
339 1988, Boudier & Coleman 1981, Lippard et al 1986, Searle & Cox 2002). Indeed, our analyses of
340 partially serpentized mantle peridotites on MoD Mountain, northeast of Hole BT1B, indicate
341 relatively high concentrations of aluminum and other elements (Falk & Kelemen 2015, Godard et al
342 2017). In these peridotites and in listvenites from Hole BT1B, Al contents are strongly correlated with
343 some rare earth element concentrations, characteristics that are distinctly different from typical
344 residual mantle peridotites in the ophiolite, but are typical of the Banded Unit (Godard et al 2000,
345 Khedr et al 2013, Khedr et al 2014, Linckens et al 2011, Prigent et al 2018a, Prigent et al 2018b,
346 Takazawa et al 2003, Yoshikawa et al 2015). The presence of the texturally and geochemically
347 distinct Banded Unit overlying the metamorphic sole is another indication that the area exposes the
348 basal thrust of the ophiolite – the paleo-subduction zone – together with the overlying mantle wedge.

349

350 In some localities, peridotites at the base of the Samail ophiolite mantle section have undergone
351 100% carbonation at 100-250°C to form “listvenites” (Beinlich et al 2020, Falk & Kelemen 2015,
352 Glennie et al 1974a, Manning et al 2018, Nasir et al 2007, Stanger 1985, Wilde et al 2002), in which
353 all Mg and Ca are in carbonate minerals, and silica derived from olivine and pyroxene has formed
354 quartz or chalcedony. In Oman, such listvenites are most abundant on and around MoD Mountain
355 northeast of Hole BT1B, where they form part of the gently folded tectonic “stratigraphy” we are
356 discussing here. Listvenites on the flanks of MoD mountain form discontinuous tabular lenses with low
357 angle dips, 10 to 200 meters thick, parallel to the basal thrust and to lithological banding in the
358 peridotite. These lenses occur along the basal thrust, between mantle peridotite and the metamorphic
359 sole, and enclosed within the peridotite, up to 300 meters above the sole. Contacts in outcrop
360 between listvenite and the surrounding, partially serpentized peridotite are marked by strongly
361 foliated, 100% serpentized zones, 1 to > 20 m thick.

362

363 The lithological banding in the peridotite and the listvenite lenses dip gently south on the south side of
364 MoD Mountain, north on the north slopes of the mountain, and then south again along and NE of the
365 wadi bounding MoD Mountain to the north. Despite later faulting, these structures define a broad
366 anticline with an axis approximately coincident with the summit ridge of MoD Mountain, and a syncline
367 with an axis roughly coincident with the wadi north of MoD Mountain. Listvenites form erosion
368 resistant dip slopes and the tops of small buttes outlining the folded stratigraphy.

369

370 Listvenites elsewhere in Oman and the UAE are found along the basal thrust, commonly juxtaposed
371 with, or within a few km of, the metamorphic sole and/or the Banded Unit at the base of the Samail
372 mantle section, as at MoD Mountain. In some other outcrops, listvenites form lenses within broad
373 serpentinite mélangé zones at the base of the ophiolite (Nasir et al 2007, Stanger 1985). In contrast,

374 listvenites are not found within the peridotite more than a few kilometers away from the basal contact
375 of the ophiolite.

376

377 These observations, together with an imprecise Rb/Sr isochron (97 ± 29 Ma, Falk & Kelemen 2015),
378 that corresponds with the much better determined U/Pb ages of zircon in the metamorphic sole and
379 igneous crust in the ophiolite, indicate that the listvenites formed via transfer of CO₂ and other
380 components from subducting material – probably sediments and/or altered lavas – into the leading
381 edge of the mantle wedge during Tethyan subduction and ophiolite emplacement. This hypothesis is
382 quantified and discussed further in Section 5.

383

384 Not all listvenites form above subduction zones. However, listvenites are found at and near the basal
385 thrust in other ophiolites, worldwide (Akbulut et al 2006, Borojević Šoštarić et al 2014, Escayola et al
386 2009, Menzel et al 2018, Quesnel et al 2016, Quesnel et al 2013, Scarsi et al 2018, Sofiya et al 2017,
387 Ulrich et al 2014). If listvenites commonly form in subduction zones, then the leading edge of the
388 mantle wedge – and subduction modified mantle that has later been incorporated into the continental
389 mantle lithosphere – may be a globally important reservoir for carbon (Foley & Fischer 2017, Kelemen
390 & Manning 2015, Li et al 2017, Scambelluri et al 2016).

391

392 It seems likely that Scharf et al. (2020) will continue to find some of these results and inferences
393 debatable, preferring the hypothesis that listvenites in Oman had nothing to do with subduction, and
394 formed entirely during deformation and fluid flow associated with Tertiary uplift and extension around
395 the Jebel Akdar and Saih Hatat domes. We hope that we've provided a fair and sufficient summary of
396 their views. However, we've also explained why we believe that the evidence indicates that the
397 listvenites formed during subduction and ophiolite emplacement. Thus, throughout the rest of this
398 paper we adopt the view that the contact between the metamorphic sole and the overlying, Banded
399 Unit at the base of the ophiolite mantle section represents the subduction zone beneath the ophiolite,
400 above which listvenites formed at the leading edge of the mantle wedge by reaction of peridotite with
401 CO₂-rich, aqueous fluids produced by devolatilization of subducting sediments and/or altered seafloor
402 lavas.

403

404

2. Methods

405

406

2.1 Geochemistry

407

408 Major, minor and trace element analyses reported in this paper were made by the OmanDP Science
409 Team onboard Drilling Vessel Chikyu, and during laboratory work at the Université de Montpellier
410 generously done by Marguerite Godard and colleagues to check and complete the “shipboard”
411 geochemical dataset. XRF major and minor element analyses of a subset of samples were also
412 conducted at the University of St. Andrews, which allowed cross-calibration with shipboard whole rock
413 data. Methods used to obtain these observations and results are described in the Proceedings of the

414 Oman Drilling Project (Kelemen et al 2020b, Kelemen et al 2020c), hosted online at Texas A&M
415 University by the International Ocean Discovery Program (IODP):
416 <http://publications.iodp.org/other/Oman/OmanDP.html>. Additional data sets are available online at
417 <https://www.icdp-online.org/projects/world/asia/oman/>, and in other repositories linked to those sites.

418

419

2.2 Isotopic measurements

420

421 Sr and C isotope ratios referred to in this paper were conducted at Lamont Doherty Earth
422 Observatory, with analytical information and complete data reported in de Obeso et al (2021a).

423

424

2.3 X-Ray diffraction

425

426 X-Ray diffraction data presented in this paper were collected onboard DV Chikyu, using methods
427 described in Kelemen et al. (2020c).

428

429

2.4 Raman spectroscopy

430

431 Raman analyses of minerals in thin section and rock slabs were conducted at the Raman
432 Microspectroscopy Laboratory, University of Colorado-Boulder with a Horiba Scientific LabRam HR
433 Evolution Raman microscope. Measurements used a 100 mW 532 nm laser, focused through a 50x
434 (0.75 NA) microscope objective onto a ~2 μm spot. The laser power was modulated with neutral
435 density filters to about 15 mW at the sample surface. Multiple (2-10) accumulations were coadded in
436 order to filter spikes and improve signal to noise, and the acquisition time and accumulation number
437 were adjusted to yield appropriate data quality. Data processing was performed using LabSpec 6
438 software (Horiba Scientific), including correction for instrumental artifacts and polynomial baseline
439 fitting/subtraction. Raman mapping was performed using a motorized stage with 2 μm step size, and
440 map datasets were fit using classical least-squares fitting with endmember spectra isolated from
441 regions within the map using LabSpec 6 after data processing.

442

443

2.5 Thermodynamic calculations and modeling

444

445 Thermodynamic modeling of fluid rock reaction was conducted at Columbia University's Lamont
446 Doherty Earth Observatory by Juan Carlos de Obeso and James Leong, in consultation with
447 Kelemen. The speciation and chemical mass transfer code EQ3/6 (Wolery 1992) was used to predict
448 the compositions of coexisting solid and aqueous phases that evolved during interaction between
449 representative lithologies from the MoD Mountain area and CO₂-bearing fluids. Thermodynamic data
450 for minerals were mostly from Berman (1988). Data for pyrite and pyrrhotite were from Helgeson et al.
451 (1978). For aqueous species, thermodynamic data used in the simulations were calculated using the
452 Deep Earth Water (DEW) model (Huang & Sverjensky 2019, Sverjensky et al 2014) which uses
453 recent experimental and theoretical advances (Facq et al 2016, Pan et al 2013) to expand the

454 extended Helgeson-Kirkham-Flowers (HKF) aqueous equation of state (Shock et al 1992, Shock et al
455 1997) to pressures up to 6.0 GPa.

456

457 The composition of 5 wt% aqueous fluid in equilibrium with a pelitic lithology from the Oman
458 Hawasina Formation at 400 – 600°C and 0.5 to 2.0 GPa at low water/rock ratios was used.
459 Specifically, a dilute fluid was equilibrated with the rock composition of sample OM20-17 (de Obeso et
460 al 2021a), containing 0.06 wt% total carbon (Supplementary Table 2). The CaO content of OM20-17
461 was below detection. For this calculation it was assumed to 0.1 wt%. In addition, the S content of this
462 sample has not been measured. For this calculation it was assumed 100 ppm. At these high
463 temperatures and low carbon contents, carbonate minerals are unstable and all carbon in the rock will
464 be mobilized into the fluid phase as dissolved CO₂.

465

466 We calculated the outcome of cooling and decompression of the CO₂-rich fluid from OM20-17, to 100
467 – 300 °C and 0.5 to 2.0 GPa. This had no significant effect on its composition. We then calculated the
468 products of reaction between this fluid and average Oman harzburgite (Supplementary Table 2,
469 calculated from Godard et al 2000, Hanghoj et al 2010, Monnier et al 2006) at 100 – 300 °C and 0.5 –
470 1.0 GPa, at water:rock ratios ranging from 100 to 1. In the models, solid solutions of precipitating
471 minerals were not considered, as the Berman database lacks properties for most Fe-endmembers of
472 minerals commonly observed in listvenites and associated rocks. Thus, for example, the model
473 predicts co-precipitation of pure, endmember magnesite, dolomite and siderite, whereas in listvenite
474 samples we observe Fe-bearing magnesite and dolomite. Among the serpentine polytypes, only
475 chrysotile precipitation was predicted. Our modeling did not include goethite, nor did we use a
476 chromian muscovite component, though solid solutions ranging from fuchsite to chromian muscovite
477 are observed in MoD Mountain listvenites (e.g., Falk & Kelemen 2015).

478

479 Phase equilibrium calculations constraining the conditions for co-existing graphite (\pm amorphous
480 carbon compounds) and hematite, and updated calculations for co-existing antigorite and quartz,
481 were conducted on the drill site and at UCLA using both Thermocalc (Powell et al 1998) and Perple_X
482 (<https://www.perplex.ethz.ch/>) (Connolly 1990, Connolly 2005, Connolly 2009), with the Holland and
483 Powell thermodynamic data for minerals (2003, 1998), and the default equations of state for H₂O-
484 CO₂ fluids (modified versions of Redlich-Kwong). Later, these calculations were repeated at Lamont
485 Doherty Earth Observatory using various versions of SUPCRT (Johnson et al 1992, Zimmer et al
486 2016), thermodynamic data for minerals from Helgeson et al. (Helgeson 1985, 1978) or Berman
487 (1988, plus graphite from Helgeson et al.) and various equations of state for H₂O-CO₂ fluids (Shock et
488 al 1992, Shock et al 1997) modified from Helgeson et al. (1981). All of these different combinations
489 were used, and all provided consistent results.

490

491

492

493

2.6 (U,Th)/He ratio measurements and cooling age calculation

494
495
496
497
498
499
500
501
502
503
504
505
506
507
508
509
510
511
512
513
514
515
516
517
518
519
520
521
522
523
524
525
526
527
528
529
530
531
532
533

All (U-Th)/He analyses were completed at the UTChron facility at the University of Texas at Austin, using aliquots of zircon separates from the metamorphic sole and lower crustal gabbros, previously analyzed for U/Pb ages by Rioux et al. (in prep.), following procedures of Wolf and Stockli (2010). Individual zircon grains were morphometrically characterized to determine alpha ejection correction (Ft, Farley et al., 1996; Cooperdock et al., 2020), equivalent spherical radius (ESR), and estimated mass assuming a tetragonal prism. Single-grain zircon sample aliquots were loaded into Pt tubes for in-vacuo laser He heating for 10 min at ~1200°C by diode laser and 4He concentrations were measured by isotope dilution, using a 3He tracer, on a Blazers Prisma QMS-200 quadrupole mass spectrometer, after cryogenic purification. Blanks and 4He gas standards were run between unknowns to monitor and quantify the procedural baseline during analytical runs. Aliquot laser reheating was repeated (2-5x) until 4He gas yields dropped <1% total extracted gas.

After degassing, individual zircon grains were removed from the Pt packets and dissolved using a two-step HF-HNO₃ and HCl pressure vessel dissolution technique and measured on a Thermo Element2 HR-ICP-MS following the procedure outlined in Wolf and Stockli (2010). U-Th-Sm concentrations were calculated using isotope dilution with an isotopically enriched, mixed U-Th-Sm spike calibrated against a 1 ppb U-Th-Sm gravimetric standard solution and blank-corrected using the average of multiple procedural blanks.

Final (U-Th)/He ages were calculated using blank corrected U, Th, Sm and He measurements for each aliquot. Reported concentrations were determined using the morphometrically determined mass of each aliquot. The reported error for individual (U-Th)/He ages represents standard error (8%) based on long-term intra-laboratory reproducibility of Fish Canyon tuff zircon standard, following the approach of Farley et al. (2001). The reported mean sample ages reflect the arithmetic mean of the aliquot ages and their standard deviations.

2.7 Calibration of XRF core scanner data

XRF core scanner data were collected onboard DV Chikyu, as described in Kelemen et al. (2020b). We used the core scanner to analyze nine listvenite samples from BT1B core, and 14 gabbro samples from Hole GT1A core that had known bulk compositions based on XRF analysis at the University of St. Andrews. While onboard DV Chikyu, we used the St. Andrews data to calibrate the XRF data, as follows: wt% SiO₂ = 0.89 x (scanner wt% SiO₂); wt% MgO = 2.57 + 1.18 x (scanner wt% MgO); wt% FeO^T = 1.048 + (scanner wt% FeO^T)^{0.848}; and wt% CaO = 0.878 x (scanner wt% CaO), where FeO^T indicates all Fe is treated as FeO. Fits are illustrated in [Supplementary Figure 2](#). Okazaki et al. (2021) present a comprehensive analysis of the XRF scanner data, together with X-Ray tomography data for BT1B core.

534
535
536
537
538
539
540
541
542
543
544
545
546
547

2.7 Calculation of mineral volume proportions

Volume proportions of quartz, magnesite and dolomite were estimated from bulk rock compositions and XRF scanner data as follows. Weight fractions of SiO_2 , MgO , FeO^T and CaO were converted to moles in 100 grams of rock using their molecular weights. (For all data reported in this paper, the sum of wt% SiO_2 , MgO , FeO^T and CaO was greater than 90% of the volatile free, bulk rock composition). The number of moles of dolomite were taken to be equal to moles of CaO , moles of magnesite were calculated as moles MgO – moles CaO , and moles of quartz were taken to be equal to moles of SiO_2 . All Fe was inferred to be in Fe-oxides and hydroxides. If the small amounts of Fe in carbonate minerals were included in such a calculation, this would slightly increase the proportions of magnesite and dolomite, relative to quartz. Volumes of each mineral in 100 grams of rock were calculated using their molar volumes. The data were “projected” from Fe oxy-hydroxides by normalizing the volumes of quartz, magnesite and dolomite to 100%.

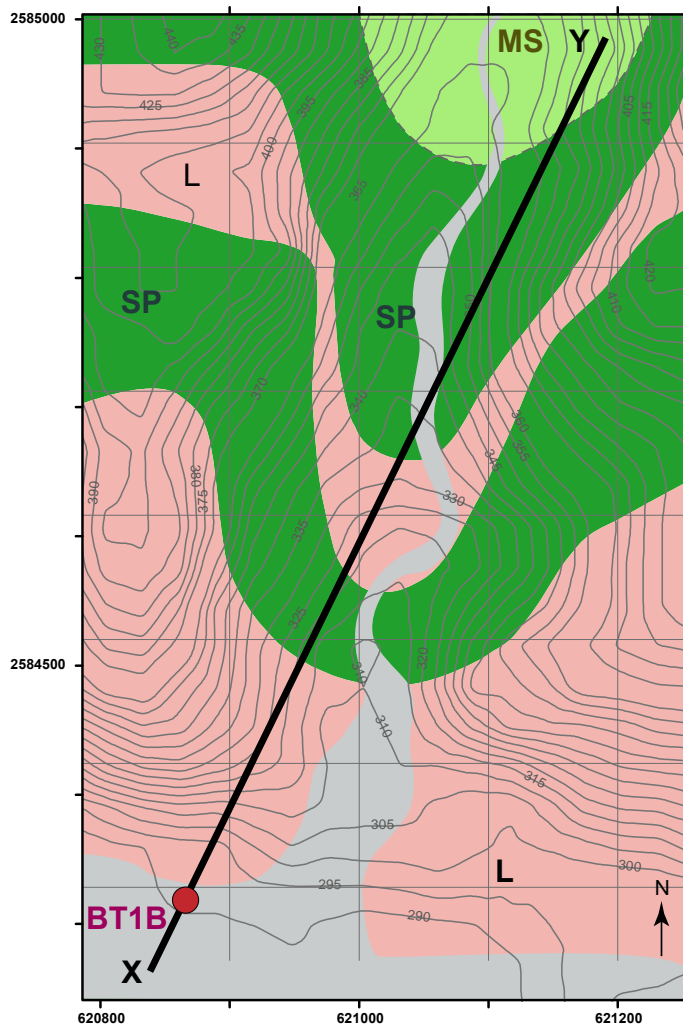
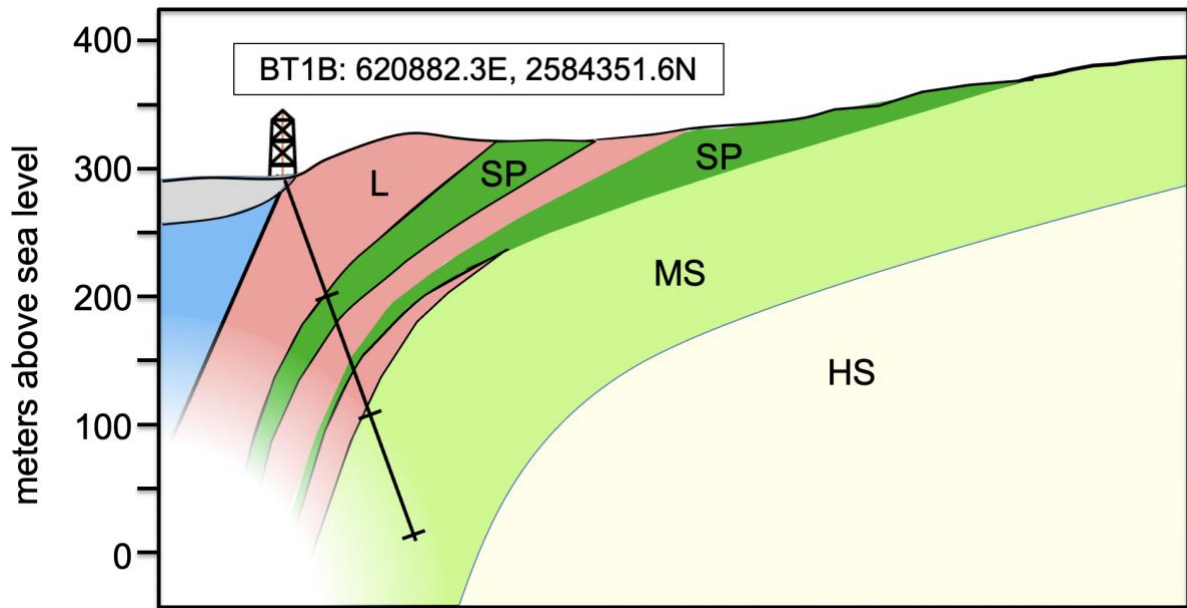


Figure 4: Map and cross section of the area NNE of Oman Drilling Project Site BT1. Yellow, HS: Hawasina sediments; light green, MS: metamorphic sole; rusty red, L: listvenite; dark green, SP: serpentized peridotite; blue: inferred gabbro, based on outcrops south of Wadi Mansah; grey: gravels of Wadi Mansah. UTM coordinates on map are in meters. Cross section has no vertical exaggeration. Map and cross-section modified from Figures F1 and F2 in Kelemen et al. (2020b)

548



549
550
551
552

3. Results

553 To investigate carbon, oxygen and hydrogen mass transfer via transport of subduction zone fluids into
554 the mantle wedge, and to understand low temperature deformation in the leading edge of the mantle
555 wedge at a paleo-plate boundary, we chose to drill at Site BT1. This site is adjacent to a massive
556 outcrop of listvenite, underlain by other bands of serpentinite and listvenite (Figure 4). In turn, these
557 bands overlie the basal thrust of the ophiolite, the metamorphic sole, and – below the depth of drill
558 core sampling – sedimentary rocks of the Hawasina Formation.

559

560 This paper provides an overview of drilling results regarding listvenites and their host serpentinites
561 and peridotites, with an emphasis on a few initial, noteworthy scientific interpretations developed
562 during core description and preliminary thermodynamic modeling. More detailed studies of BT1B core
563 and related topics in this volume focus on scientific interpretations of textural and petrologic data for
564 listvenites (Beinlich et al 2020), listvenite serpentinite contacts (Manning et al. 2021) and the
565 metamorphic sole (Kotowski et al 2021), volume changes during serpentinitization (Malvoisin et al
566 2020), major and trace element geochemistry of all lithologies that allows us to infer the protolith
567 composition and the extent of mass transfer during listvenite formation (Godard et al 2017), Mg-, Sr-
568 and C-isotope geochemistry shedding light on the source of CO₂-bearing fluids and the process of
569 fluid-rock reaction (de Obeso et al 2021a, de Obeso et al 2021b) and both brittle and ductile
570 deformation of the listvenites (Menzel et al 2021, Menzel et al 2020).

571

572 Site BT1 is about 12 km southeast of the village of Fanjah, at 23.364374°N, 58.182693°E, on the
573 north side of the broad channel of Wadi Mansah, which drains mountainous regions to the east and
574 southeast. Hole BT1A penetrated 1.90 meters of gravels in Wadi Mansah, south of listvenite outcrops
575 flanking the Wadi. After we became concerned that a steep hole there might intersect tens of meters

576 of gravel before reaching bedrock, and/or that the gravel might overlie a major, steep fault along Wadi
577 Mansah that postdates ophiolite emplacement, we moved the drill and inclined the Hole. Hole BT1B is
578 three or four meters closer to the listvenite outcrop. The well head is intact, marked and protected
579 from floods by a concrete monument. Drilling of the fine-grained, silica-rich listvenites was
580 challenging, because this lithology has a hardness similar to fine-grained chert or flint (~ 7 on the
581 Mohs' scale), but with patience and expert drilling, we obtained about 100% recovery of all lithologies
582 intersected by the borehole (Figure 5).

583

584

3.1 Lithology

585

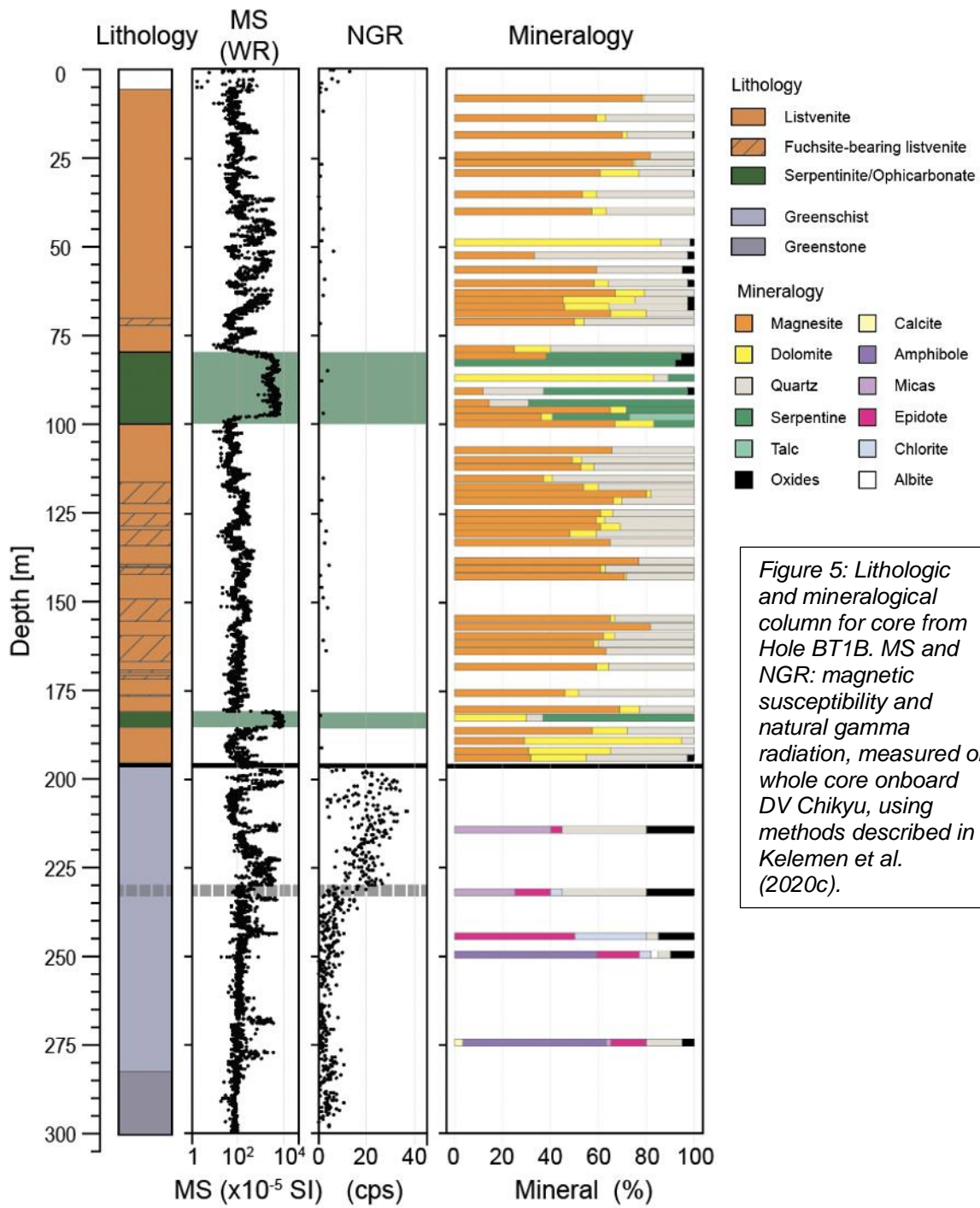
586 As illustrated in Figure 5, the top of the Hole sampled ~ 200 meters of listvenite interlayered with two
587 main serpentinite bands from 80 to 100 m depth, and 181 to 185 m depth. Below 185 m, the listvenite
588 is ubiquitously deformed, with visual core descriptions indicating a mixture of brittle and ductile
589 deformation. At about 197 m below the surface, core was composed of a few tens of cm of soft, clay-
590 rich fault gouge, together with a few cm of hard, aphanitic, black ultracataclasite. Beneath these fault
591 lithologies, the core sampled ~ 102 meters of the metamorphic sole, grading from dominantly fine-
592 grained, finely-banded, muscovite-bearing metasediments at the top ("greenschists" in Figure 5) to
593 coarser, more massive-appearing, foliated "greenstones", interpreted as metavolcanic rocks, at the
594 bottom.

595

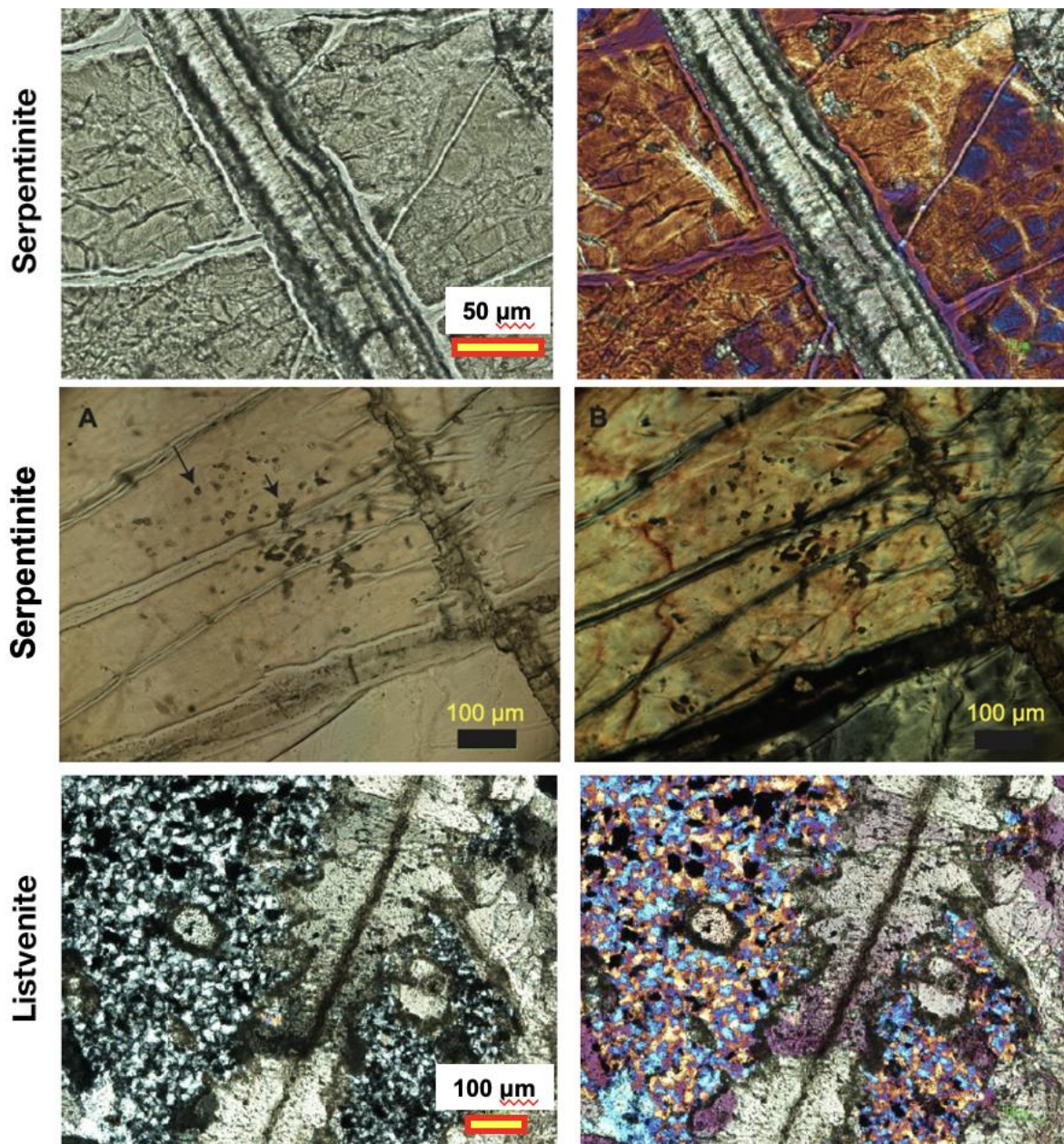
596 Serpentinite bands in the core have gradational contacts with host listvenites over 10's of centimeters
597 to ~ 1 m thick (Manning et al. 2021). Serpentinities contain antitaxial¹ veins of magnesite with a
598 median line composed of hematite and other Fe-oxides. There are prismatic terminations of
599 magnesite crystals away from vein centers, toward the host serpentine (Figure 6). Away from the
600 veins, serpentinites also contain up to 10% magnesite ovoids 10 to 100 microns in diameter, unevenly
601 dispersed within a massive serpentine matrix. These magnesite vein and ovoid textures are abundant
602 in the listvenites as well. Thus, the Shipboard Scientific Party suggested that they are indicative of
603 incipient replacement of serpentinite by listvenite, grading from < 10% carbonate (and no quartz) in
604 veins and ovoids to 100% fine-grained carbonate + quartz across sharp reaction fronts (Kelemen et al
605 2020b). Another notable feature is that some of the serpentinites are optically isotropic in thin section,
606 probably indicative of low temperature formation of poorly ordered or amorphous material with
607 serpentine stoichiometry, sometimes termed "protoserpentine" (e.g., Andreani et al 2004).

608

¹ Antitaxial veins are those whose textures suggest growth of minerals outward from the vein center. They are commonly interpreted to open due to the "pressure of crystallization" (Durney DW, Ramsay JG. 1973. Incremental strain measured by syntectonic crystallization growths. In *Gravity and Tectonics*, ed. KA De Jong, R Scholten, pp. 67-96. New York: John Wiley; Urai, J.L., Williams, P.F. and van Roermund, H.L.M. 1991. Kinematics of crystal growth in syntectonic fibrous veins. *J. Struct. Geol.* 13: 823-836). However, this is less clear in the serpentinites and listvenites of Hole BT1B, where the Mg in the carbonate is derived from the host rocks, and to some degree the veins may replace, rather than displace, the host.



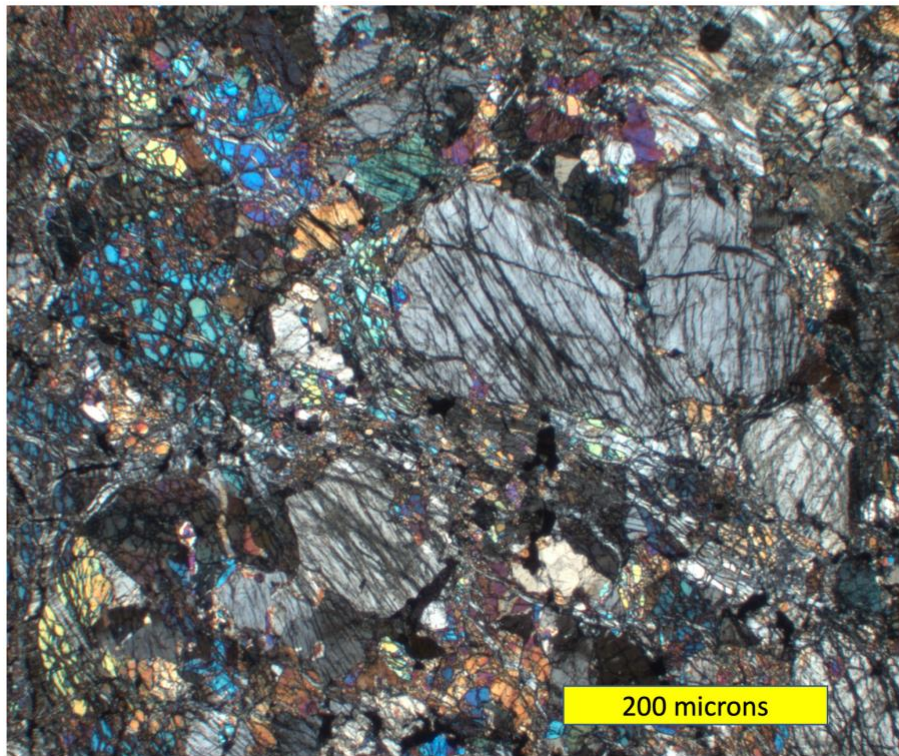
609
610
611



612
613

614 *Figure 6: Magnesite-hematite veins, and magnesite spheroids in serpentinites and listvenites in core*
 615 *from Hole BT1B. Top panels: plane light (left) and crossed-polarized images (right, quartz plate (+1λ)*
 616 *inserted) of magnesite-hematite veins near the lower contact of the upper serpentinite band,*
 617 *TS_BT1B_44Z-3_9-11.5, ~100 m depth, from Figure F47 in Kelemen et al. (2020b). Middle panels:*
 618 *tiny magnesite spheroids in serpentinite, TS_BT1B_44Z-3_9-11.5, ~100 m depth, from Figure F29 in*
 619 *Kelemen et al. (2020b). F. Bottom panels: Cross-polarized images, right one with quartz plate (+1λ)*
 620 *inserted, of texturally similar, “antitaxial” magnesite-hematite veins and magnesite ovoids in quartz-*
 621 *rich, listvenite matrix, TS_BT1B_47Z-3_15-19 at about 110 m depth, from Figure F35 in Kelemen et*
 622 *al. (2020b).*
 623

624 In turn, the listvenites and serpentinites recovered in drill core are hosted by more typical, partially
 625 serpentinized peridotites and dunites in outcrop north and northeast of Hole BT1B (Figure 7). Such
 626 lithologies, typical of the Banded Unit at the base of the mantle section of the Samail ophiolite, are
 627 abundant on the flanks of MoD Mountain, and are particularly well exposed west of the summit
 628 (Figure 2) and on the broad, north facing outcrop below the summit ridge.



630
631
632
633
634
635
636

Figure 7: Cross-polarized image of partially-serpentinized harzburgite sample OM09-14 (Falk & Kelemen 2015) from ~ 10 m above lower listvenite band in Figure 2. Olivine: bright interference colors and irregular, serpentine-filled fractures. Orthopyroxene: grey interference colors and parallel to orthogonal fractures. Minor calcic-pyroxene and/or hornblende are barely visible in this image.

637
638
639
640
641
642
643
644
645

A short sample transect on the ridge forming the drainage divide between Wadi Mansah (site of Hole BT1B) and the parallel wadi north of MoD Mountain documented a sparsely sampled, 5-meter scale progression from listvenite to serpentinite (with intergrown quartz and antigorite) to partially serpentinized peridotite containing relict olivine and orthopyroxene (Figure 5 in Falk & Kelemen 2015). Along that watershed transect, the presence of antigorite – rather than the serpentine polytypes lizardite and chrysotile – was attributed to high SiO_2 -activity produced by reaction of olivine and serpentine to produce carbonate and quartz, since antigorite is more SiO_2 -rich than the other polytypes.

646
647
648
649
650
651
652
653
654

However, the serpentinites in core from Hole BT1B are distinct from the serpentinized zone flanking listvenite, and from the surrounding, partially serpentinized Banded Horizon harzburgites. Although quartz veins cut the serpentinite in the core, antigorite was not observed. Moreover, despite the presence of some orthopyroxene pseudomorphs (“bastites”) in serpentinites, and a concerted effort to find relict mantle minerals, no olivine or pyroxene were detected in drill core. Taken together, field and core observations suggest that the contact between serpentinites and partially serpentinized peridotites is gradational over a few meters at most, approximately as sharp as the contact between listvenites and serpentinites. The shipboard party formed the hypothesis that the serpentinites replaced partially serpentinized peridotites along an “outer” reaction front, farther from the source of

655 CO₂-bearing, aqueous fluids, at the same time that serpentinites were replaced by listvenite along an
656 “inner” reaction front (Kelemen et al 2020b). More on this in Section 4.7, below.

657

658 Essentially, two types of listvenite were recovered, magnesite + quartz + iron oxide lithologies, and
659 volumetrically less abundant, dolomite + quartz + iron oxide rocks, previously termed magnesite-
660 listvenites and dolomite-listvenites, respectively (Falk & Kelemen 2015). Much of the core contains 0.5
661 to 3% relict chromian spinel, partially or fully altered to Fe-oxides. Instead or in addition, some
662 samples contain minor amounts of Cr-rich white mica (fuchsite-muscovite solid solutions,
663 supplementary Figure 7 in Falk & Kelemen 2015), in mm to cm scale, round, microscopic intergrowths
664 with quartz. These intergrowths are macroscopically evident in outcrop and core as cm-scale, ovoid
665 green spots, though in fact Cr-rich mica composes only a few percent of such spots, apparently has
666 undergone alteration to clays in some samples, and was significantly damaged or removed during thin
667 section preparation. This was disappointing, for example because crystals were not large enough for
668 robust ⁴⁰Ar/³⁹Ar analyses. Figure 5 of Nasir et al. (2007) is a photomicrograph of nicely crystalline
669 fuchsite from another listvenite locality in Oman.

670

671 Typical macroscopic listvenite textures are characterized by abundant veins (10 to 200 veins more
672 than 1 mm thick per meter of core, typically ~ 1 per cm) in a fine-grained matrix. In typical, massive
673 listvenites, the fine-grained matrix to ubiquitous veins contains ovoids of either magnesite or quartz
674 (Figure 8). Though they have similar textures, ovoids of the two different minerals are rarely adjacent
675 to each other. Both commonly have Fe-oxides in their cores and/or in spherical zones. Microprobe
676 analyses show that magnesite ovoids have low Fe cores, commonly rimmed with relatively Fe-rich
677 magnesite (Beinlich et al 2020). They have sizes and shapes similar to the quartz spherulites.
678 Carbonate ovoids and cross-cutting magnesite-hematite veins are also observed in serpentinite
679 bands in the core (Figure 6). Thus, the Shipboard Science Party considered it likely that many such
680 veins initially formed within serpentinite, followed by ovoids within surrounding serpentine, and then
681 by later replacement of the entire serpentinite matrix by carbonate + quartz (Kelemen et al 2020b). If
682 so, despite conventional interpretations of veins as relatively young features, “cross-cutting” their
683 matrices, in this case the fine-grained listvenite host may postdate the earliest veins found within
684 them. This hypothesis is discussed further in Section 4.4.

685

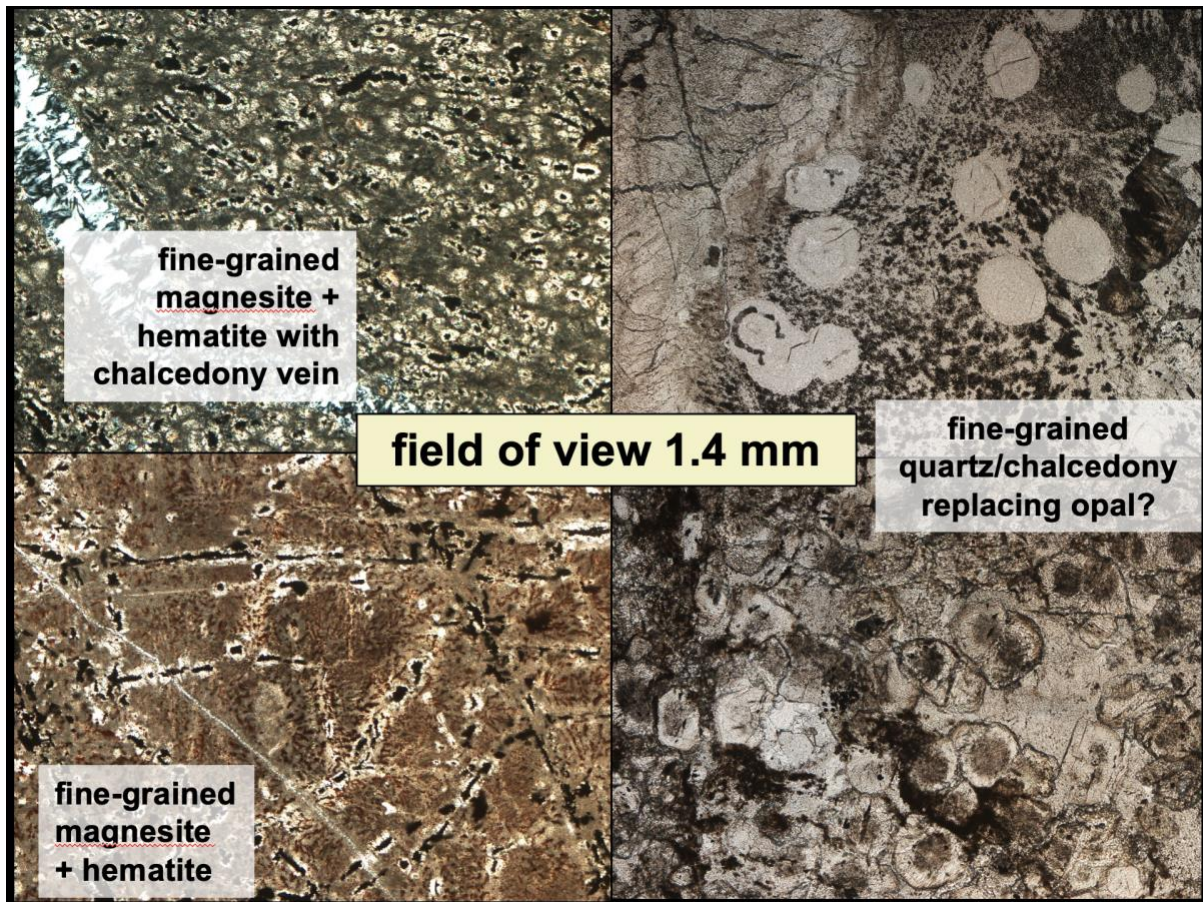
686 The quartz ovoids have the texture of “spherulites”, with radiating microscopic crystals producing a
687 false, “uniaxial interference pattern” in cross-polarized light. Spherulites form during devitrification of
688 amorphous opal as well as rhyolite glass, so Falk & Kelemen (2015) and the Shipboard Science Party
689 (Kelemen et al 2020b) interpreted these as replacing opal, which would have among the earliest SiO₂
690 minerals to form in many of the listvenites. Importantly, opal is commonly found in other listvenites
691 and serpentine-magnesite associations worldwide (Abu-Jaber & Kimberley 1992, Aftabi & Zarrinkoub
692 2013, Akbulut et al 2006, Arisi Rota et al 1971, Barnes et al 1973, Beinlich et al 2010, Borojević
693 Šoštarić et al 2014, Boschi et al 2009, Ece et al 2005, Jurković et al 2012, Lacinska & Styles 2013,

694 Lapham 1961, Oskierski et al 2013a, Oskierski et al 2013b, Posukhova et al 2013, Quesnel et al
695 2016, Searston 1998, Ulrich et al 2014, Zarrinkoub et al 2005).

696

697 Vein types cutting this fine-grained matrix generally record a progression from texturally early,
698 antitaxial magnesite veins – some with cores of hematite + other Fe-oxides (Figure 6) – and related,
699 early Fe-oxide veins, to syntaxial² dolomite veins and carbonate-quartz veins, and lastly to syntaxial
700 calcite veins. Some of the late, syntaxial veins contain vugs lined with prismatic calcite and/or
701 dolomite. A poorly exposed, weathered, fuchsite vein has been observed in outcrop, but no such
702 veins were sampled in BT1B core.

703



704

705

706 *Figure 8: Plane light photomicrographs illustrating magnesite ovoids in a matrix composed of*
707 *magnesite, quartz, and subordinate hematite and Fe-oxyhydroxides, TS_BT1B_20Z-1_42-46, ~ 40 m*
708 *depth (left top) and TS_BT1B_27Z-2_6-8.5, ~ 59 m depth (left bottom), and quartz spherulites with*
709 *carbonate and hematite inclusions, in matrix of fine-grained quartz and hematite with subordinate,*
710 *microscopic carbonates, TS_BT1B_60Z-1_12-17, ~140 m depth (right).*
711

712 Among the Fe-oxide veins, some contain minor sulfide – generally not detected during core

713 description – and amorphous, organic carbon compounds. The carbon compounds were first

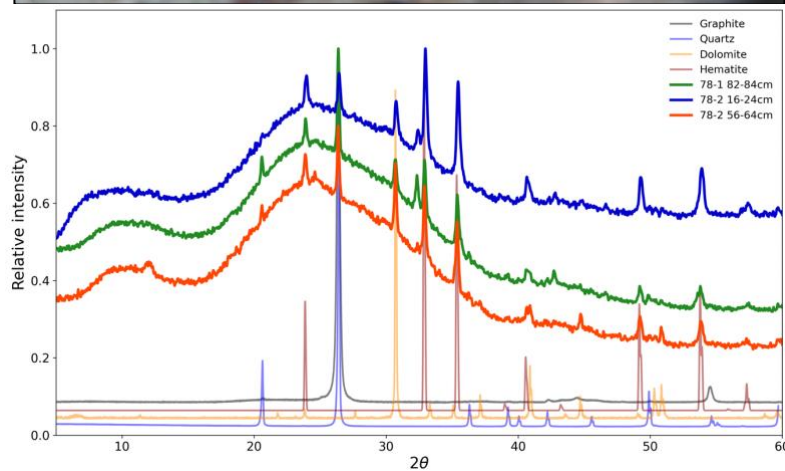
714 identified in core at the drill site, in the lowest listvenite band, as elongate lenses within transposed

² Syntaxial vein textures are associated with inward crystallization of crystals into fractures opened due to external, tensional stresses
ibid..

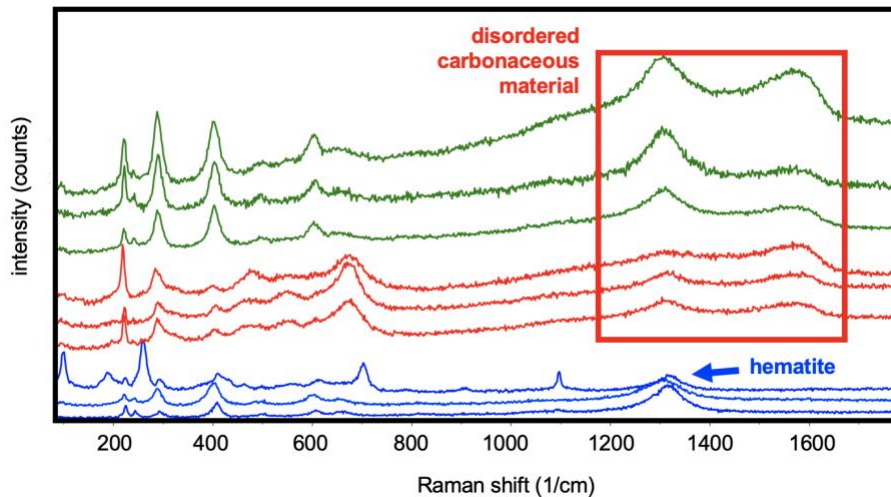
715 hematite veins parallel to the penetrative foliation, where they were described as “graphite”. Soft
716 organic carbon compounds in these features appear to have been largely lost from sample surfaces
717 during washing and handling of the core prior to shipboard observations and analyses, and again
718 during fabrication of thin sections. However, Raman spectroscopy of small, armored relicts, in oxide
719 veins and also in isolated, dark red spots that resemble relict spinel on the core face and rock slabs,
720 reveals the presence of disordered, thermally immature carbonaceous material (Figure 9), some of
721 which may retain a more ordered organic molecular structure. The carbonaceous materials we can
722 still find, on freshly cut surfaces from the core interior, are commonly on the margins of microscopic
723 chalcocite and covellite crystals, in one case also associated with copper sulfate (chalcantite)
724



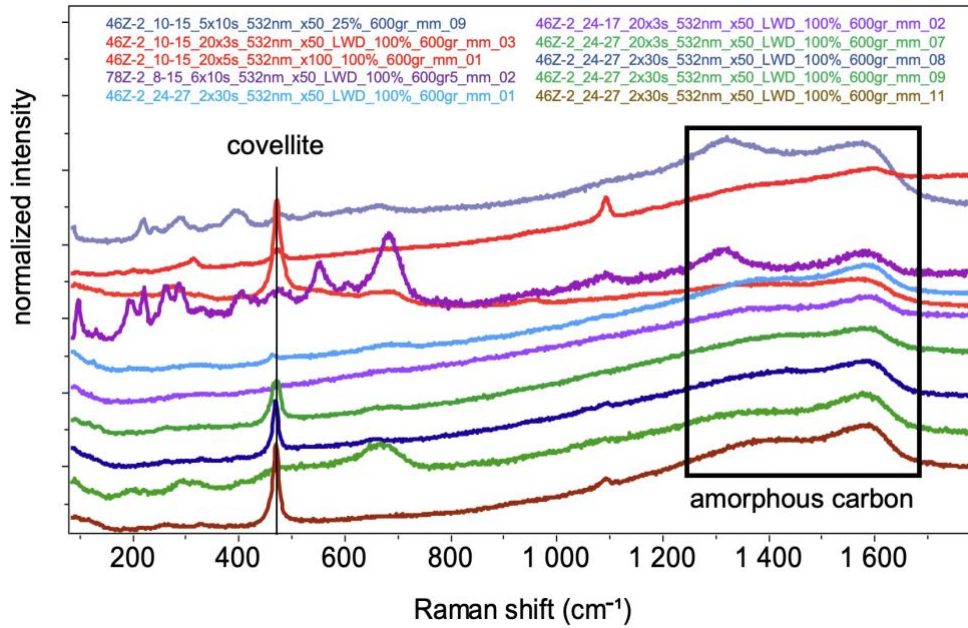
725



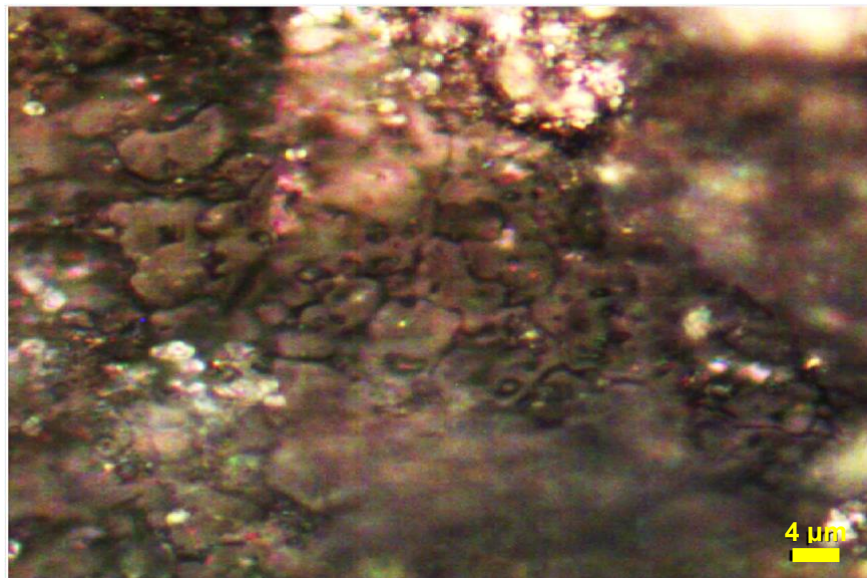
726



727



728



729

730

731 *Figure 9: Carbonaceous material in drill core. Top: Drill site photo of 1 to 2 mm vein of shiny, grey,*

732 *soft material described as graphite on the drill site, in a vein rimmed with hematite. Field of view 5 cm*

733 *wide, core 74Z-01, ~ 195 m depth. Second: Shipboard XRD spectra of soft “graphite” powder*

734 *extracted from veins with “graphite” + hematite, replacing Figure F43 in Kelemen et al. (2020b).*

735 *Interpretation of these data is complicated by the similarity of the quartz and graphite peaks at ~ 26°*

736 *2θ, but quartz also has a prominent peak at ~ 21° which is absent from the blue spectrum for 78Z-*

737 *02_16-24. Third: Raman spectra of black material in samples BT1B_77Z-03_30-38 (blue), 78Z-02_8-*

738 *15 (red) and 78Z-02_50-56 (green, ~ 192-198 m depth. Broad double peaks at wavenumbers of*

739 *~1350/cm and 1600/cm are indicative of disordered carbon compounds; no Raman spectra diagnostic*

740 *of graphite were obtained. Many microscopic, soft, black domains contained hematite, with a single*

741 *broad peak at ~1350/cm, instead of, or in addition to, disordered carbon compounds. Fourth: Raman*

742 *spectra of black material in samples BT1_44Z-02_10-15, BT1_78Z-02_8-15, and BT1_44Z-02_24-27,*

743 *showing broad, double peaks indicative of disordered carbon compounds, some associated with*

744 *covellite. Core 44Z ~ 98 m depth. Bottom image: dark grey copper sulfate “cow pies”, spatially*

745 *associated with brightly reflecting covellite, near amorphous carbon material, field of view ~ 100*

746 *microns, sample BT1_44Z-02_24-27. Data and images from core 44Z are from a 1 mm diameter*

747 *black spot with a red rim in the interior of the core, exposed by the rock saw during sample*

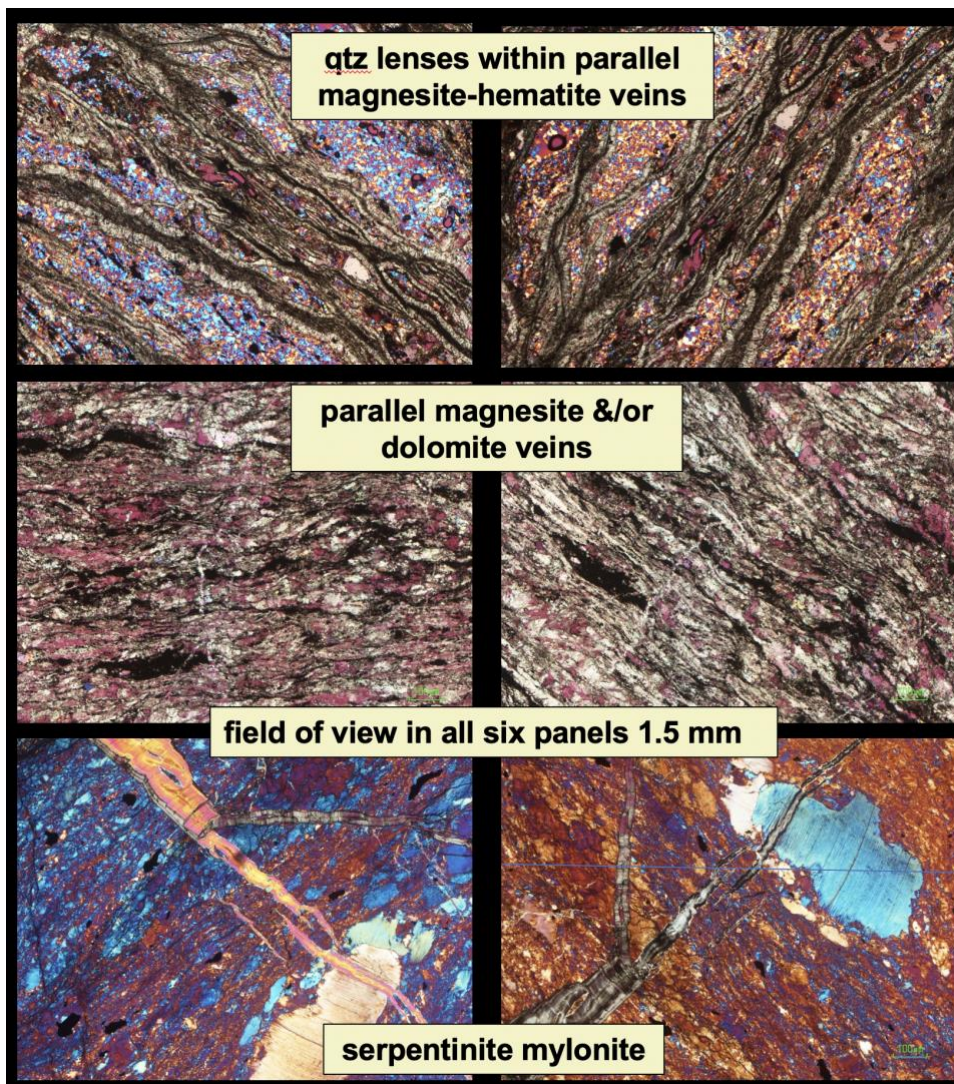
748 *preparation.*

749

750
751
752
753
754
755
756
757
758
759
760
761
762
763
764
765

3.2 Crystallographic preferred orientation of minerals

An overall preferred orientation of veins is not evident from structural data on the core scale, possibly due to differential rotation of core pieces. And, systematic measurements have not been made on the outcrop scale. However, at the meter scale many core intervals contain textures indicative of ductile deformation (Figure 10). Some samples show a strong macroscopic foliation, defined by parallel (possibly transposed) veins enclosing elongate lenses of the fine-grained matrix, in textures commonly interpreted as forming via boudinage during ductile deformation. In samples with a strong foliation defined by dozens of subparallel, early magnesite veins per 10 mm², intervening patches of fine-grained quartz commonly have a crystallographic preferred orientation (CPO). Some samples with a strong foliation defined by abundant, subparallel carbonate veins also have an optically evident, crystallographic preferred orientation in magnesite and/or dolomite within a large number of parallel (transposed?) veins. Similarly, some shear zones in serpentinite have an optically evident, strong shape- and crystallographic-preferred orientation of lizardite crystals, and contain deformed serpentine porphyroclasts.



766
767

768 *Figure 10: Examples of crystallographic preferred orientation (CPO) in localized zones in core from*
769 *Hole BT1B. All images in cross-polarized light with quartz plate inserted. Images on right are of the*
770 *same area as on left, but rotated 90° with respect to the polarizers. Areas showing optical continuity*
771 *have a crystallographic preferred orientation. Top, TS_BT1B_31Z-4_12-14, ~ 65 m depth, quartz*
772 *lenses within sub-parallel, anastomosing magnesite-hematite veins. Middle, TS_BT1B_78Z-2_34-38,*
773 *~ 195 m, thin section composed almost entirely of parallel magnesite and/or dolomite veins, with a*
774 *CPO in the carbonates. Bottom, TS_BT1B_74Z-1_59-62, ~ 183 m, serpentinite mylonite, with a*
775 *strong CPO in the fine-grained matrix, and visible, internal deformation in serpentine porphyroclasts.*
776

777 *3.3 Brittle deformation textures*

778
779 A broad range of different breccias and cataclasites are observed in listvenites and in the
780 metamorphic sole, in outcrop and in core. In turn these are cut by sharp faults – some associated with
781 planar bands and branching veins of aphanitic ultracataclasite and/or pseudotachylite – and by late
782 calcite veins. The nature and interpretation of cataclasites and faults observed in core from Hole
783 BT1B are discussed in detail by Menzel et al. (2020). Based on textural observations, it is clear that
784 the breccias and cataclasites postdate listvenite formation. Some may postdate ophiolite
785 emplacement, and may be broadly related to uplift and extension during formation of the nearby Jebel
786 Akdar and Saih Hatat domes. On the other hand, some could be related to deformation during
787 subduction beneath the ophiolite. At least some of the late calcite veins in core samples, especially
788 those that cut cataclasites, may have formed at the same time as calcite veins with Tertiary U/Pb
789 formation or cooling ages sampled further east, near Fanjah (Scharf et al 2020).

790

791 *3.4 Geochemical data*

792

793 The bulk composition of core samples was measured in five different ways, using procedures
794 described in Kelemen et al. (2020c): (1) Major and minor element compositions of nine samples were
795 measured by XRF at St. Andrews University. (2) Major and minor element compositions of 74
796 samples, including those previously analyzed at St. Andrews, were measured via XRF (both fusion
797 and pressed pellets) onboard the Drilling Vessel Chikyu. (3) Major element compositions of the cut
798 face of selected core sections were analyzed onboard using an XRF core scanner. (4) Trace element
799 compositions of a few samples were analyzed onboard via ICP-MS. (5) Trace element compositions
800 of 61 samples were analyzed via ICP-MS at the Université de Montpellier. These data, and
801 subsequent analyses, are tabulated and described in Kelemen et al. (2020b) and Godard et al.
802 (2017), so for brevity we simply refer readers to those other publications.

803

804 **4. Discussion**

805

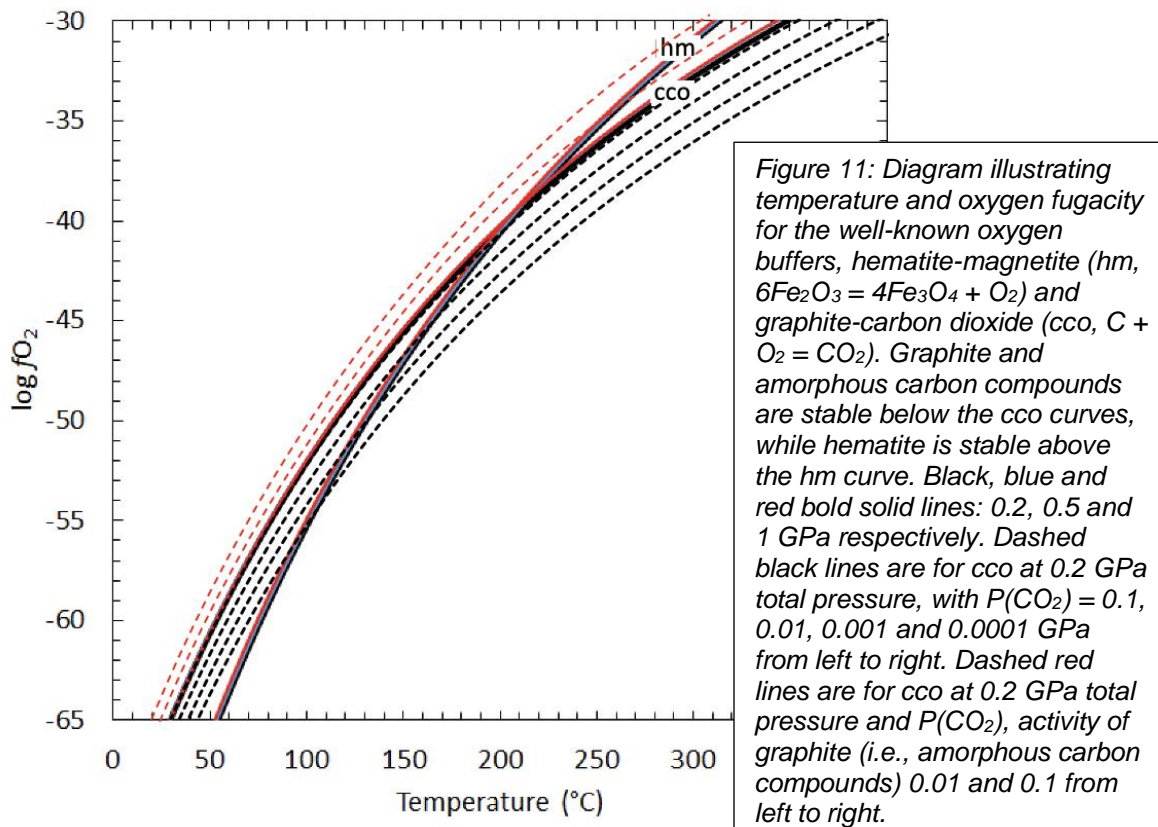
806 *4.1 Temperature and pressure of listvenite formation*

807

808 The temperatures of listvenite formation have been previously constrained using metamorphic phase
809 equilibria, conventional oxygen isotope thermometry, and clumped isotope analyses. Falk & Kelemen
810 (2015) noted the presence of intergrown antigorite (serpentine) + quartz. in the reaction zone between

811 listvenite and serpentinite on the west ridge of MoD Mountain (Figure 2). In some cases, these
 812 samples also contain talc. They used Thermocalc (Powell et al 1998), with thermodynamic data from
 813 Holland and Powell (2003, 1998), and similar methods with the thermodynamic data of Gottschalk
 814 (1997) to estimate that equilibrium coexistence of antigorite, quartz and talc occurs at 80 to 120°C,
 815 depending on the choice and uncertainty of thermodynamic parameters for the minerals, and the
 816 (poorly known) pressure at which these assemblages crystallized. We recently reproduced these
 817 calculations, using Perple_X (<https://www.perplex.ethz.ch/>) (Connolly 1990, Connolly 2005, Connolly
 818 2009) with mineral properties from Holland and Powell. In turn, these temperature estimates are
 819 broadly consistent with temperatures estimated based on $\delta^{18}\text{O}$ in quartz and carbonate minerals in
 820 the listvenite, assuming that fluid $\delta^{18}\text{O}$ was similar to seawater, and with clumped isotope analyses of
 821 magnesite and dolomite yielding temperatures of 80 to 130°C for listvenite samples. Observation of
 822 quartz spherulites in listvenite, possibly reflecting devitrification of opal, also suggest that listvenite
 823 formation occurred in this “low temperature” regime, at ~ 150°C or less, in the presence of aqueous
 824 fluid. However, we should note that our recent calculations, using the Deep Earth Water (DEW) model
 825 (Huang & Sverjensky 2019, Sverjensky et al 2014) or the extended Helgeson-Kirkham-Flowers (HKF)
 826 aqueous equation of state (Shock et al 1992, Shock et al 1997) do not predict equilibrium coexistence
 827 of antigorite + quartz above 15°C.

828



829

830

831 Veins of intergrown amorphous carbon compounds and hematite sampled in the core must have
 832 formed below ~ 200°C (Figure 11). The observation of hydrocarbon species intergrown with oxidized
 833 iron minerals in veins may seem surprising at first, but they are mutually stable at low temperature

834 due to the stronger temperature dependence of the iron oxidation state, compared to the carbon
835 oxidation state. Above $\sim 200^{\circ}\text{C}$, reduced, organic carbon compounds and oxidized iron minerals such
836 as hematite cannot coexist at the same oxygen fugacity, but they can crystallize together at moderate
837 oxygen fugacities below $\sim 200^{\circ}\text{C}$. We've found that this result is robust across all available sets of
838 internally consistent thermodynamic data, and in the pressure range from 0.2 to 1.0 GPa.

839

840 Fourteen more recent clumped isotope analyses for listvenites and carbonate-bearing serpentinites
841 from BT1B core yield an average temperature of $147 \pm 58^{\circ}\text{C}$ (1 sigma). Ten of the 14 temperature
842 estimates lie within the 1 sigma range, whereas two are lower (45 ± 5 and $52 \pm 8^{\circ}\text{C}$) and the two least
843 precise estimates are higher (227 ± 52 and $247 \pm 52^{\circ}\text{C}$) (Beinlich et al 2020). These two high
844 temperatures are closer to those estimated from fluid inclusion studies in some listvenites elsewhere
845 in the world (210 to 280°C , Hansen et al 2005) (208 - 268°C , Madu et al 1990) (250 - 350°C , Schandl &
846 Naldrett 1992, Schandl & Wicks 1991).

847

848 However, though some MoD Mtn listvenites might have formed at temperatures greater than 200°C ,
849 such temperatures are too high for crystallization of intergrown amorphous carbon + hematite, they
850 are (probably) too high for crystallization of intergrown antigorite + quartz, and they are too high for
851 crystallization of opal. Carbonation of peridotite above $\sim 150^{\circ}\text{C}$ would be predicted to form abundant
852 talc + magnesite, whereas talc is absent in MoD Mtn listvenites, and rare but present in serpentinite-
853 listvenite contact zones that are gradational over a few meters (Falk & Kelemen 2015, Manning et al.
854 2021). The range in temperature estimates based on phase equilibrium and clumped isotope ratios
855 from the MoD Mountain listvenites may indicate that mineral assemblages in the listvenites and
856 surrounding serpentinites formed gradually over a range of times and temperatures. In addition, some
857 of the clumped isotope data may record closure temperatures during cooling, rather than the peak
858 temperature at which the MoD Mountain listvenites first crystallized, as proposed for clumped isotope
859 data from fine-grained 10-meter scale magnesite veins in California (Garcia del Real et al 2016).
860 Alternatively, since the highest clumped isotope temperatures from Beinlich et al. are also the most
861 imprecise estimates, perhaps they result from analytical uncertainties or disequilibrium effects. When
862 the clumped isotope temperatures from Beinlich et al. are combined with the 31 older Falk and
863 Kelemen clumped isotope temperatures for MoD Mtn listvenites, the full data set yields an average of
864 $100 \pm 46^{\circ}\text{C}$ (1 sigma).

865

866 The depth of listvenite formation is difficult to constrain. As noted in Section 1.1, the metamorphic sole
867 beneath the Samail ophiolite records peak temperatures up to 700 to 900°C at pressures potentially
868 ranging from 200 to 1400 MPa, indicative of anomalously hot subduction zone conditions. Well
869 studied outcrops of the metamorphic sole record a gradient in peak temperature, with the highest
870 temperatures nearest to the fault contact with overlying peridotites, declining to 400 - 500°C within a
871 few hundred meters below the fault (Cowan et al 2014, Garber et al 2020, Ghent & Stout 1981,
872 Hacker & Gnos 1997, Hacker & Mosenfelder 1996, Searle & Cox 1999, Searle & Cox 2002, Searle et
873 al 1980, Searle & Malpas 1980, Searle & Malpas 1982, Soret et al 2017). However, in BT1B drill core,

874 the metamorphic sole records peak conditions of 450 to 550°C and 800 to 1200 MPa (Kotowski et al
875 2021).

876

877 The current structural thickness of intact sections of oceanic crust and upper mantle provides another
878 constraint on the depth of listvenite formation. The crust is ~ 5 to 7 km thick in most sections (Nicolas
879 et al 1996), and the base of the mantle section where the Banded Unit is observed is ~ 20 km below
880 the crust-mantle transition zone, based on estimates derived from the dip of the mantle-crust
881 transition zone (MTZ) and the horizontal distance from the MTZ to the basal thrust (e.g., Boudier &
882 Coleman 1981), yielding a structural thickness of ~ 25 km.

883

884 As noted in the introduction, either the published range of pressure estimates for the metamorphic
885 sole is the result of uncertainty rather than true variation in depth, or the lower few km of the ophiolite
886 mantle section has undergone thinning in some places, or the lenses of the metamorphic sole
887 recording the highest pressures migrated upward with respect to the overlying peridotite. Also, we
888 infer from Sr isotope data that the fluids that formed the listvenites were not derived from the
889 metamorphic sole (Section 4.3, below, and de Obeso et al 2021a). For all of these reasons, it is
890 unclear how the metamorphic pressures inferred for the sole constrain the depth of listvenite
891 formation. However, temperatures and pressures recorded by the sole do provide a window into the
892 thermal evolution of subduction beneath the ophiolite.

893

894 Initiation of subduction, during formation of the metamorphic sole, probably involved thrusting of a hot
895 mantle wedge over newly formed, hot basaltic crust. Over time, subduction of progressively older
896 oceanic crust and – eventually – the pelagic sediments of the Hawasina Formation, would have
897 caused cooling of the subduction zone as it evolved toward a steady state geotherm for oceanic
898 subduction zones. A few clumped isotope analyses on calcite in sediments beneath the ophiolite and
899 the metamorphic sole on MoD Mountain yield temperatures of 150 to 200°C (Falk & Kelemen 2015). It
900 is possible that these were peak temperatures during diagenesis of the sediments along a subduction
901 geotherm at the pressure and depth recorded by the underlying metamorphic sole in core from Hole
902 BT1B, 800 -1200 MPa, or about 25 to 40 km.

903

904 In turn, even lower temperatures recorded in most listvenite samples may record continued, isobaric
905 cooling of rocks flanking the subduction zone. Temperatures of 100 to 200°C at depths of 25 to 40 km
906 are inferred for fore-arc regions above subduction zones from heat flow data (reviewed in Peacock
907 1996) and predicted for steady state, oceanic subduction geotherms in numerical models (e.g.,
908 Peacock 1996, Peacock et al 2005, Syracuse et al 2010), including those recently modeled by Van
909 Keken et al. (2019). Such conditions also lie within the cold end of the range of PT conditions
910 recorded by subduction-related metamorphic rocks (Hacker 1996, Hacker 2006, Penniston-Dorland et
911 al 2015). Such low temperatures at 25 to 40 km are rare or absent in other tectonic environments.

912

913 It is possible that the sediments and the overlying mantle peridotites at the base of the ophiolite were
914 juxtaposed by subduction at the leading edge of the mantle wedge, at a depth of 25 to 40 km, and
915 that the MoD Mountain listvenites formed at these depths. Alternatively, if the metamorphic sole has
916 migrated updip with respect to the overlying peridotites, then the listvenites could have formed at
917 lower pressures and shallower depths.

918

919 *4.2 Composition of listvenite protolith and geochemical fluid additions*

920

921 Given the abundance and variety of mineralogically simple veins, many of which are monomineralic,
922 there is substantial compositional variation in listvenites at the millimeter to meter scale. This
923 variability extends to larger scales in some parts of the core. Nevertheless, remarkably enough,
924 average $\text{MgO}/\text{SiO}_2/\text{FeO}^*$ (all Fe as FeO) ratios in the listvenites are very similar to those in average
925 residual peridotites from the ophiolite (Figure 12), as discussed further by Okazaki et al. (Okazaki et al
926 2021). These oxides comprise more than 90% of the volatile-free bulk composition of the rock. On the
927 other hand, of course, serpentinites and listvenites record addition of tens of weight percent H_2O and
928 CO_2 to the original bulk composition of mantle peridotite protoliths. Thus, either congruent dissolution
929 removed major elements in their original proportions in the peridotite, or the rocks record a large
930 increase in the solid mass, due to addition of volatiles with little or no export of dissolved major
931 elements, on the scale of meters to hundreds of meters. More on this below.

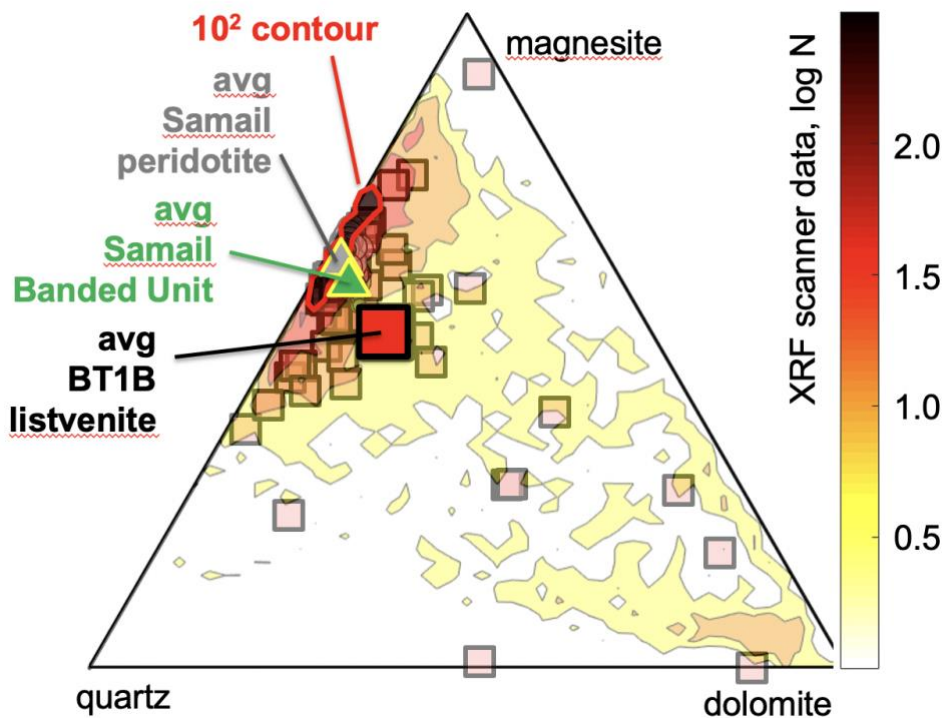
932

933 In addition to CO_2 , dolomite listvenites clearly record substantial addition of CaO, and – since CaO
934 and Sr concentrations are strongly correlated – of Sr as well. Although the shipboard data do not
935 reveal systematic variation in the abundance of magnesite vs dolomite listvenites downhole, there is a
936 clear change in the abundance of both Al and K, together with many other highly incompatible trace
937 elements. Concentrations of these elements are relatively low above the serpentinite band at 80-100
938 m depth, and much higher below that band (Godard et al 2017; Kelemen et al 2020b). Understanding
939 the source for enrichment in these elements is complicated by uncertainty about their concentration in
940 the peridotite protolith.

941

942 As noted above, “Banded Units” of alternating dunite, harzburgite and lherzolite characterize the base
943 of the ophiolite mantle section in many regions, including several where the presence of the
944 underlying metamorphic sole indicates that the base of the mantle section is the paleo-subduction
945 zone. Some Banded Unit peridotites record high temperature geochemical refertilization of residual
946 mantle peridotites by reaction with infiltrating melt or fluid at $> 800^\circ\text{C}$, with addition of calcic pyroxene
947 and Mg-rich hornblende, corresponding to geochemical enrichment in CaO and Al_2O_3 to levels well
948 above those observed in average residual mantle peridotites in the Samail ophiolite. Indeed, four out
949 of six harzburgite samples from banded harzburgites and dunites on MoD Mountain, the protolith for
950 the serpentinites and listvenites in BT1B core, have Ca and Al contents outside the 1 sigma range of
951 variability in residual mantle peridotite in the ophiolite (Falk & Kelemen 2015, Godard et al 2017;
952 Kelemen et al 2020c). In the listvenites below 100 meters depth in core from Hole BT1B, as in

953 enriched peridotites in the Banded Unit, many trace elements are significantly enriched compared to
 954 average Samail ophiolite mantle peridotites, and have trace element ratios that are distinct from
 955 typical peridotites, but characteristic of the Banded Unit (Fig. 12 and Godard et al 2017), as shown in
 956 **Figure 13**. In particular, middle to heavy rare earth element ratios in the Banded Unit, and in the
 957 listvenites, are high compared to typical Samail peridotite. Such relative enrichment in middle rare
 958 earth elements is commonly associated with the presence of igneous hornblende in peridotites, and
 959 the listvenites probably inherited these characteristics from their enriched, Banded Unit protolith. On
 960 the other hand, it is clear that most listvenites have higher Sr concentrations than typical Samail
 961 ophiolite peridotites *and* the Banded Unit (de Obeso et al 2021a). Instead, Sr and Ca were added
 962 during low temperature alteration, along with H₂O and CO₂. These topics are discussed further in
 963 Godard et al. (2017).
 964



965
 966
 967 *Figure 12: Ternary diagram illustrating relative volume proportions of quartz, magnesite and dolomite,*
 968 *projected from hematite, calculated from whole rock compositions, for Samail ophiolite mantle*
 969 *peridotites (large, grey open circles, barely visible, Godard et al. 2000; Monnier et al. 2006; Hanghoj et*
 970 *al. 2010}, Banded Unit peridotites near the base of the Samail ophiolite mantle section (small, green*
 971 *open circles, barely visible, Falk & Kelemen 2015, Khedr et al 2013, Khedr et al 2014, Takazawa et al*
 972 *2003), and listvenites from Hole BT1B and MoD Mtn (open squares, Falk & Kelemen 2015, Kelemen*
 973 *et al 2020b), superimposed on contoured histogram of mineral proportions from shipboard XRF*
 974 *scanner data. Contour interval 10^{1/2}. Okazaki et al. (2021) provide a more thorough view of the XRF*
 975 *scanner data, together with shipboard X-Ray Computed Tomography data on the whole core.*
 976

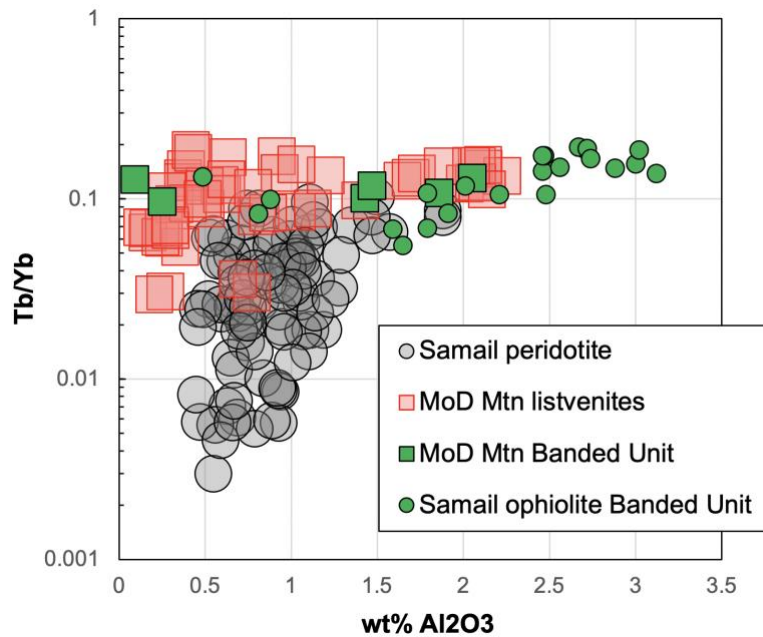


Figure 13: Weight percent Al_2O_3 versus Tb/Yb ratios in bulk rock compositions of MoD Mtn listvenites (open squares, Falk & Kelemen 2015, Godard et al 2021, Kelemen et al 2020b), and MoD Mtn peridotites that host listvenites (green squares, Falk & Kelemen 2015, Godard et al 2021), compared to typical Samail ophiolite mantle peridotites (grey open circles, Godard et al 2000, Hanghoj et al 2010, Monnier et al 2006), and Banded Unit peridotites from the base of the Samail ophiolite (Khedr et al 2013, Khedr et al 2014, Takazawa et al 2003).

977

978

979 Present day Sr isotope ratios in listvenites and serpentinites from MoD Mtn range from ~ 0.708 to
 980 0.715 (de Obeso et al 2021a, Falk & Kelemen 2015). Using current Rb/Sr contents in these samples,
 981 age corrected $^{87}Sr/^{86}Sr$ ratios at 96 Ma range from ~ 0.708 to 0.714, much higher than the range of Sr
 982 ratios in Samail ophiolite peridotites (0.703 to 0.707, Benoit et al 1999, Gerbert-Gaillard 2002,
 983 Gregory & Taylor Jr 1981, Lanphere et al 1981, McCulloch et al 1980, McCulloch et al 1981), the
 984 range in Late Cretaceous to modern seawater (~ 0.7075 to 0.7081), or the range in peridotite-hosted
 985 ground water in the Samail ophiolite (~0.7065 to 0.7092, Weyhenmeyer 2000). Together with
 986 correlated, elevated Sr and Ca contents, the OmanDP Science Team inferred that the Sr-, Ca- and
 987 CO_2 -rich fluid(s) that modified the mantle overlying the basal thrust of the ophiolite had relatively high
 988 $^{87}Sr/^{86}Sr$ ratios compared to fresh, residual mantle peridotites.

989

990 Initially, many members of the OmanDP Science Team expected that the metamorphic sole, as
 991 sampled by core from Hole BT1B, might be the source of fluids that formed the listvenites in the
 992 overlying peridotites, or at least might be analogous to the source of these fluids. However, this is not
 993 consistent with the Sr isotope data on the sole in core from Hole BT1B. Measured and age-corrected
 994 Sr isotope ratios in the metamorphic sole are consistently lower than corresponding ratios in the
 995 listvenites.

996

997 Instead, pelagic, clastic units of the underlying Hawasina sedimentary rocks have measured and age-
 998 corrected Sr isotope ratios that span the same range as those in the listvenites (de Obeso et al
 999 2021a). Thus, these sedimentary units in the Hawasina may be analogous to subducted sedimentary
 1000 rocks that produced the CO_2 -bearing fluids that formed the MoD Mtn listvenites. Indeed, there is
 1001 evidence for a deeply subducted component with terrigenous isotope characteristics – like those of
 1002 the Hawasina sedimentary rocks – elsewhere in the Samail ophiolite. A series of felsic intrusions in
 1003 the sole, mantle and lower crust along the length of the ophiolite have low, age-corrected $^{143}Nd/^{144}Nd$

1004 (and thus, presumably, high $^{87}\text{Sr}/^{86}\text{Sr}(t)$), attributed to melting of high-grade metasediment in the
1005 subduction zone below the ophiolite (Amri et al 2007, Briquieu et al 1991, Cox et al 1999, Haase et al
1006 2016, Haase et al 2015, Lippard et al 1986, Rioux et al 2021a, Rioux et al 2013, Rioux et al 2021b,
1007 Rollinson 2015, Spencer et al 2017).

1008

1009

4.3 Source of fluid for listvenite formation

1010

1011 As noted above, clastic units in the Hawasina formation have Sr isotope ratios that are higher than
1012 those of Samail ophiolite serpentinites and peridotites, and higher than in the metamorphic sole, but
1013 overlap those of the MoD Mtn listvenites. Thus, we infer that those units are analogous to the source
1014 of the CO_2 -bearing fluids that formed the listvenites. This is likely, despite the presence of C- and Sr-
1015 rich limestone and dolomite units in the Hawasina, because devolatilization of clay and mica bearing,
1016 clastic metasediments produces abundant, CO_2 -rich aqueous fluids, while limestone and marble
1017 remain relatively refractory at low to moderate temperature, subduction zone conditions (e.g., Kerrick
1018 & Connolly 2001, Stewart & Ague 2020).

1019

1020 However, the clastic units in the Hawasina formation have $d^{13}\text{C}$ less than -4 per mil, whereas
1021 listvenites have $d^{13}\text{C} > -3$ per mil. These differences in carbon isotope ratios can be understood as
1022 the result of temperature dependent carbon isotope fractionation. As discussed in more detail in de
1023 Obeso et al. (2021a), at temperatures greater than $\sim 300^\circ\text{C}$, dissolved CO_2 in aqueous fluids has $d^{13}\text{C}$
1024 higher than co-existing calcite and dolomite (Deines 2002, Horita 2014). At lower temperatures,
1025 calcite and dolomite have $d^{13}\text{C}$ higher than co-existing fluids. Dolomite and magnesite crystallized at
1026 relatively low temperature, from aqueous fluids that acquired their carbon isotope ratios during higher
1027 temperature devolatilization of Hawasina clastic sediment compositions, would have $d^{13}\text{C}$ in the range
1028 of 1.0 to -3.0‰, as observed in the MoD Mtn listvenites. In addition, low carbon solubilities in low
1029 temperature, low pressure aqueous fluids saturated in carbonate minerals in mineral assemblages
1030 similar to those in the Hawasina clastic sedimentary rocks (Fig. 22 and associated text in Chapter 4,
1031 Falk 2014, Kelemen & Manning 2015) have been inferred and/or calculated to be insufficient to
1032 produce the MoD Mtn listvenites (de Obeso et al 2017, Falk & Kelemen 2015).

1033

1034 Based on the data and reasoning described in the previous paragraph, we favor a process in which
1035 higher temperature, subduction zone devolatilization produced CO_2 -rich aqueous fluids that then
1036 cooled and decompressed by flow up the subduction zone, to react with peridotite at less than 200°C
1037 to produce the MoD Mtn listvenites. To quantify this hypothesis, we made thermodynamic calculations
1038 with the compositions of solid reactants given in **Supplementary Table 2**, methods described in
1039 Section 2, and results outlined in Figures 14 and 15. As the source of fluid, we chose sample OM20-
1040 17, a pelitic end-member from among the Hawasina clastic sedimentary rocks analyzed by Falk &
1041 Kelemen (2015) and de Obeso et al. (2021a). As the peridotite reactant, we used an average Samail
1042 harzburgite composition calculated from published studies (Godard et al 2000, Hanghoj et al 2010,
1043 Monnier et al 2006).

1044
1045
1046
1047
1048
1049
1050

Devolatilization of clastic Hawasina sediments similar to OM20-17 is predicted to produce fluids with ~ 20,000 ppm dissolved C after exhaustion of carbonate minerals at ~ 400°C at 0.5 GPa to ~ 500°C at 2 GPa (Figure 14). Closed system decompression and cooling of this fluid to 100 to 300°C, and 0.5 to 1 GPa produced no significant change in the composition of this modeled fluid. Modeling open system transport of this fluid, updip along a subduction zone geotherm, is beyond the scope of this paper.

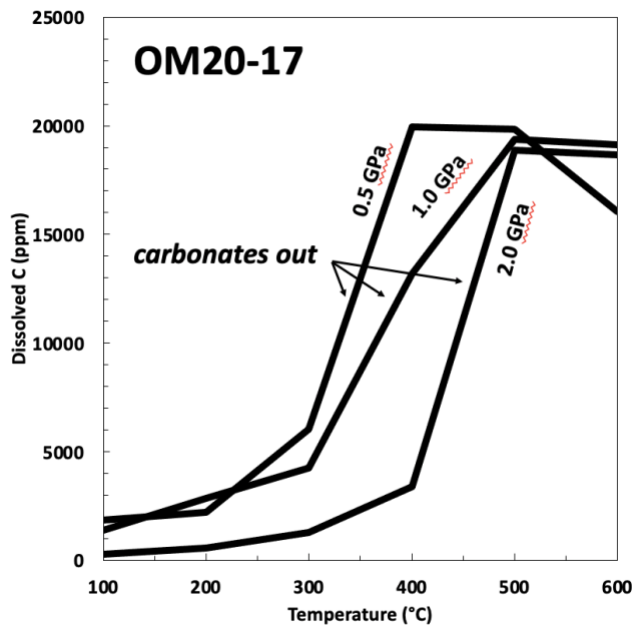


Figure 14: Calculated dissolved carbon concentration in fluid in equilibrium with Hawasina sediment sample OM20-17 at a water/rock ratio of 5%, as a function of temperature and pressure.

1051
1052
1053
1054
1055
1056
1057
1058
1059
1060
1061
1062
1063
1064
1065
1066
1067
1068
1069
1070

Reaction of this model fluid with peridotite at 100-300°C and 0.5 to 1.0 GPa is predicted to produce mineral assemblages similar to those modeled by Klein and Garrido (2011): Small masses of “birbirite” (silicified peridotite) at high water/rock ratios and/or low temperatures, through moderate masses of listvenite and soapstone (talc-carbonate rocks) at moderate water/rock and temperature, to relatively large masses of carbonate-bearing serpentinite at low water/rock ratios and/or high temperature (Figure 15). Predicted magnesite and quartz proportions correspond closely to observed proportions in MoD Mtn listvenites (Figure 12). Most of the PT conditions produced small amounts of hematite coexisting with magnesite and quartz, as observed. Predicted magnesite and siderite proportions correspond to a solid solution with ~ 8 wt% FeO, which is a few wt% higher than observed in MoD Mtn listvenites. Most modeled conditions produced dolomite in listvenite assemblages at water/rock ratios at water/rock ratios less than 10 (log water/rock = 1), consistent with the presence of relatively late, cross-cutting dolomite-bearing veins in the listvenites. Most model runs produce small amounts of kaolinite, and very limited proportions of muscovite in listvenite mineral assemblages, whereas chromian white mica is thought to be common in MoD Mtn listvenites, and listvenites worldwide. It is possible that addition of a thermodynamic model for fuchsite would yield stable white mica, rather than kaolinite, over a wider range of temperature and water/rock ratios. Alternatively, perhaps some green sheet silicates in listvenites are chrome-bearing clays rather than true micas. Thus, thermodynamic modeling suggests that the CO₂-bearing aqueous fluids that formed the MoD

1071 Mountain listvenites formed by metamorphic devolatilization in a subduction zone at > 400°C. These
1072 fluids then migrated updip to react with peridotite at the leading edge of the mantle wedge, probably at
1073 a depth less than 40 km. However, this is just a forward model, and there may be other possibilities.

1074

1075

4.4 Listvenite formation

1076

1077 Subhorizontal lenses of listvenite at MoD Mountain contain a cumulative mass of about 2 billion tons
1078 of CO₂ over a strike length of 2 km NS, and 5 km EW, corresponding to 1 million to 400,000 tons of
1079 CO₂ per m along strike. The allochthonous sedimentary units below the ophiolite are about 3 km thick.
1080 Within these, clastic units comprise at least half the section, and contain about 2300 ppm C, or 0.84
1081 wt% CO₂ on average (de Obeso et al 2021a), yielding a total of about 35 tons CO₂ per m along strike,
1082 per m subducted. (As noted above, rocks composed mainly of calcite and/or dolomite in the
1083 subducting sedimentary section would be unlikely to contribute significant amounts of CO₂ to
1084 subduction fluids at temperatures less than 800°C). At subduction velocities of 0.05 to 0.1 m/year,
1085 90% decarbonation of the clastic units in the Hawasina Formations with a density of 2.75 tons/m³, at ~
1086 400-500°C would produce at least 1.7 to 3.5 tons of CO₂ per year per m of strike length. If most of this
1087 CO₂ reacted with peridotite at the depth and temperature of MoD Mtn listvenite formation, this could
1088 supply the observed mass of CO₂ at MoD Mountain in less than 600,000 years.

1089

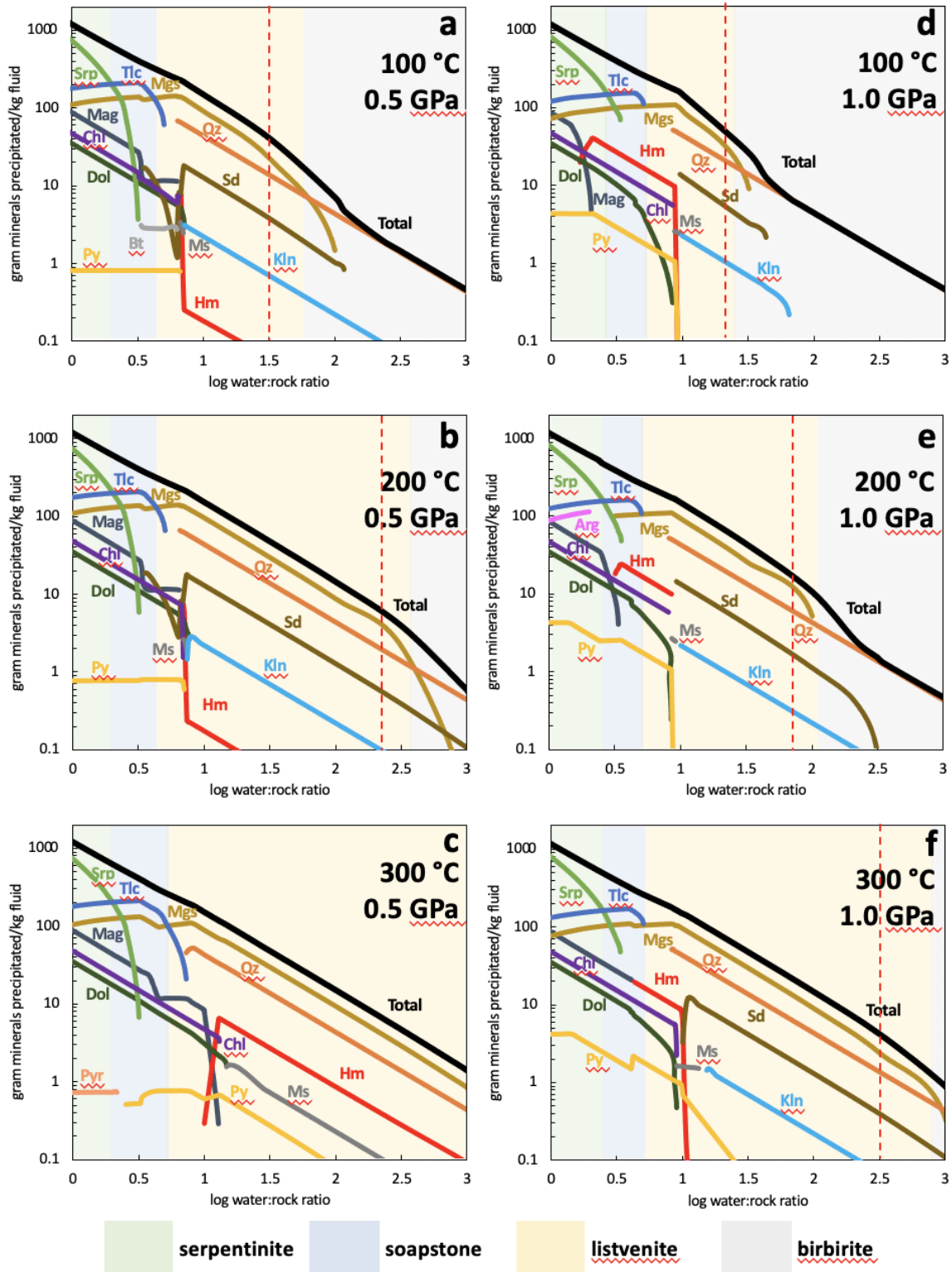
1090 Most of the model results at different conditions predict precipitation of a few weight percent
1091 magnesite (and some dolomite) in the serpentinization domain. This is consistent with observation of
1092 carbonate veins in serpentinites from Hole BT1B, and with the hypothesis that formation of carbonate
1093 veins in the serpentinite zone preceeded transformation of the serpentinite host rocks to listvenite
1094 (also see Figure 6 and associated text in Section 3.1,

1095

1096 The fluid temperatures, compositions and fluxes used in these calculations are different from the
1097 constraints used in some calculations by Falk & Kelemen (2015). In that previous work, we explored
1098 the possibility that CO₂ to form the listvenites was supplied over tens of millions of years, carried in
1099 100 to 200°C fluids containing a few hundred ppm dissolved carbon, derived from pore fluids and/or
1100 dewatering of opal and clay minerals, from the Hawasina sedimentary rocks immediately below the
1101 site of listvenite formation at MoD Mountain. However, one of us (Falk!) insisted on mentioning the
1102 possibility that the CO₂ to form listvenites was derived from fluids formed deeper in the subduction
1103 zone, that migrated updip. We now prefer this latter hypothesis, for the reasons outlined above.

1104

water/rock ratio vs grams minerals precipitated/kg fluid



1105
1106

1107 *Figure 15: Results of thermodynamic reaction path models of reaction between fluids derived from*
 1108 *devolatilization of Hawasina pelitic sedimentary rock sample OM20-17 (Section 4.3) and average*
 1109 *Oman harzburgite. Mineral end-member abbreviations Qz quartz, Sd siderite, Mgs magnesite, Kln*
 1110 *kaolinite, Ms muscovite, Dol dolomite, Chl chlorite, Py pyrite, Tlc talc, Srp serpentine (chrysotile), Pyr*
 1111 *pyrrhotite. Red, vertical dashed line indicates where magnesite/quartz molar and volume proportions*
 1112 *are ~ 2:1, as observed in magnesite listvenites from MoD Mtn (e.g., Figure 12).*

1113

1114 Updip migration of fluids in a subduction zone has been predicted in some simplified dynamic models
1115 of fluid flow in a viscously deforming subduction zone with high permeability (Wilson et al 2014).

1116 However, the tendency of fluid buoyancy to drive vertical fluid flow may often dominate subduction
1117 zone fluid fluxes. Thus, formation of relatively shallow listvenites, like those at MoD Mountain, may be
1118 localized and unusual. Elsewhere, CO₂-bearing fluids may migrate vertically into overlying mantle
1119 peridotite at greater depth (e.g., Kelemen & Manning 2015). It is interesting to ponder how subduction
1120 zone CO₂ fluxes may be partitioned between these different transport and mineralization processes.

1121

1122

4.5 Multiple reaction fronts

1123

1124 While detailed modeling of “chromatographic effects” during transformation of peridotite to
1125 serpentinite, and then to listvenite, is beyond the scope of this paper, the thermodynamic models
1126 presented in the previous Section (4.4) do provide a starting point for understanding these processes.

1127 As can be seen in **Figure 15**, simple, equilibrium reaction path models predict sharp fronts where
1128 serpentinite is replaced by soapstone, and then by listvenite. Talc-bearing, soapstone assemblages
1129 are predicted to crystallize in a limited range of conditions, consistent with the fact that talc is rare in
1130 core from Hole BT1B, and in hand specimens from MoD Mtn, where it is almost entirely restricted to
1131 narrow (~ 1 m scale) transition zones between listvenite and serpentinite. If we were to use different
1132 thermodynamic data, talc might be even less abundant, or absent in models at 100°C, because talc is
1133 predicted to be unstable below ~ 100°C with respect to antigorite + quartz when using mineral data
1134 from Holland and Powell or Gottschalk, together with the Redlich-Kwong equation of state for H₂O-
1135 CO₂ fluids as modified by Kerrick and Jacobs (1981) and by Holland and Powell (2003).

1136

1137

1138 In the model results presented in **Figure 15**, considering reaction progress from the point of view of
1139 the fluid, from high fluid/rock ratio on the right to low fluid/rock ratio on the left, magnesite + quartz
1140 and magnesite + talc become unstable with respect to serpentine as dissolved carbon in the fluid is
1141 exhausted. Because carbon is a minor constituent of aqueous fluid, but a major component of the
1142 solid listvenite assemblage, exhaustion of dissolved carbon is predicted to occur at a fluid/rock ratio
1143 much greater than 1 (log fluid/rock > 0). Of course, because aqueous fluid is composed mainly of
1144 H₂O, the potential for serpentinization of peridotite continues to much lower fluid/rock ratios.

1145

1146 Although we cannot model it, we can also predict that – in the presence of pervasive fluid flow on the
1147 grain scale – there could also be a sharp front where serpentine replaces olivine at water/rock ratios
1148 less than one. Thermodynamic calculations for simplified olivine serpentinization by Kelemen et al.
1149 (2020a) indicate that olivine + H₂O would be stable with respect to serpentine at 100°C and a partial
1150 pressure of ~ 10⁻² bars, and at 200°C and P(H₂O) ~ 1 bar. While these conditions cannot be modeled
1151 using EQ3/6, we can anticipate that very low partial pressures of H₂O – much lower than lithostatic
1152 pressures – are produced along grain boundaries and near the tips of incipient fractures and veins,

1153 especially where fluid has been almost completely consumed by peridotite hydration reactions. Under
1154 these conditions, there could be a sharp front where serpentine (at higher fluid pressures) becomes
1155 stable relative to olivine (at lower fluid pressure).

1156

1157 Throughout the mantle section of the Samail ophiolite, residual mantle peridotites commonly contain
1158 about 50 to 80% serpentine, as inferred from the fact that bulk rock analyses yield loss on ignition
1159 (mostly, H₂O) of 8 to 10 wt% as compared to 13 to 16 wt% H₂O in completely serpentinized, Mg end-
1160 member harzburgite and dunites. These partially serpentinized peridotites commonly show a “mesh
1161 texture”, with relict olivine and pyroxene “cores” transected by a “mesh” of cross-cutting serpentine
1162 veins – typically 10 to 100 microns apart (Francis 1956, Green 1961, Green 1964, Raleigh & Paterson
1163 1965). In some regions within the Samail ophiolite, particularly areas of relatively subdued topography
1164 that have undergone extensive, penetrative weathering, relict mantle minerals in the mesh cores are
1165 completely replaced by serpentine (e.g., OmanDP Sites BA1, BA2, BA3 and BA4, Kelemen et al
1166 2020c). However, along the steep canyons and narrow ridges that are typical of outcrops in the
1167 mantle section of the ophiolite, subject to relatively rapid erosion, the pervasive presence of the
1168 serpentine vein mesh surrounding relict mantle minerals attests to relatively rapid fluid transport in
1169 fractures and veins, compared to slow transport of H₂O into the mesh cores by diffusion and/or
1170 imbibition.

1171

1172 In contrast, as noted above, the serpentinites sampled in core from Hole BT1B contain no relict olivine
1173 or orthopyroxene, though pyroxene pseudomorphs (“bastites”) are evident. A zone of 100%
1174 serpentinized peridotites a few meters thick was sampled by Falk & Kelemen (2015) in a transect
1175 across a listvenite-peridotite contact on the watershed ridge east of the summit MoD Mountain.
1176 Outside this zone, samples of peridotite had compositions and textures typical of partially
1177 serpentinized residual mantle peridotites throughout the ophiolite. Based on these observations, we
1178 have inferred that there is a zone of 100% serpentinite front a few meters thick between listvenite and
1179 partially serpentinized peridotite, probably with a sharp front, less than 1 meter thick, separating
1180 partially from completely serpentinized peridotite. Indeed, the shipboard scientific party proposed that
1181 the serpentinization front formed at the same time as the listvenite front, further from the source of the
1182 CO₂-rich, reacting fluid, at lower water/rock ratios.

1183

1184 *4.6 Low temperature ductile deformation in subduction zones*

1185

1186 As noted above, the listvenites at MoD Mountain probably formed at depths of 25 to 40 km, at
1187 temperatures less 200°C, yielding low temperature “geotherms” of 5 to 8°C/km depth. Such small
1188 increases of temperature with depth are characteristic of the forearc above subduction zones
1189 (Peacock 1996). High fluid pressures at these depths may account for the somewhat surprising
1190 indications of low temperature, ductile deformation in core samples from Hole BT1B, based on the
1191 observed crystallographic preferred orientation (CPO) in quartz, magnesite and serpentine in core
1192 samples.

1193

1194 Some of the fabrics illustrated in Figure 10 could be inherited. For example, magnesite crystals in
1195 early formed, magnesite-hematite veins form parallel crystals, perpendicular to vein margins, with
1196 small misorientations between adjacent crystals. When these veins are parallel (because they form
1197 that way, or after they are transposed), this imparts a CPO to the sample, and may also give the
1198 impression that sub-grain boundaries are present, even if there was no deformation of magnesite
1199 crystals via dislocation creep. Similarly, quartz replacing opal may inherit a CPO, or a CPO may arise
1200 due to anisotropic stress during recrystallization, without substantial strain. However, clear examples
1201 of ductile deformation and shear zones with classical indicators of substantial strain do indicate that
1202 ductile deformation was active during and/or after the initial stages of listvenite formation, perhaps
1203 assisted by positive feedback between weakening, due to reaction-induced recrystallization, and
1204 porosity enhancement due to deformation, as discussed further by Menzel et al. (2021). An important
1205 role for ductile deformation in reaction zones at the top of subducting oceanic crust may help to
1206 explain why, in the relatively hot Cascadia and SW Japan subduction zones, there are very few
1207 earthquakes at the top of the subducting crust (Abers et al 2009, Abers et al 2013, Hirose et al 2008).

1208

1209

4.7 Volume change during listvenite formation

1210

1211 The likely volume change during fluid-rock reactions has long been debated. Whereas Coleman &
1212 Keith (1971) proposed that serpentinization involved simple addition of H₂O to peridotite, with no
1213 significant change in the volatile-free solid composition, Carmichael (1987), Nahon & Merino (1987),
1214 and Fletcher & Merino (2001) argued that such reactions take place at nearly constant volume, with
1215 addition of some components balanced by dissolution and export of others. Fletcher & Merino
1216 provided quantitative calculations to support this hypothesis. Where a fluid that is super-saturated in a
1217 new mineral phase, A, starts to crystallize A within a host mineral B, initially in equilibrium with fluid,
1218 expansion of B around A leads to an increase in local effective stress. In turn, because chemical
1219 potential is proportional to the mean stress, this reduces supersaturation in A and leads to
1220 undersaturation in B. This process continues, with very small volume changes, until the rate of
1221 crystallization of A becomes equal to the rate of dissolution of B, at a steady state stress.

1222

1223 Using the methodology of Fletcher and Merino (2001) and a saturation index of 2 (as they did),
1224 Kelemen and Hirth (2012) calculated that the steady state, effective stress during replacement of
1225 olivine with serpentine is ~ 40 MPa. However, because olivine is very far from equilibrium with water
1226 at low temperature, the saturation index for water reacting with olivine to form serpentine at 50 to
1227 250°C and $P(\text{H}_2\text{O}) > 1$ bar is close to 10^7 , and the steady state, effective stress estimated using the
1228 method of Fletcher and Merino is ~ 800 MPa (Kelemen & Hirth 2012). Clearly, such a large differential
1229 stress cannot be sustained within most rocks, which will deform at a lower stress, before the steady
1230 state can be reached, either via ductile mechanisms (if reactions are slow and temperatures are high)
1231 or via fracture and frictional deformation (if reactions are fast and temperatures are low). The latter
1232 outcome is sometimes termed “reaction-induced cracking” (Jamtveit et al 2009, Rudge et al 2010) or

1233 “reaction-driven cracking” (Kelemen & Hirth 2012). Thus, while some workers still disagree over the
1234 extent of volume change in specific replacement processes, the approach of Fletcher and Merino
1235 nicely explains a continuum between nearly constant volume replacement of one mineral by another
1236 at high temperature, close-to-equilibrium conditions, and large volume changes accommodated by
1237 fractures and frictional sliding at low temperature, far-from-equilibrium conditions.

1238

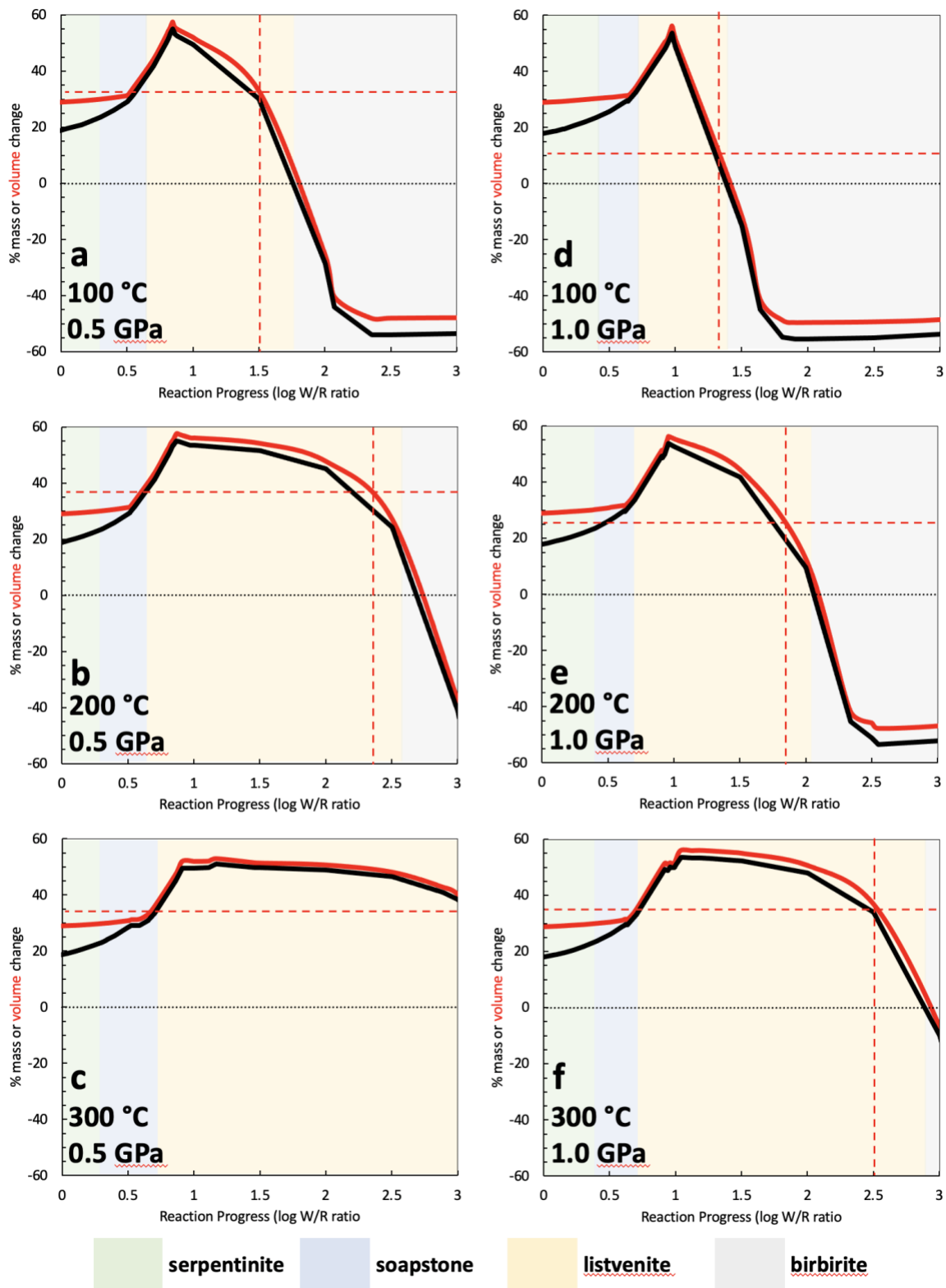
1239 As noted above, despite dramatic, local variability, the average composition of listvenites from MoD
1240 Mountain – in drill core and surface samples – is strikingly similar to the average composition of
1241 residual mantle harzburgites in the Samail ophiolite, with the exception that dolomite listvenites
1242 appear to record CaO addition and MgO extraction on an almost mole-for-mole ratio (Falk & Kelemen
1243 2015). However, dolomite listvenites are volumetrically minor in the core from Hole BT1B. Together,
1244 the concentrations of MgO, SiO₂ and FeO* (all Fe as FeO) account for more than 90% of the volatile-
1245 free bulk composition of listvenite samples. Thus, the fact that average Mg/Si/Fe ratios in the
1246 listvenites are almost identical to those in Samail peridotites suggests that either (a) large scale
1247 dissolution of the peridotite protoliths was nearly congruent, exporting dissolved, major elements in
1248 approximately their initial proportions, or (b) there was little dissolution and export of major elements
1249 in the protolith during addition of CO₂ to form listvenites, and addition of H₂O to form serpentinites.

1250

1251 Thermodynamic models, experimental data, and observations of natural rock samples strongly favor
1252 the second of these hypotheses. The solubility of silicate and Fe-oxide minerals in rock-buffered
1253 aqueous fluids at low temperature is too low to allow for large scale dissolution and export of major
1254 elements in open system, fluid-rock reactions. In turn, addition of CO₂ and/or H₂O to peridotites, with
1255 little removal of other species, leads to large increases in the mass and volume of the solid products
1256 of reaction. Birbirite formation may involve net volume and mass loss due to extensive dissolution of
1257 peridotite reactants at water/rock ratios greater than ~ 100. However, the models of listvenite
1258 formation illustrated in Figure 15 yield predicted mass and volume increases of 25 to 55 percent
1259 relative to an anhydrous, peridotite reactant during listvenite formation, as illustrated in **Figure 16**,
1260 except for results at 100°C and 1 GPa, with predicted volume increase from 10 to 55%. Similar results
1261 have been produced by thermodynamic models of serpentinization (volume increase of 40-60%, de
1262 Obeso & Kelemen 2018, Malvoisin 2015), experimental observation of closed system serpentinization
1263 (30-60%, Klein & Le Roux 2020) and analysis of microstructures in partially serpentinized peridotites
1264 formed in an open system (59±30 to 74±36%, Malvoisin et al 2020).

1265

percent mass and volume change during water/rock reaction

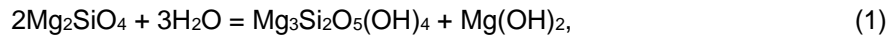


1266
1267
1268
1269
1270
1271
1272

Figure 16: Calculated mass and volume change relative to an anhydrous peridotite, for the reaction path models illustrated in Figure 15. Dashed, vertical red lines indicate where molar and volume proportions of magnesite/quartz reach 2:1, as observed in MoD Mtn listvenites (e.g., Figure 12). Dashed, horizontal line highlights the minimum increase in solid volume calculated for listvenite formation.

1273
1274
1275
1276
1277
1278
1279
1280
1281
1282
1283
1284
1285
1286
1287
1288
1289
1290

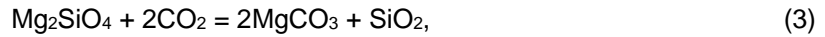
These modeled and observed volume changes approximate those resulting from simplified, Fe-free, stoichiometric reactions. Thus, hydration of olivine to form serpentine and brucite,



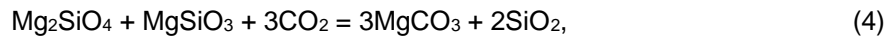
and hydration of olivine + orthopyroxene to form serpentine,



can produce 52 and 63% increases in the solid volume, respectively. (Volume change calculated as 100% (product volume - reactant volume)/(reactant volume)). Direct carbonation of olivine



and olivine + orthopyroxene,



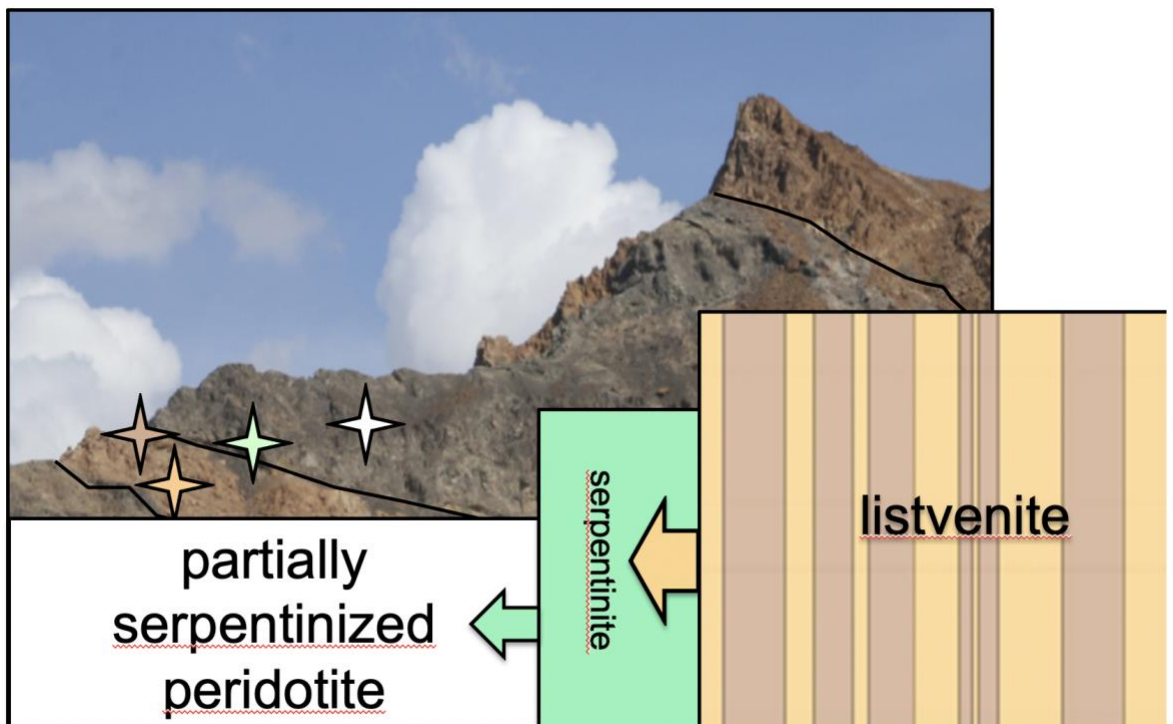
can lead to 85% and 74% increases in the solid volume, respectively. And, carbonation of serpentine plus brucite



and serpentine alone



both produce solid volume increases ~ 22%.



1291
1292
1293
1294
1295
1296
1297
1298
1299
1300

Figure 17: Schematic illustration of sequential volume changes during replacement of partially serpentinized peridotite by serpentinites and then replacement of serpentinites by listvenites. The height of the rectangles corresponds to the relative volumes, produced by reaction of CO₂-bearing fluid with an initial, anhydrous peridotite. The tan and brown stripes in the “listvenite” represent alternations of different listvenite compositional bands. Stars on photo of the SW side of MoD Mtn illustrate position of listvenite, serpentinite and partially serpentinized peridotite samples (Falk & Kelemen 2015).

1301 Because porosities in fractured peridotite, serpentinite and listvenite rarely if ever exceed 5%, all of
1302 these solid volume changes are accommodated mainly by expansion of the entire rock volume. It is
1303 interesting to speculate on how much uplift – and/or lateral expansion – in forearc regions above
1304 oceanic subduction zones is caused by hydration and carbonation of the mantle wedge. However, at
1305 the plate tectonic scale, the rates of reactions similar to those outlined in equations (1-6) are
1306 unknown. It is likely that the strains due to reaction are comparable to, or smaller than, other rates of
1307 deformation at convergent plate boundaries, rendering the effect of solid volume expansion difficult to
1308 detect at the regional scale.

1309
1310 Based on the considerations outlined in this section, it is likely that large increases in the solid volume
1311 occurred during formation of the MoD Mountain listvenites, and were accommodated mainly by
1312 reaction-driven cracking frictional sliding along fractures, and perhaps reaction-assisted dilatant
1313 granular flow (Menzel et al 2021). The presence of abundant, antitaxial magnesite, magnesite-
1314 hematite, and Fe-oxide veins in both serpentinites and listvenites can be taken as qualitatively
1315 consistent with such a hypothetical process. However, we have not identified any obvious strain
1316 markers that would allow a quantitative evaluation of this hypothesis using rock textures.

1317
1318 Building upon an idea from Hansen et al. (2005), the Shipboard Scientific Party developed the
1319 hypothesis that large volume increases due to hydration of olivine and pyroxene (reactions 1 & 2) may
1320 have initially formed fractures at (and beyond) a serpentinization front – not observed in drill core, but
1321 traversed in a sample transect by Falk & Kelemen (Falk & Kelemen 2015) – and these fractures were
1322 conduits for fluid flow and sites of localized deformation during the smaller volume changes due to
1323 carbonation of serpentinites (reactions 5 and 6) as schematically illustrated in Figure 17.

1324

1325

5. Conclusions

1326

1327 Observations of drill core of listvenite (completely carbonated peridotite), serpentinite, and
1328 subduction-related metamorphic rocks from OmanDP Hole BT1B provide constraints on temperature,
1329 depth, and deformation during mass transfer of H₂O and CO₂ from subducted sediments into
1330 overlying mantle peridotites at the leading edge of the mantle wedge. Listvenites, and a surrounding
1331 zone of serpentinite, formed at temperatures less than ~ 200°C and poorly constrained depths of 25
1332 to 40 km. Serpentinization and carbonation involved reaction of partially serpentinized, residual
1333 mantle peridotite with CO₂-rich, aqueous fluids produced by devolatilization of subducting, clastic
1334 sediments analogous to the Hawasina formation, probably at 400 to 500°C and greater depth. These
1335 fluids were transported up the subduction zone to the site of listvenite formation. Such processes
1336 could form important reservoirs with a significant role in the global carbon cycle, as previously
1337 proposed by Kelemen and Manning (2015).

1338

1339 Based on observed crystallographic preferred orientation in quartz, magnesite and serpentine in
1340 macroscopically identified shear zones, it is inferred that ductile deformation of listvenite and

1341 serpentinite occurred under low temperature conditions at the base of the mantle wedge during
1342 subduction. Low temperature ductile deformation, coeval with serpentinization and listvenite
1343 formation, may have been facilitated by recrystallization associated with the hydration and carbon
1344 mineralization processes, as discussed in more detail by Menzel et al. (Menzel et al 2021). Such a
1345 process could be active in subduction zones where the interface between subducting oceanic crust,
1346 sediments, and hanging wall peridotites is aseismic.

1347

1348 The total solid volume increased by tens of percent during hydration followed by carbonation. While
1349 core and surface samples provide few direct constraints on the mechanism that accommodated this
1350 expansion, one hypothesis is that large volume changes during hydration of olivine and pyroxene
1351 along a serpentinization front caused large stresses and fractures that accommodated expansion via
1352 frictional sliding, and provided secondary porosity for the CO₂-rich fluids that transformed
1353 serpentinites to listvenites.

1354

1355

6. Author contributions

1356

1357 Kelemen and de Obeso conducted field mapping at MoD Mountain. de Obeso made new Sr and C
1358 isotopic analyses of listvenites, the metamorphic sole and the underlying sedimentary rocks, updating
1359 work by Falk & Kelemen (2015). Stockli carried out the reconnaissance (U,Th)/He analyses of zircons
1360 from the metamorphic sole and lower crust, using zircon separates samples provided by Rioux.
1361 Godard expertly led the BT1B geochemistry team onboard Drilling Vessel Chikyu, and then heroically
1362 continued with analyses at the Université de Montpellier on behalf of the Shipboard Scientific Party.
1363 Okazaki labored with Kelemen on the triangular histogram of shipboard XRF scanner data. Leong and
1364 de Obeso conducted the EQ3/6 thermodynamic modeling, in consultation with Kelemen. Working with
1365 his computer in 46°C weather on the drill site, Manning provided key insights into conditions for
1366 coexisting hematite and organic carbon compounds. Ellison supervised Kelemen's Raman
1367 spectroscopy analyses at the University of Colorado, Boulder, and offered essential advice and data
1368 interpretation. Kotowski led analysis of core from the metamorphic sole and shared her results. Urai
1369 led the structural geology team during core description onboard DV Chikyu, and is now advising
1370 Menzel, who is leading analysis and interpretation of microstructures. Hirth offered insights into
1371 potential mechanisms of low temperature, ductile deformation in subduction zones. Lafay and Beinlich
1372 provided valuable input on the drill site and as members of the Shipboard Scientific Party. Coggon
1373 (Project Manager) supervised drilling, core curation and logistics for this and all other OmanDP
1374 boreholes, together with Nehal Warsi (Site Geologist). Matter (Project Director), Teagle (ICDP Lead
1375 Investigator) and Sulaimani (Country Manager) worked tirelessly to ensure the success of the Oman
1376 Drilling Project. Harris, Kelemen, Michibayashi, and Takazawa served as Co-Chief Scientists onboard
1377 DV Chikyu during description of core from Hole BT1B. Kelemen (Chief Scientist) helped lead the
1378 project, had a few ideas, and took the lead in writing this manuscript.

1379

1380

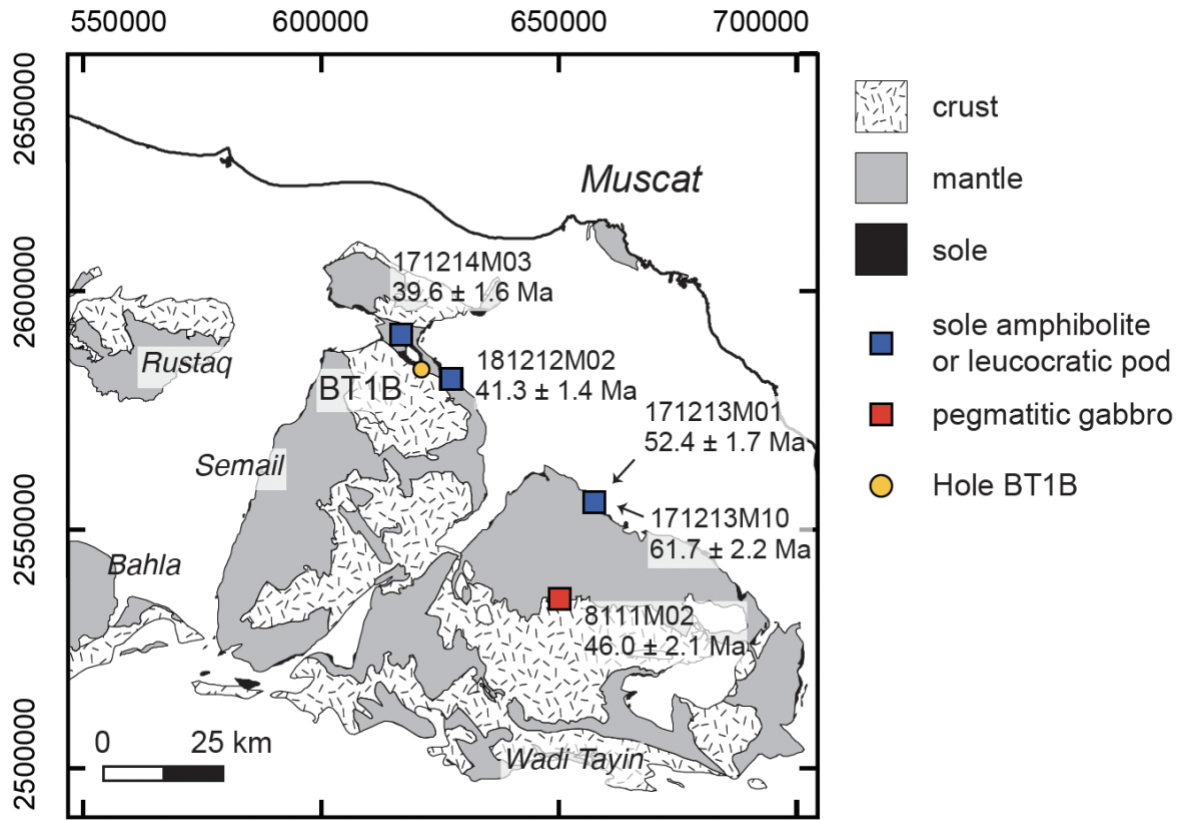
7. Acknowledgements

1381
1382 Drilling and research in the Oman Drilling Project were supported by the Alfred P. Sloan Foundation
1383 (in association with the Deep Carbon Observatory, DCO), the International Continental scientific
1384 Drilling Program (ICDP), US National Science Foundation (NSF) Research Grant NSF-EAR-1516300,
1385 the Japanese Marine Science and Technology Center (JAMSTEC), grant number 16H06347 from the
1386 Japanese Society for the Promotion of Science (JSPS), the US National Aeronautics and Space
1387 Administration (NASA, including the Rock Powered Life NASA Astrobiology Institute (NNA15BB02A),
1388 the European Science Foundation, the German Science Foundation, the Swiss Science Foundation,
1389 and the International Ocean Discovery Program (aka International Ocean Drilling Program, IODP).
1390 Kelemen's research was also supported with funds from the Arthur D. Storke Chair at Columbia
1391 University. In addition to the authors of this paper, a huge team contributed to the success of
1392 OmanDP, including drilling and core analyses at Hole BT1B. In Oman, a Project Supervisory
1393 Committee chaired by Dr. Said Al Habsi (Director General of Water Resources Assessment in the
1394 Ministry of Regional Municipalities and Water Resources), and including Prof. Sobhi Nasir at Sultan
1395 Qaboos University, Dr. Ali Al Rajhi, Director of the Geological Survey of Oman, and others, ensured
1396 that the project went forward smoothly in accordance with Omani requirements. At Petroleum
1397 Development Oman (PDO), Dr. Hamad Shuaili and Dr. Hisham Siyabi kindly facilitated storage of the
1398 archive half of all OmanDP core. We particularly thank Dr. Jay Miller and Dr. Brad Clement at IODP
1399 TAMU for making the online proceedings volume possible, and Shana Lewis, Rhonda Kappler, Jean
1400 Wulfson, Phil Rumford, Lorri Peters, Crystal Wolfe and Kenneth Sherar at IODP TAMU for editorial
1401 assistance in preparing the Proceedings of the Oman Drilling Project, more or less following IODP
1402 protocols in presenting the results of this decidedly non-standard ICDP project. We thank the
1403 technical staff onboard Drilling Vessel Chikyu for fantastic, efficient support and advice over four
1404 months in summers 2017 and 2018, especially Lena Maeda, Dr. Yusuke Kubo, and Dr. Chiaki
1405 Igarashi. Dr. Nobu Eguchi served as a patient, generous liaison between OmanDP, NSF and
1406 JAMSTEC. Core description onboard Chikyu would have been impossible without proactive support
1407 from JAMSTEC President Asahiko Taira and NSF Program Director Leonard Johnson. Similarly, we
1408 received essential assistance with borehole permitting from Professor Ali Al Bemani, Vice Chancellor
1409 of Sultan Qaboos University. On a different timescale, we are deeply indebted to His Majesty Sultan
1410 Qaboos bin Said Al Said for his open-door policy for scientific research in Oman, and to Professors
1411 Françoise Boudier, Bob Coleman, Cliff Hopson and Adolphe Nicolas for establishing the framework
1412 for modern studies of the Samail ophiolite.

1413
1414 **Data Availability:** Samples in Table 1 have IGSN numbers and locations, and data in Table 1 are in
1415 the process of being archived in the Geochron database (www.geochron.org). Figures 4, and 6 are
1416 compilations of images that are published at <http://publications.iodp.org/other/Oman/OmanDP.html>,
1417 where they are freely available, with more detailed references provided in the figure captions. Figures
1418 1, 2, 5, and 7-17, Supplementary Figures 1 and 2, and Supplementary Tables 1 and 2 constitute data
1419 that are original with this paper. Although this is not required by JGR, when this manuscript is
1420 submitted, the submitted version will be archived and freely available at ESSOAr.

1421
1422
1423
1424
1425

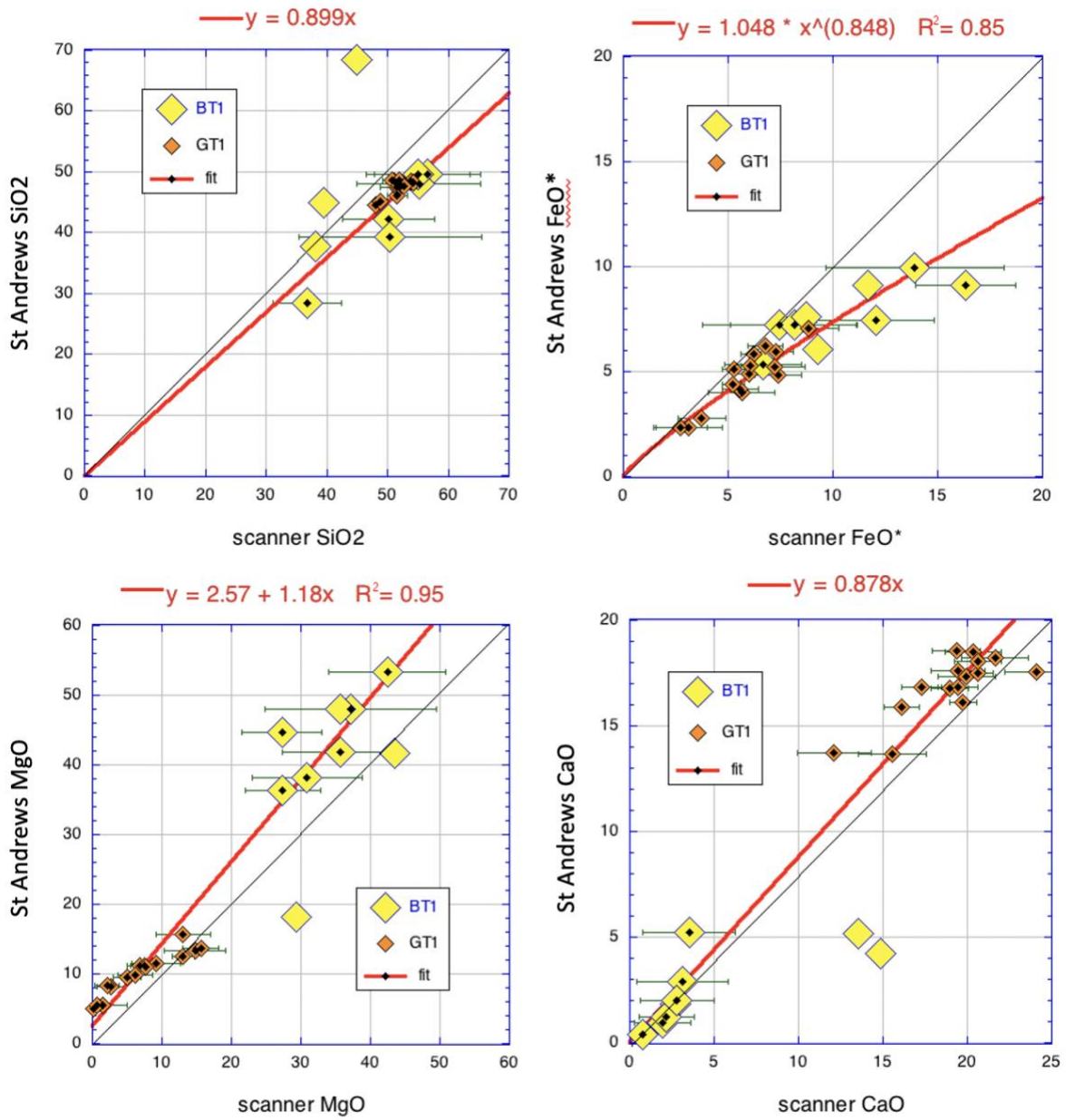
Supplementary Figure 1: Map in UTM coordinates of Oman Drilling Project Hole BT1B and the (U,Th)/He cooling ages reported in the main text and Supplemental Table 1. Geologic map is after Nicolas et al. (2000).



1426
1427

1428
1429
1430
1431
1432

Supplementary Figure 2: University of St. Andrews XRF data on core samples from Oman Drilling Project Holes BT1B and GT1A used to calibrate XRF scanner data from DV Chikyu. All data tabulated in Kelemen et al. (2020b).



1433
1434
1435

Supplementary Table 1: Reduced (U-Th/Sm)/He Data

Sample	UTM (E) ^a	UTM (N) ^a	IGSN ^b	Location	Rock type	Mineral	Age: Ma	$\pm 2\sigma$ abs ^c	U (ppm)	Th (ppm)	⁸⁷ Sm (ppm)	[U]	Th/U	He (mmol/g)	mass (ng)	Ft ^d	ESR ^e	Comments	Mean age: Ma	stdev: Ma
z171213-M01-1	657956	2555558	MER171301	Wadi Tayin Massif Metamorphic sole	leucocratic pod in amphibolite	zircon	55.8	4.5	30.2	1.6	0.0	30.5	0.05	7.6	13.04	0.83	67.8		54.5	7.4
z171213-M01-2						zircon	52.2	4.2	40.2	2.0	0.0	40.7	0.05	10.06	0.80	59.0		n =	6 of 6	
z171213-M01-3						zircon	62.2	5.0	40.2	2.6	5.1	40.9	0.06	10.5	5.34	0.77	48.7			
z171213-M01-4						zircon	56.0	4.5	48.8	2.5	0.0	49.4	0.05	12.1	9.53	0.81	61.0			
z171213-M01-5						zircon	41.1	3.3	23.1	1.4	1.0	23.5	0.06	4.5	27.91	0.86	85.6			
z171213-M01-6						zircon	59.6	4.8	33.1	2.5	0.0	33.7	0.07	9.0	15.62	0.83	67.6			
z171213-M10-1	657290	2555449	MER171310	Wadi Tayin Massif Metamorphic sole	leucocratic pod in amphibolite	zircon	64.9	5.2	194.3	12.9	0.0	197.3	0.07	52.6	4.24	0.76	47.1		61.8	2.6
z171213-M10-3						zircon	64.2	5.1	165.5	11.1	0.0	166.0	0.07	41.6	2.82	0.72	40.3		n =	5 of 5
z171213-M10-4						zircon	59.4	4.7	130.4	8.0	0.0	132.3	0.06	33.4	5.90	0.79	53.7			
z171213-M10-5						zircon	60.0	4.8	358.8	33.4	0.0	366.5	0.09	93.5	6.09	0.79	53.6			
z171213-M10-6						zircon	60.7	4.9	153.6	10.2	0.0	156.0	0.07	40.6	6.44	0.79	55.2			
z171214-M03-1*	617297	2591659	MER171403	Fanjah Metamorphic sole	amphibolite + leucocratic layers	zircon	23.9	1.9	12.6	2.7	14.5	13.3	0.21	1.2	1.88	0.69	36.3	likely apatite	38.7	7.7
z171214-M03-2						zircon	29.0	2.3	97.6	0.7	11.9	97.9	0.01	10.9	2.30	0.71	38.3		n =	5 of 6
z171214-M03-3						zircon	39.6	3.2	114.9	3.1	17.3	115.7	0.03	16.1	1.58	0.65	30.9			
z171214-M03-4						zircon	33.0	2.6	71.1	1.3	0.0	71.4	0.02	10.6	13.35	0.83	68.9			
z171214-M03-5						zircon	44.9	3.6	569.4	7.4	0.0	571.1	0.01	108.0	5.25	0.78	51.4			
z171214-M03-6						zircon	47.2	3.8	358.2	5.5	0.0	359.5	0.02	68.1	3.30	0.74	43.8			
z181212-M02-1	626900	2582008	MER181202	Fanjah Metamorphic sole	amphibolite in metamorphic sole	zircon	39.1	3.1	5.0	0.2	1.2	5.0	0.03	0.9	22.61	0.86	82.3		44.4	8.0
z181212-M02-2						zircon	49.2	3.9	7.0	2.1	3.0	7.5	0.30	1.6	9.25	0.80	58.9		n =	6 of 6
z181212-M02-3						zircon	30.6	2.4	2.7	0.9	3.3	3.0	0.33	0.4	8.29	0.80	58.4			
z181212-M02-4						zircon	46.8	3.7	14.5	5.2	3.9	15.7	0.36	3.1	7.09	0.78	54.4			
z181212-M02-5						zircon	51.9	4.1	6.7	1.4	2.2	7.0	0.20	1.6	12.22	0.82	66.7			
z181212-M02-6						zircon	49.0	3.9	7.6	1.4	0.0	8.0	0.19	1.9	46.24	0.89	106.7			
z8111-M02-1*	650157	2535313	MER081102	Wadi Tayin Massif Ophiolite lower crust	hornblende gabbro pegmatite vein	zircon	263.1	21.0	60.0	99.8	0.0	83.0	1.66	95.2	7.42	0.79	58.4	partial grain loss	46.4	3.9
z8111-M02-2						zircon	42.2	3.4	15.9	3.0	10.9	16.7	0.19	2.7	2.50	0.72	39.6		n =	3 of 5
z8111-M02-3*						zircon	136.3	10.9	38.1	43.4	0.0	48.1	1.14	27.3	4.69	0.76	50.1	partial grain loss		
z8111-M02-4						zircon	47.3	3.8	28.0	1.8	0.0	28.5	0.06	4.7	1.23	0.65	30.9			
z8111-M02-5						zircon	49.8	4.0	20.5	2.4	7.1	21.1	0.11	4.3	3.83	0.75	45.8			

^a WGS 84 UTM zone 40

^b Assigned international geo sample number (IGSN)

^c 2-sigma standard error based on FCT analysis

^d Ft = alpha ejection correction of Farley et al 1996

^e ESR = Equivalent Spherical Radius

Supplementary Table 2

Rock compositions used in the model (wt %)

	OM20-17	Average Hz ^a
SiO ₂	74.43	40.14
TiO ₂	0.54	0.01
Al ₂ O ₃	12.17	0.79
Cr ₂ O ₃	nm	0.37
FeO _T	3.88 ^c	7.46 ^d
MnO	0.06	0.12
MgO	2.17	40.83
CaO	0.1 ^b	0.97
Na ₂ O	0.51	0.09
K ₂ O	2.77	0.00
P ₂ O ₅	nm	0.01
S	0.01	0.00
H ₂ O	3.77	8.61
CO ₂	0.22	0.00
Total	96.42	99.41

bdl - below detection limit; nm - not measured

^aAverage composition of harzburgites, see text for references

^bAssumed to be 0.1 wt % in the model

^c as Fe₂O₃

^d as FeO

^e assumed for modeling

^f measured as 0.06 wt% C

1436
1437
1438
1439
1440
1441
1442
1443
1444
1445
1446
1447
1448
1449
1450
1451
1452
1453
1454
1455
1456
1457
1458
1459
1460
1461
1462
1463
1464
1465
1466
1467
1468
1469
1470
1471
1472
1473
1474
1475
1476
1477
1478
1479
1480
1481
1482
1483
1484
1485
1486
1487
1488
1489
1490
1491
1492
1493
1494

8. References cited

- Abers GA, MacKenzie LS, Rondenay S, Zhang Z, Wech AG, Creager KC. 2009. Imaging the source region of Cascadia tremor and intermediate-depth earthquakes. *Geology* 37: 1119-22
- Abers GA, Nakajima J, van Keken PE, Kita S, Hacker BR. 2013. Thermal–petrological controls on the location of earthquakes within subducting plates. *Earth Planet Sci. Lett.* 369-370: 178-87
- Abu-Jaber NS, Kimberley MM. 1992. Origin of ultramafic-hosted vein magnesite deposits. *Ore Geol. Reviews* 7: 155-91
- Aftabi A, Zarrinkoub MH. 2013. Petrogeochemistry of listvenite association in metaophiolites of Sahlabad region, eastern Iran: Implications for possible epigenetic Cu–Au ore exploration in metaophiolites. *Lithos* 156: 186-203
- Agard P, Yamato P, Soret M, Prigent C, Guillot S, Plunder A, Dubacq B, Chauvet A, Monié P. 2016. Plate interface rheological switches during subduction infancy: Control on slab penetration and metamorphic sole formation. *Earth Planet Sci. Lett.* 451: 208-20
- Akbulut M, Piskin O, Karayigit AI. 2006. The genesis of the carbonatized and silicified ultramafics known as listvenites: A case study from the Mihaliccik region (Eskisehir), NW Turkey. *Geol. J.* 41: 557-80
- Alabaster T, Pearce JA, Malpas J. 1982. The volcanic stratigraphy and petrogenesis of the Oman ophiolite complex. *Contrib. Mineral. Petrol.* 81: 168-83
- Allegre CJ, Montigny R, Bottinga Y. 1973. Cortège ophiolitique et cortège océanique, géochimie comparée et mode de genèse. *Bulletin de la Société Géologique de France* 7
- Amri I, Ceuleneer G, Benoit M, Python M, Puga E, Targuisti K. 2007. Genesis of granitoids by interaction between mantle peridotites and hydrothermal fluids in oceanic spreading setting in the Oman ophiolite. *GEOGACETA* 42: 23-6
- Andreani M, Baronnet A, Boullier A-M, Gratier J-P. 2004. A microstructural study of a “crack-seal” type serpentine vein using SEM and TEM techniques. *Eur. J. Mineral.* 16: 585-95
- Arisi Rota F, Brondi A, Dessau G, Branzini M, Stea B, Vighi L. 1971. I giacimenti minerari. In “La Toscana Meridionale. Fondamenti geologico-minerari per una prospettiva di valorizzazione delle risorse naturali”. *Rendiconti S.I.M.P.* 27: 357-544
- Asimow PD, Dixon JE, Langmuir CH. 2004. A hydrous melting and fractionation model for mid-ocean ridge basalts: Application to the Mid-Atlantic Ridge near the Azores. *G-cubed* 5
- Barnes I, O'Neill JR, Rapp JB, White DE. 1973. Silica-carbonate alteration of serpentine: Wall rock alteration in mercury deposits of the California Coast Ranges. *Econ. Geol.* 68: 388-98
- Béchenec F, Le Métour J, Rabu D, Bourdillon-de-Grissac C, De Wever P, Beurrier M, Villey M. 1990. The Hawasina Nappes: stratigraphy, palaeogeography and structural evolution of a fragment of the south-Tethyan passive continental margin. *Geol. Soc. Special Pub.* 49: 213-23
- Béchenec F, Le Métour J, Rabu D, Villey M, Beurrier M. 1988. The Hawasina Basin: A fragment of a starved passive continental margin, thrust over the Arabian Platform during obduction of the Sumail Nappe. *Tectonophysics.* 151: 323-43
- Beinlich A, Austrheim H, Glodny J, Erambert M, Andersen TB. 2010. CO₂ sequestration and extreme Mg depletion in serpentinized peridotite clasts from the Devonian Solund basin, SW-Norway. *Geochim. Cosmochim. Acta* 74: 6935-64
- Beinlich A, Plümper O, Boter E, Müller IA, Kourim F, Ziegler M, Harigane Y, Lafay R, Kelemen PB, Oman Drilling Project Science Team. 2020. Ultramafic rock carbonation: Constraints from listvenite core BT1B, Oman Drilling Project. *J. Geophys. Res.* 125: e2019JB019060
- Benoit M, Ceuleneer G, Polvé M. 1999. The remelting of hydrothermally altered peridotite at mid-ocean ridges by intruding mantle diapirs. *Nature* 402: 514-8
- Berman RG. 1988. Internally-consistent thermodynamic data for minerals in the system Na₂O-K₂O-CaO-MgO-FeO-Fe₂O₃-Al₂O₃-SiO₂-TiO₂-H₂O-CO₂. *J. Petrol.* 29: 445-522
- Borojević Šoštarić S, Palinkaš AL, Neubauer F, Cvetković V, Bernroider M, Genser J. 2014. The origin and age of the metamorphic sole from the Rogozna Mts., Western Vardar Belt: New evidence for the one-ocean model for the Balkan ophiolites. *Lithos* 192: 39-55
- Boschi C, Dini A, Dallai L, Ruggieri G, Gianelli G. 2009. Enhanced CO₂-mineral sequestration by cyclic hydraulic fracturing and Si-rich fluid infiltration into serpentinites at Malenrata (Tuscany, Italy). *Chem. Geol.* 265: 209-26
- Bottinga Y, Allegre CJ. 1973. Thermal aspects of sea-floor spreading and the nature of the oceanic crust. *Tectonophysics.* 18: 1-17
- Boudier F, Ceuleneer G, Nicolas A. 1988. Shear zones, thrusts and related magmatism in the Oman ophiolite: Initiation of thrusting on an oceanic ridge. *Tectonophysics.* 151: 275-96

1495 Boudier F, Coleman RG. 1981. Cross section through the peridotite in the Semail ophiolite. *J.*
1496 *Geophys. Res.* 86: 2573-92

1497 Braun MG, Kelemen PB. 2002. Dunite distribution in the Oman ophiolite: Implications for melt flux
1498 through porous dunite conduits. *G-cubed* 3

1499 Breton J-P, Béchenec F, Le Métour J, Moen-Maurel L, Razin P. 2004. Eoalpine (Cretaceous)
1500 evolution of the Oman Tethyan continental margin: insights from a structural field study in Jabal
1501 Akhdar (Oman Mountains). *GeoArabia* 9: 41-58

1502 Briquieu L, Mével C, Boudier F. 1991. Sr, Nd and Pb isotopic constraints on the genesis of a calc-
1503 alkaline plutonic suite in the Oman mountains related to the obduction process. In *Ophiolite genesis*
1504 *and evolution of the oceanic lithosphere*, ed. T Peters, A Nicolas, RG Coleman, pp. 517-42. Muscat,
1505 Oman: Ministry of Petroleum and Minerals, Sultanate of Oman

1506 Carmichael DM. 1987. Induced stress and secondary mass transfer: Thermodynamic basis for the
1507 tendency toward constant-volume constraint in diffusion metasomatism. In *Chemical Transport in*
1508 *Metasomatic Processes, NATO ASI Series C, 218.*, ed. HC Helgeson, pp. 239-64. Dordrecht:
1509 Springer

1510 Chemenda AI, Burg J-P, Mattauer M. 2000. Evolutionary model of the Himalaya-Tibet system:
1511 Geopoem based on new modelling, geological and geophysical data. *Earth Planet Sci. Lett.* 174:
1512 397-409

1513 Christensen NL, Smewing JD. 1981. Geology and seismic structure of the southern section of the
1514 Oman Ophiolite. *J. Geophys. Res.*: 2545-55

1515 Coleman RG, Hopson CA, eds. 1981. *Oman Ophiolite Special Issue, J. Geophys. Res.*, Vols. 86.
1516 2495-782 pp.

1517 Coleman RG, Keith TE. 1971. Chemical Study of Serpentinization - Burro Mountain, California.
1518 *Journal of Petrology* 12: 311-&

1519 Connolly JAD. 1990. Multivariable phase-diagrams - an algorithm based on generalized
1520 thermodynamics. *Am. J. Sci.* 290: 666-718

1521 Connolly JAD. 2005. Computation of phase equilibria by linear programming: A tool for geodynamic
1522 modeling and its application to subduction zone decarbonation. *Earth Planet Sci. Lett.* 236: 524-41

1523 Connolly JAD. 2009. The geodynamic equation of state: what and how. *G-cubed* 10: Q10014
1524 DOI:10.1029/2009GC002540

1525 Cooper DJW. 1988. Structure and sequence of thrusting in deep-water sediments during ophiolite
1526 emplacement in the south-central Oman Mountains. *J. Struct. Geol.* 10: 473-85

1527 Cowan RJ, Searle MP, Waters DJ. 2014. Structure of the metamorphic sole to the Oman Ophiolite,
1528 Sumeini Window and Wadi Tayyin: implications for ophiolite obduction processes. *Geol. Soc.*
1529 *London Spec. Pub.* 392: 155-75

1530 Cox J, Searle M, Pedersen R. 1999. The petrogenesis of leucogranitic dykes intruding the northern
1531 Semail ophiolite, United Arab Emirates: field relationships, geochemistry and Sr/Nd isotope
1532 systematics. *Contrib. Mineral. Petrol* 137: 267-87

1533 de Obeso JC, Kelemen PB. 2018. Fluid rock interactions in residual mantle peridotites overlain by
1534 shallow oceanic limestones: Insights from Wadi Fins, Sultanate of Oman. *Chem. Geol.* 498: 139-49

1535 de Obeso JC, Kelemen PB, Leong JM, Manning CE, Menzel MD, Cai YM, Godard M, Oman Drilling
1536 Project Phase 1 Science Party. 2021a. Sr isotope record from OmanDP Hole BT1B. *J. Geophys.*
1537 *Res.*: **A PDF of the current draft of this manuscript is included with this submission.**

1538 de Obeso JC, Kelemen PB, Manning CE, Michibayashi K, Harris M, Party ODPPS. 2017. Listvenite
1539 formation from peridotite: Insights from Oman Drilling Project hole BT1B and preliminary reaction
1540 path model approach. *AGU Fall Meeting Abstracts*: 328802

1541 de Obeso JC, Santiago Ramos D, Higgins J, Kelemen P. 2021b. A Mg isotopic perspective on the
1542 mobility of magnesium during serpentinization and carbonation of the Oman ophiolite. *J. Geophys.*
1543 *Res.* 126: e2020JB020237

1544 Deines P. 2002. The carbon isotope geochemistry of mantle xenoliths. *Earth-Science Rev.* 58: 247-
1545 78

1546 Duncan RA. 1982. A captured island chain in the Coast Range of Oregon and Washington. *J.*
1547 *Geophys. Res.* 87: 10,827-10,37

1548 Durney DW, Ramsay JG. 1973. Incremental strain measured by syntectonic crystallization growths. In
1549 *Gravity and Tectonics*, ed. KA De Jong, R Scholten, pp. 67-96. New York: John Wiley

1550 Ece ÖI, Matsubaya O, Çoban F. 2005. Genesis of hydrothermal stockwork-type magnesite deposits
1551 associated with ophiolite complexes in the Kütahya-Eskişehir region, Turkey. *Neues Jahrbuch für*
1552 *Minerologie-Abhandlungen* 181: 191-205

1553 Ernewein M, Pflumio C, Whitechurch H. 1988. The death of an accretion zone as evidenced by the
1554 magmatic history of the Semail ophiolite (Oman). *Tectonophys.* 151: 247-74

1555 Escayola MP, Proenza JA, van Staal C, Rogers N, Skulski T. 2009. The Point Rouse listvenites,
1556 Baie Verte, Newfoundland: Altered ultramafic rocks with potential for gold mineralization? *Current*
1557 *Research, Newfoundland & Labrador Dept. of Natural Res.* 09-1: 1-12

1558 Facq S, Daniel I, Montagnac G, Cardon H, Sverjensky DA. 2016. Carbon speciation in saline
1559 solutions in equilibrium with aragonite at high pressure. *Chem. Geol.* 431, 44–53. *Chem. Geol.* 431:
1560 44-63

1561 Falk ES. 2014. *Carbonation of Peridotite in The Oman Ophiolite*. Columbia University, New York, NY,
1562 USA. 233 pp.

1563 Falk ES, Kelemen PB. 2015. Geochemistry and petrology of listvenite in the Oman Ophiolite:
1564 Complete carbonation of peridotite during ophiolite emplacement. *Geochim. Cosmochim. Acta* 160:
1565 70-90

1566 Fletcher RC, Merino E. 2001. Mineral growth in rocks: kinetic-rheological models of replacement, vein
1567 formation, and syntectonic crystallization. *Geochim. Cosmochim. Acta* 65: 3733-48

1568 Foley SF, Fischer TP. 2017. An essential role for continental rifts and lithosphere in the deep carbon
1569 cycle. *Nature Geosci.* 10: 897-902

1570 Francis GH. 1956. The serpentinite mass in Glen Urquhart, Inverness-shire, Scotland. *Am. J. Sci.*
1571 254: 201-26

1572 Garber JM, Rioux M, Kylander-Clark AR, Hacker BR, Vervoort JD, Searle MP. 2020. Petrochronology
1573 of Wadi Tayin metamorphic sole metasediment, with implications for the thermal and tectonic
1574 evolution of the Samail Ophiolite (Oman/UAE). *Tectonics* 39: e2020TC006135

1575 Garcia del Real P, Maher K, Kluge T, Bird DK, Brown GE, John CM. 2016. Clumped-isotope
1576 thermometry of magnesium carbonates in ultramafic rocks. *Geochim. Cosmochim. Acta* 193: 222-
1577 50

1578 Gerbert-Gaillard L. 2002. *Caractérisation Géochimique des Péridotites de l'ophiolite d'Oman :*
1579 *processus magmatiques aux limites lithosphère/asthenosphère*. Université Montpellier II - Sciences
1580 et Techniques du Languedoc, Montpellier, FR. 241 pp.

1581 Ghent ED, Stout MZ. 1981. Metamorphism at the base of the Samail ophiolite, southeastern Oman
1582 mountains. *J. Geophys. Res.* 86: 2557-71

1583 Glennie KW, Boeuf MGA, Hughes-Clark MW, Moody-Stuart M, Pilaar WFH, Reinhardt BM. 1974a.
1584 Geology of the Oman Mountains. *Verh. K. Ned. Geol. Mijnbouw. Gen.* 31

1585 Glennie KW, Boeuf MGA, Hughes-Clarke MW, Moody-Stuart M, Pilaar WFH, Reinhardt BM. 1973.
1586 Late Cretaceous nappes in the Oman Mountains and their geologic evolution. *Am. Assoc.*
1587 *Petroleum Geol. Bull.* 57: 5-27

1588 Glennie KW, Boeuf MGA, Hughes-Clarke MW, Moody-Stuart M, Pilaar WFH, Reinhardt BM. 1974b.
1589 Geology of the Oman Mountains. *Kon. Nederlands Geol. Mijb. Gen. Ver. Verh.* 31: 1-423

1590 Godard, M., E. Bennett, E. Carter, F. Kourim, R. Lafay, J. Noël, P.B. Kelemen, K. Michibayashi, M.
1591 Harris, and Oman Drilling Project Phase 1 Science Party, *Geochemical and Mineralogical Profiles*
1592 *Across the Listvenite- Metamorphic Transition in the Basal Megathrust of the Oman Ophiolite: First*
1593 *Results from Drilling at Oman Drilling Project Hole BT1B, AGU Fall Meeting abstract 328591, 2017;*
1594 *this citation is a stand-in for Godard M, Carter E, Lafay R, Bennett E, Kourim F, de Obeso J-C,*
1595 *Michibayashi K, Harris M, Kelemen P, Oman Drilling Project Phase 1 Science Party. 2021.*
1596 *Geochemical and Mineralogical Profiles Across the Listvenite-Metamorphic Transition in the Basal*
1597 *Megathrust of the Semail Ophiolite: Results from Drilling at Oman DP Hole BT1B. J. Geophys.*
1598 *Res., which is not yet available*

1599 Godard M, Jousset D, Bodinier J-L. 2000. Relationships between geochemistry and structure
1600 beneath a palaeo-spreading centre: A study of the mantle section in the Oman ophiolite. *Earth*
1601 *Planet. Sci. Lett.* 180: 133-48

1602 Gottschalk M. 1997. Internally consistent thermodynamic data for rock-forming minerals in the system
1603 SiO₂-TiO₂-Al₂O₃-Fe₂O₃-CaO-MgO-FeO-K₂O-Na₂O-H₂O-CO₂. *Eur. J. Mineral.* 9: 175-223

1604 Green DH. 1961. Ultramafic breccias from the Musa Valley, eastern Papua. *Geol. Mag.* 98: 1-26

1605 Green DH. 1964. The petrogenesis of the high-temperature peridotite intrusion in the Lizard area,
1606 Cornwall. *J. Petrol.* 5: 134-88

1607 Gregory RT, Taylor Jr HP. 1981. An oxygen isotope profile in a section of Cretaceous oceanic crust,
1608 Samail Ophiolite, Oman: Evidence for $\delta^{18}\text{O}$ buffering of the oceans by deep (> 5 km) seawater-
1609 hydrothermal circulation at mid-ocean ridges. *J. Geophys. Res.* 86: 2737-55

1610 Grobe A, Virgo S, von Hagke C, Urai JL, Littke R. 2018. Multiphase structural evolution of a
1611 continental margin during obduction orogeny: Insights from the Jebel Akhdar dome, Oman
1612 mountains. *Tectonics* 37: 888-913

1613 Grobe A, von Hagke C, Littke R, Dunkl I, Wübbeler F, Muchez P, Urai JL. 2019. Tectono-thermal
1614 evolution of Oman's Mesozoic passive continental margin under the obducting Semail Ophiolite: a
1615 case study of Jebel Akhdar, Oman. *Solid Earth* 10: 149–75

1616 Guilmette C, Smit MA, Hinsbergen DJJv, Gürer D, Corfu F, Charette B, Maffione M, Rabeau O,
1617 Savard D. 2018. Forced subduction initiation recorded in the sole and crust of the Semail Ophiolite
1618 of Oman. *Nature Geosci.* 11: 699-5

1619 Haase KM, Freund S, Beier C, Koepke J, Erdmann M, Hauff F. 2016. Constraints on the magmatic
1620 evolution of the oceanic crust from plagiogranite intrusions in the Oman ophiolite. *Contrib. Mineral.
1621 Petrol* 171: 1-16

1622 Haase KM, Freund S, Koepke J, Hauff F, Erdmann M. 2015. Melts of sediments in the mantle wedge
1623 of the Oman ophiolite. *Geology* 43: 275-8

1624 Hacker BR. 1996. Eclogite formation and the rheology, buoyancy, seismicity, and H₂O content of
1625 oceanic crust. *AGU Monograph* 96: 337-46

1626 Hacker BR. 2006. Pressures and temperatures of ultrahigh-pressure metamorphism: Implications for
1627 UHP tectonics and H₂O in subducting slabs. *Int. Geol. Rev.* 48: 1053–66

1628 Hacker BR, Gnos E. 1997. The conundrum of Samail: Explaining the metamorphic history.
1629 *Tectonophys.* 279: 215-26

1630 Hacker BR, Mosenfelder JL. 1996. Metamorphism and deformation along the emplacement thrust of
1631 the Samail ophiolite, Oman. *Earth Planet Sci. Lett.* 144: 435-51

1632 Hacker BR, Mosenfelder JL, Gnos E. 1996. Rapid emplacement of the Oman ophiolite: thermal and
1633 geochronologic constraints. *Tectonics* 15: 1230-47

1634 Halls C, Zhao R. 1995. Listvenite and related rocks: Perspectives on terminology and mineralogy with
1635 reference to an occurrence at Cregganbaun, Co. Mayo, Republic of Ireland. *Mineral. Deposita* 30:
1636 303-13

1637 Hanghoj K, Kelemen PB, Hassler D, Godard M. 2010. Composition and genesis of depleted mantle
1638 peridotites from the Wadi Tayin massif, Oman ophiolite; Major and trace element geochemistry, and
1639 Os isotope and PGE systematics. *J. Petrol.* 51: 201-27

1640 Hansen LD, Dipple GM, Gordon TM, Kellett DA. 2005. Carbonated serpentinite (listwanite) at Atlin,
1641 British Columbia: A geological analogue to carbon dioxide sequestration. *Can. Mineral.* 43: 225-39

1642 Hansman RJ, Ring U, Thomson SN, den Brok B, Stübner K. 2017. Late Eocene uplift of the Al Hajar
1643 Mountains, Oman, supported by stratigraphy and low-temperature thermochronology. *Tectonics* 36:
1644 3081–109

1645 Helgeson HC. 1985. Errata II. Thermodynamics of minerals, reactions, and aqueous solutions at high
1646 pressures and temperature. *Am. J. Sci.* 285: 8450855

1647 Helgeson HC, Delany JM, Nesbitt HW, Bird DK. 1978. Summary and critique of the thermodynamic
1648 properties of rock-forming minerals. *Am. J. Sci.* 278-A: 1-229

1649 Helgeson HC, Kirkham DH, Flowers GC. 1981. Theoretical prediction of the thermodynamic behavior
1650 of aqueous electrolytes by high pressures and temperatures; IV, Calculation of activity coefficients,
1651 osmotic coefficients, and apparent molal and standard and relative partial molal properties to 600
1652 degrees C and 5kb. *Am. J. Sci.* 281: 1249-516

1653 Herwegh M, Mercolli I, Linckens J, Müntener O. 2016. Mechanical anisotropy controls strain
1654 localization in upper mantle shear zones. *Tectonics* 35: 1177-204

1655 Hirose F, Nakajima J, Hasegawa A. 2008. Three-dimensional seismic velocity structure and
1656 configuration of the Philippine Sea slab in southwestern Japan estimated by double-difference
1657 tomography. *J. Geophys. Res.* 113: <http://dx.doi.org/10.1029/2007JB005274>

1658 Holland T, Powell R. 2003. Activity–composition relations for phases in petrological calculations: an
1659 asymmetric multicomponent formulation. *Contrib. Mineral. Petrol* 145: 492-501

1660 Holland TJB, Powell RTJB. 1998. An internally consistent thermodynamic data set for phases of
1661 petrological interest. *J. Metamorphic Geol.* 16: 309-43

1662 Horita J. 2014. Oxygen and carbon isotope fractionation in the system dolomite–water–CO₂ to
1663 elevated temperatures. *Geochim. Cosmochim. Acta* 129: 11-124

1664 Huang F, Sverjensky DA. 2019. Extended Deep Earth Water Model for predicting major element
1665 mantle metasomatism. *Geochim. Cosmochim. Acta* 254: 192-230

1666 Ishikawa T, Nagaishi K, Umino S. 2002. Boninitic volcanism in the Oman ophiolite: Implications for
1667 thermal condition during transition from spreading ridge to arc. *Geology* 30: 899-902

1668 Jamtveit B, Putnis C, Malthe-Sorensen A. 2009. Reaction induced fracturing during replacement
1669 processes. *Contrib. Mineral. Petrol.* 157: 127-33

1670 Johnson JW, Oelkers EH, Helgeson HC. 1992. SUPCRT92 - A software package for calculating the
1671 standard molal thermodynamic properties of minerals, gases, aqueous species, and reactions from
1672 1-bar to 5000-bar and 0C to 1000C. *Computers and Geosciences* 18: 899-947

1673 Jurković I, Palinkaš LA, Garašić V, Strmić Palinkaš S. 2012. Genesis of vein-stockwork
1674 cryptocrystalline magnesite from the Dinaride ophiolites. *Ophioliti* 37: 13-26
1675 Kelemen PB, Braun M, Hirth G. 2000. Spatial distribution of melt conduits in the mantle beneath
1676 oceanic spreading ridges: Observations from the Ingalls and Oman ophiolites. *G-cubed* 1:
1677 doi:10.1029/999GC000012
1678 Kelemen PB, Evans O, Ghiorso M, Mustard J, Ehlmann BL, Spiegelman M. 2020a. Carbonate in
1679 Olivine-Rich Unit (s) on Mars May Have Formed at Low P (H₂O). *Lunar & Planetary Science
1680 Conference Abstracts*: 1213
1681 Kelemen PB, Hirth G. 2012. Reaction-driven cracking during retrograde metamorphism: Olivine
1682 hydration and carbonation. *Earth Planet. Sci. Lett.* 345-348: 81–9
1683 Kelemen PB, Koga K, Shimizu N. 1997. Geochemistry of gabbro sills in the crust-mantle transition
1684 zone of the Oman ophiolite: Implications for the origin of the oceanic lower crust. *Earth Planet. Sci.
1685 Lett.* 146: 475-88
1686 Kelemen PB, Manning CE. 2015. Reevaluating carbon fluxes in subduction zones: What goes down,
1687 mostly comes up. *Proc. Nat. Acad. Sci.* 112: E3997-E4006.
1688 <https://doi.org/10.1073/pnas.1507889112>
1689 Kelemen PB, Matter JM, Teagle DAH, Coggon JA, Oman Drilling Project Science Team. 2020b. Site
1690 BT1: fluid and mass exchange on a subduction zone plate boundary,
1691 http://publications.iodp.org/other/Oman/VOLUME/CHAPTERS/113_BT1.PDF. In *Proceedings of the
1692 Oman Drilling Project*, <http://publications.iodp.org/other/Oman/OmanDP.html>, ed. PB Kelemen, JM
1693 Matter, DAH Teagle, JA Coggon, Oman Drilling Project Science Team. College Station, TX:
1694 International Ocean Discovery Program
1695 Kelemen PB, Matter JM, Teagle DAH, Coggon JA, Team ODPS. 2020c. *Proceedings of the Oman
1696 Drilling Project*, doi:10.14379/Oman.ph1-2.proc.2020.
1697 <http://publications.iodp.org/other/Oman/OmanDP.html>. College Station, TX: International Ocean
1698 Discovery Program
1699 Kelemen PB, Shimizu N, Salters VJM. 1995. Extraction of mid-ocean-ridge basalt from the upwelling
1700 mantle by focused flow of melt in dunite channels. *Nature* 375: 747-53
1701 Kerrick DM, Connolly JAD. 2001. Metamorphic devolatilization of subducted oceanic metabasalts:
1702 Implications for seismicity, arc magmatism and volatile recycling. *Earth Planet Sci. Lett.* 189
1703 Kerrick DM, Jacobs GK. 1981. A modified Redlich-Kwong equation for H₂O, CO₂, and H₂O-CO₂
1704 mixtures at elevated pressures and temperatures. *Am. J. Sci.* 281: 735-67
1705 Khedr MZ, Arai S, Python M. 2013. Petrology and chemistry of basal lherzolites above the
1706 metamorphic sole from Wadi Sarami central Oman ophiolite. *J. Mineral. Petrol. Sci.* 108: 13-24
1707 Khedr MZ, Arai S, Python M, Tamura A. 2014. Chemical variations of abyssal peridotites in the
1708 central Oman ophiolite: Evidence of oceanic mantle heterogeneity. *Gondwana Res.* 25: 1242-62
1709 Klein EM, Langmuir CH. 1987. Global correlations of ocean ridge basalt chemistry with axial depth
1710 and crustal thickness. *J. Geophys. Res.* 92: 8089-115
1711 Klein F, Garrido C-J. 2011. Thermodynamic constraints on mineral carbonation of serpentinized
1712 peridotite. *Lithos* 126: 147-60
1713 Klein F, Le Roux V. 2020. Quantifying the volume increase and chemical exchange during
1714 serpentinization. *Geology* 48: 552-6
1715 Kotowski A, Cloos M, Stockli D, Orent EB. 2021. Structural and thermal evolution of an infant
1716 subduction shear zone: Insights from sub-ophiolite metamorphic rocks recovered from Oman
1717 Drilling Project Site BT-1B. *J. Geophys. Res.*; *this paper is in revision; the submitted manuscript is
1718 available online at <https://www.essoar.org/doi/abs/10.1002/essoar.10505943.1>*
1719 Lacinska AM, Styles MT. 2013. Silicified serpentinite—a residuum of a Tertiary palaeo-weathering
1720 surface in the United Arab Emirates. *Geol. Mag.* 150: 385-95
1721 Lanphere MA, Coleman RG, Hopson CA. 1981. Sr isotopic tracer study of the Samail ophiolite,
1722 Oman. *J. Geophys. Res.* 86: 2709-20
1723 Lapham DM. 1961. New data on deweylite. *Am. Min.* 46: 168-88
1724 Li S-G, Yang W, Ke S, Meng X, Tian H, Xu L, He Y, Huang J, Wang X-C, Xia Q, Sun W, Yang X, Ren
1725 Z-Y, Wei H, Liu Y, Meng F, Yan J. 2017. Deep carbon cycles constrained by a large-scale mantle
1726 Mg isotope anomaly in eastern China. *National Science Review* 4: 111-20
1727 Linckens J, Herwegh M, Müntener O, Mercogli I. 2011. Evolution of a polymineralic mantle shear zone
1728 and the role of second phases in the localization of deformation. *J. Geophys. Res.* 116: B06210
1729 Lippard SJ, Shelton AW, Gass IG. 1986. *The Ophiolite of Northern Oman. Geological Society London
1730 Memoir* 11. 178 pp.
1731 MacLeod CJ, Lissenberg CJ, Bibby LE. 2013. “Moist MORB” axial magmatism in the Oman ophiolite:
1732 the evidence against a mid-ocean ridge origin. *Geology* 41: 459-62

- 1733 Madu BE, Nesbitt BE, Muehlenbachs K. 1990. A mesothermal gold-stibnite-quartz vein occurrence in
1734 the Canadian Cordillera. *Econ. Geol.* 85: 1260-8
- 1735 Malvoisin B. 2015. Mass transfer in the oceanic lithosphere: serpentinization is not isochemical. *Earth*
1736 *Planet Sci. Lett.* 430: 75-85
- 1737 Malvoisin B, Zhang C, Müntener O, Baumgartner LP, Kelemen PB, Team ODPS. 2020. Measurement
1738 of volume change and mass transfer during serpentinisation: Insights from the Oman Drilling
1739 Project. *J. Geophys. Res.* 125: e2019JB018877
- 1740 Manning C, Lu S, Kelemen P, Oman Drilling Project Phase 1 Science Party. 2018. Origin of
1741 Serpentinite and Listvenite Near the Basal Thrust of the Samail Ophiolite Recorded in Oman Drilling
1742 Project Hole BT1B. *AGU Fall Meeting Abstracts*: V11B-07
- 1743 *Manning, CE, S Lu, PB Kelemen, and The Oman Drilling Project Phase 1 Science Party, Origin of*
1744 *Serpentinite and Listvenite Near the Basal Thrust of the Samail Ophiolite Recorded in Oman Drilling*
1745 *Project Hole BT1B, AGU Fall Meeting Abstracts, V11B-07, 2018; this citation is standing in for*
1746 *Manning et al. CE. 2021. Replacement of serpentinite by listvenite, OmanDP Hole BT1B. J.*
1747 *Geophys. Res., the manuscript of which is not yet available to share*
- 1748 McCulloch MT, Gregory RT, Wasserburg GJ, Taylor Jr HP. 1980. A neodymium, strontium, and
1749 oxygen isotopic study of the Cretaceous Samail Ophiolite and implications for the petrogenesis and
1750 seawater-hydrothermal alteration of oceanic crust. *Earth Planet Sci. Lett.* 46: 201-11
- 1751 McCulloch MT, Gregory RT, Wasserburg GJ, Taylor Jr HP. 1981. Sm-Nd, Rb-Sr, and 18O/16O
1752 isotopic systematics in an oceanic crustal section: Evidence from the Samail Ophiolite. *J. Geophys.*
1753 *Res.* 86: 2721-35
- 1754 McKenzie D, Bickle MJ. 1988. The volume and composition of melt generated by extension of the
1755 lithosphere. *J. Petrol.* 29: 625-79
- 1756 Menzel MD, Garrido CJ, López Sánchez-Vizcaíno V, Marchesi C, Hidas K, Escayola MP, Delgado
1757 Huertas A. 2018. Carbonation of mantle peridotite by CO₂-rich fluids: the formation of listvenites in
1758 the Advocate ophiolite complex (Newfoundland, Canada). *Lithos* 323: 238-61
- 1759 Menzel MD, Urai JL, Kelemen PB, Hirth G. 2021. Ductile deformation during carbonation of
1760 serpentinized peridotite. *Nature Communications*; *a preprint of the submitted manuscript is available*
1761 *online at <https://www.essoar.org/doi/abs/10.1002/essoar.10505943.1>*
- 1762 Menzel MD, Urai JL, Obeso JCd, Kotowski A, Manning CE, Kelemen PB, Kettermann M, Jesus AP,
1763 Harigane Y, Team ODPPS. 2020. Brittle deformation of carbonated peridotite: Insights from
1764 listvenites of the Samail Ophiolite (Oman Drilling Project Hole BT1B). *J. Geophys. Res.* 125,
1765 *e2020JB020199*
- 1766 Monnier C, Girardeau J, Le Mée L, M. P. 2006. Along-ridge petrological segmentation of the mantle in
1767 the Oman ophiolite. *G-cubed* 7: doi:10.1029/2006GC001320
- 1768 Nahon D, Merino E. 1987. Pseudomorphic replacement in tropical weathering: Evidence,
1769 geochemical consequences, and kinetic-rheological origin. *Am. J. Sci.* 297: 393-417
- 1770 Nasir S, Al Sayigh A, Al Harthy A, Al-Khribash S, Al-Jaaidi O, Musllam A, Al-Mishwat A, Al-Bu'saidi S.
1771 2007. Mineralogical and geochemical characterization of listwaenite from the Semail Ophiolite,
1772 Oman. *Chemie der Erde* 67: 213-28
- 1773 Nicolas A, Boudier F, Ildefonse B. 1996. Variable crustal thickness in the Oman ophiolite: Implication
1774 for oceanic crust. *J. Geophys. Res.* 101: 17,941-17,50
- 1775 Nicolas A, Boudier F, Ildefonse B, Ball E. 2000. Accretion of Oman and United Arab Emirates
1776 ophiolite: Discussion of a new structural map. *Marine Geophys. Res.* 21: 147-79
- 1777 Ninkabou D, Agard P, et al. 2021. Structure of the offshore obducted Oman margin: Emplacement of
1778 the Semail ophiolite and role of tectonic inheritance. *J. Geophys. Res.* in press
- 1779 Okazaki K, Michibayashi K, Hatakeyama K, Abe N, Johnson K, Kelemen P. 2021. Major mineral
1780 fraction and physical properties of carbonated peridotite (listvenite) from ICDP Oman Drilling Project
1781 Hole BT1B inferred from X-ray CT core images *J. Geophys. Res.* *A preprint of the submitted*
1782 *manuscript is available online at <https://www.essoar.org/doi/abs/10.1002/essoar.10506374.1>*
- 1783 Oskierski HC, Bailey JG, Kennedy EM, Jacobsen G, Ashley PM, Dlugogorski BZ. 2013a. Formation of
1784 weathering-derived magnesite deposits in the New England Orogen, New South Wales, Australia:
1785 Implications from mineralogy, geochemistry and genesis of the Attunga magnesite deposit.
1786 *Mineralium Deposita* 48: 525-641
- 1787 Oskierski HC, Dlugogorski BZ, Jacobsen G. 2013b. Sequestration of atmospheric CO₂ in a
1788 weathering-derived, serpentinite-hosted magnesite deposit: 14C tracing of carbon sources and age
1789 constraints for a refined genetic model. *Geochim. Cosmochim. Acta* 122: 226-46
- 1790 Pan D, Spanu L, Harrison B, Sverjensky DA, Galli G. 2013. Dielectric properties of water under
1791 extreme conditions and transport of carbonates in the deep Earth. *Proc. Nat. Acad. Sci.* 110: 6646–
1792 50

1793 Peacock SM. 1996. Thermal and petrologic structure of subduction zones. *AGU Monograph* 96: 119-
1794 33

1795 Peacock SM, van Keken PE, Holloway SD, Hacker BR, Abers GA, Ferguson RL. 2005. Thermal
1796 structure of the Costa Rica – Nicaragua subduction zone. *Phys. Earth Planet. Int.* 149: 187-200

1797 Pearce JA, Alabaster T, Shelton AW, Searle MP. 1981. The Oman Ophiolite as a Cretaceous Arc-
1798 Basin Complex: Evidence and Implications. *Phil. Trans. Roy. Soc. London* A300: 299-317

1799 Pearce JA, Peate DW. 1995. Tectonic implications of the composition of volcanic arc magmas. *Ann.*
1800 *Rev. Earth Planet. Sci.* 23: 251-86

1801 Penniston-Dorland SC, Kohn MJ, Manning CE. 2015. The global range of subduction zone thermal
1802 structures from exhumed blueschists and eclogites: Rocks are hotter than models. *Earth Planet Sci.*
1803 *Lett.* 428: 243-54

1804 Posukhova TV, Panasian LL, Sas IE. 2013. Serpentinites of the ural: mineralogical features,
1805 petrophysical properties and subduction processes. *Open J. Geology*. doi:10.4236/ojg.2013

1806 Powell R, Holland TJBH, Worley B. 1998. Calculating phase diagrams involving solid solutions via
1807 non-linear equations, with examples using THERMOCALC. *J. Metamorphic Geol.* 16: 577-88

1808 Prigent C, Agard P, Guillot S, Godard M, Dubacq B. 2018a. Mantle wedge (de)formation during
1809 subduction infanicy: Evidence from the base of the Semail ophiolitic mantle. *J. Petrol.* 59: 2061-92

1810 Prigent C, Guillot S, Agard P, Lemarchand D, Soret M, Ulrich M. 2018b. Transfer of subduction fluids
1811 into the deforming mantle wedge during nascent subduction: Evidence from trace elements and
1812 boron isotopes (Semail ophiolite, Oman). *Earth Planet Sci. Lett.* 484: 213-28

1813 Quesnel B, Boulvais P, Gautier P, Cathelineau M, John CM, Dierick M, Agrinier P, Drouillet M. 2016.
1814 Paired stable isotopes (O, C) and clumped isotope thermometry of magnesite and silica veins in the
1815 New Caledonia Peridotite Nappe. *Geochim. Cosmochim. Acta* 183: 234-49

1816 Quesnel B, Gautier P, Boulvais P, Cathelineau M, Maurizot P, Cluzel D, Ulrich M, Guillot S, Lesimple
1817 S, Couteau C. 2013. Syn-tectonic, meteoric water-derived carbonation of the New Caledonia
1818 peridotite nappe. *Geology* 41: 1063-6

1819 Raleigh CB, Paterson MS. 1965. Experimental deformation of serpentinite and its tectonic
1820 implications. *J. Geophys. Res.* 70: 3965-85

1821 Reiners PW, Spell TL, Nicolescu S, Zanetti KA. 2004. Zircon (U-Th)/He thermochronometry: He
1822 diffusion and comparisons with ⁴⁰Ar/³⁹Ar dating. *Geochim. Cosmochim. Acta*: 1857-87

1823 Rioux M, Benoit M, Amri I, Ceuleneer G, Garber JM, Searle M, Leal K. 2021a. The origin of felsic
1824 intrusions within the mantle section of the Semail ophiolite: Geochemical evidence for three distinct
1825 mixing and fractionation trends. *J. Geophys. Res.*: e2020JB020760

1826 Rioux M, Bowring S, Kelemen P, Gordon S, Dudás F, Miller R. 2012. Rapid crustal accretion and
1827 magma assimilation in the Oman-U.A.E. ophiolite: High precision U-Pb zircon geochronology of the
1828 gabbroic crust. *J. Geophys. Res.* 117: B07201, doi:10.1029/2012JB009273

1829 Rioux M, Bowring S, Kelemen P, Gordon S, Miller R, Dudás F. 2013. Tectonic development of the
1830 Semail ophiolite: High precision U-Pb zircon geochronology of crustal growth and ophiolite
1831 emplacement. *J. Geophys. Res.* 118: 2085-101

1832 Rioux M, Garber J, Bauer A, Bowring S, Searle M, Kelemen P, Hacker B. 2016. Synchronous
1833 formation of the metamorphic sole and igneous crust of the Semail ophiolite: New constraints on the
1834 tectonic evolution during ophiolite formation from high-precision U-Pb zircon geochronology. *Earth*
1835 *Planet. Sci. Lett.* 451: 185-95

1836 Rioux M, Garber J, Searle M, Kelemen P, Miyashita S, Adachi Y, Bowring S. 2021b. High-precision
1837 U-Pb zircon dating of late magmatic series in the Semail ophiolite: A record of subduction initiation.
1838 *J. Geophys. Res.* in press

1839 Rollinson H. 2015. Slab and sediment melting during subduction initiation: granitoid dykes from the
1840 mantle section of the Oman ophiolite. *Contrib. Mineral. Petrol* 170: 1-20

1841 Rudge JF, Kelemen PB, Spiegelman M. 2010. A simple model of reaction-induced cracking applied to
1842 serpentinization and carbonation of peridotite. *Earth Planet Sci. Lett.* 291: 215-27

1843 Scambelluri M, Bebout GE, Belmonte D, Gilio M, Campomenosi N, Collins N, Crispini L. 2016.
1844 Carbonation of subduction-zone serpentinite (high-pressure ophicarbonates; Ligurian Western Alps)
1845 and implications for the deep carbon cycling. *Earth Planet Sci. Lett.* 441: 155-66

1846 Scarsi M, Malatesta C, Fornasaro S. 2018. Lawsonite-bearing eclogite from a tectonic mélange in the
1847 Ligurian Alps: New constraints for the subduction plate-interface evolution. *Geol. Mag.* 155: 280-97

1848 Schandl ES, Naldrett AJ. 1992. CO₂ metasomatism of serpentinites south of Timmins, Ontario. *Can.*
1849 *Mineral.* 30: 93-108

1850 Schandl ES, Wicks FJ. 1991. Carbonate and associated alteration of ultramafic and rhyolitic rocks at
1851 the Hemingway Property, Kidd Creek Volcanic Complex, Timmins, Ontario. *Econ. Geol.* 88: 1615-
1852 35

- 1853 Scharf A, Mattern F, Bolhar R, Bailey CM, Ring U. 2020. *U-Pb dating of postobductional carbonate*
1854 *veins in listwaenite of the Oman Mountains near Fanja*. Presented at Proceedings of the
1855 International Conference on Ophiolites and the Oceanic Lithosphere: Results of the Oman Drilling
1856 Project and Related Research, Sultan Qaboos University, Oman
1857 Searle M, Cox J. 1999. Tectonic setting, origin, and obduction of the Oman ophiolite. *GSA Bull.* 111:
1858 104-22
1859 Searle M, Cox J. 2002. Subduction zone metamorphism during formation and emplacement of the
1860 Semail ophiolite in the Oman Mountains. *Geol. Mag.* 139: 241-55
1861 Searle MP, Lippard SJ, Smewing JD, Rex DC. 1980. Volcanic rocks beneath the Semail Ophiolite
1862 nappe in the northern Oman mountains and their significance in the Mesozoic evolution of Tethys.
1863 *J. Geol. Soc. London* 137: 589-604
1864 Searle MP, Malpas J. 1980. The structure and metamorphism of rocks beneath the Semail ophiolite of
1865 Oman and their significance in ophiolite obduction. *Trans. Roy. Soc. Edinburgh Earth Sci.* 71: 247-
1866 62
1867 Searle MP, Malpas J. 1982. Petrochemistry and origin of sub-ophiolitic metamorphic and related
1868 rocks in the Oman Mountains. *J. Geol. Soc. London* 139: 235-48
1869 Searle MP, Robertson AHF. 1990. The northern Oman Tethyan continental margin: Stratigraphy,
1870 structure, concepts and controversies. *Geol. Soc. Special Pub.* 49: 3-25
1871 Searston SM. 1998. *Resource estimation and the Kunwarara magnesite deposit*. University of
1872 Tasmania, Hobart, Tasmania. 356 pp.
1873 Shock EL, Oelkers EH, Johnson JW, Sverjensky DA, Helgeson HC. 1992. (1992) Calculation of the
1874 thermodynamic properties of aqueous species at high pressures and temperatures: Effective
1875 electrostatic radii, dissociation constants and standard partial molal properties to 1000 _____
1876 C and 5 kbar. *J. Chem. Soc. Faraday Trans.* 88: 803-26
1877 Shock EL, Sassani DC, Willis M, Sverjensky DA. 1997. Inorganic species in geologic fluids:
1878 correlations among standard molal thermodynamic properties of aqueous ions and hydroxide
1879 complexes. *Geochim. Cosmochim. Acta* 61: 907-50
1880 Sofiya A, Ishiwatari A, Hirano N, Tsujimori T. 2017. Relict chromian spinels in Tulu Dimtu
1881 serpentinites and listvenite, Western Ethiopia: implications for the timing of listvenite formation. *Int.*
1882 *Geol. Rev.* 59: 1621-31
1883 Soret M, Agard P, Dubacq B, Plunder A, Yamato P. 2017. Petrological evidence for stepwise
1884 accretion of metamorphic soles during subduction infancy (Semail ophiolite, Oman and UAE). *J.*
1885 *Metamorphic Geol.* 35: 1051-80
1886 Spencer CJ, Cavosie AJ, Raub TD, Rollinson H, Jeon H, Searle MP, Miller JA, McDonald BJ, Evans
1887 NJ. 2017. Evidence for melting mud in Earth's mantle from extreme oxygen isotope signatures in
1888 zircon. *Geology* 45: 975-8
1889 Stanger G. 1985. Silicified serpentinite in the Semail nappe of Oman. *Lithos* 18: 13-22
1890 Stewart EM, Ague JJ. 2020. Pervasive subduction zone devolatilization recycles CO₂ into the forearc.
1891 *Nature Communications* 11: 1-8
1892 Styles MT, Ellison RA, Phillips ER, Arkley S, Schofield DI, Thomas RJ, Goodenough KM, Farrant AR,
1893 McKervey JA, Crowley QG, Pharaoh TC. 2006. *The Geology and Geophysics of the United Arab*
1894 *Emirates, vol.2*. Abu Dhabi: Ministry of Energy, United Arab Emirates
1895 Sverjensky DA, Harrison B, Azzolini D. 2014. Water in the deep Earth: the dielectric constant and the
1896 solubilities of quartz and corundum to 60 kb and 1200 C. *Geochim. Cosmochim. Acta* 129: 125-45
1897 Syracuse EM, Keken PEv, Abers GA. 2010. The global range of subduction zone thermal models.
1898 *Phys. Earth Planet. Int.* 183: 73-90
1899 Takazawa E, Okayasu T, Satoh K. 2003. Geochemistry and origin of the basal lherzolites from the
1900 northern Oman ophiolite (northern Fizh block). *G-cubed* 4: 1021
1901 Tilton GR, Hopson CA, Wright JE. 1981. Uranium-lead isotopic ages of the Semail ophiolite, Oman,
1902 with applications to Tethyan ocean ridge tectonics. *J. Geophys. Res.* 86: 2736-75
1903 Ulrich M, Munoz M, Guillot S, Cathelineau M, Picard C, Quesnel B, Boulvais P, Couteau C. 2014.
1904 Dissolution–precipitation processes governing the carbonation and silicification of the serpentinite
1905 sole of the New Caledonia ophiolite. *Contrib. Mineral. Petrol* 167: 952; doi 10.1007/s00410-013-
1906 0952-8
1907 van Hinsbergen DJJ, Maffione M, Koornneef LMT, Guilmette C. 2019. Kinematic and paleomagnetic
1908 restoration of the Semail ophiolite (Oman) reveals subduction initiation along an ancient Neotethyan
1909 fracture zone. *Earth Planet Sci. Lett.* 518: 183-96
1910 van Keken PE, Wada I, Sime N, Abers GA. 2019. Thermal structure of the forearc in subduction
1911 zones: A comparison of methodologies. *G-cubed* 20: 3268–88

- 1912 Villey M, Le Metour J, De Gramont X. 1986. *Geological Map of Fanjah. Muscat, Oman*. Muscat,
1913 Oman: Ministry of Petroleum and Minerals, Directorate General of Minerals, Sultanate of Oman
- 1914 Warren C, Parrish R, Waters D, Searle M. 2005. Dating the geologic history of Oman's Semail
1915 ophiolite: insights from U–Pb geochronology. *Contrib. Mineral. Petrol.* 150: 403-22
- 1916 Weyhenmeyer CE. 2000. *Origin and evolution of groundwater in the alluvial aquifer of the Eastern
1917 Batinah Coastal Plain, Sultanate of Oman : a hydrogeochemical approach*. University of Bern, Bern,
1918 CH
- 1919 Wilde A, Simpson L, Hanna S. 2002. Preliminary study of Tertiary hydrothermal alteration and
1920 platinum deposition in the Oman ophiolite. *J. Virtual Explorer* 6: 7-13
- 1921 Wilson CR, Spiegelman M, van Keken PE, Hacker BR. 2014. Fluid flow in subduction zones: The role
1922 of solid rheology and compaction pressure. *Earth Planet Sci. Lett.* 401: 261-74
- 1923 Wohlwend S, Celestino R, Reháková D, Huck S, Weissert H. 2017. Late Jurassic to Cretaceous
1924 evolution of the eastern Tethyan Hawasina Basin (Oman Mountains). *Sedimentology* 64: 87-110
- 1925 Wolery TJ. 1992. EQ3/6, a software package for geochemical modeling of aqueous systems: package
1926 overview and installation guide (version 7.0) (No. UCRL-MA--110662-PT. 1). *Lawrence Livermore
1927 National Lab*
- 1928 Yoshikawa M, Python M, Tamura A, Arai S, Takazawa E, Shibata T, Ueda A, Sato T. 2015. Melt
1929 extraction and metasomatism recorded in basal peridotites above the metamorphic sole of the
1930 northern Fizz massif, Oman ophiolite. *Tectonophysics*. 650: 53-64
- 1931 Zarrinkoub MH, Amini S, Aftabi A, Karimpour MH. 2005. Mineralogy, geochemistry, structural position
1932 and a genetic model for listvenite in the east of Iran. *Iranian J. Crystallography & Mineralogy* 13:
1933 363-78
- 1934 Zimmer K, Zhang YL, Lu P, Chen Y.Y., Zhang GR, Dalkilic M, Zhu C. 2016. SUPCRTBL: A revised
1935 and extended thermodynamic dataset and software package of SUPCRT92. *Computers and
1936 Geosciences* 90: 97-111
- 1937